12-2014

Characterization of Electron Number Density of Rocket Exhaust Plumes Through Microwave Transmissions

Jorge Torres
Embry-Riddle Aeronautical University - Daytona Beach

Embry-Riddle Aeronautical University

Master's Thesis

Characterization of Electron Number Density of Rocket Exhaust Plumes Through Microwave Transmissions

Author:
Jorge Torres

Advisor:
Dr. William C. Barott

A thesis submitted in partial fulfillment of the requirements
for the degree of Master of Science in Electrical and Computer Engineering

in the

Radar & Microwaves Laboratory
Department of Electrical, Computer, Software, and Systems Engineering

December 2014

Committee Approval

"Characterization of Electron Number Density of Rocket Exhaust Plumes Through Microwave Transmissions,"

Jorge Torres

This thesis is prepared under the direction of the candidate's thesis committee chairman, Dr. William C. Barott, Department of Electrical, Computer, Software, and Systems Engineering, and has been approved by members of his thesis committee. It is submitted to the Electrical, Computer, Software, and Systems Engineering Department in partial fulfillment of the requirements for the degree of Master of Science in Electrical and Computer Engineering.

Dated: 12-3-14

Committee Members:

Dr. William C. Barott:

Dr. Jianhua Liu:

Dr. William Engblom:

ECSSE Department Chair:

Dr. Tim Wilson:

Dean of the College of Engineering:

Dr. Maj Mirmirani:

Associate Vice President for Academics:

Dr. Robert Oxley:

Embry-Riddle Aeronautical University

Author	Jorge Torres
Title	Characterization of Electron Number Density of Rocket Exhaust Plumes Through Microwave Transmissions
Department	Electrical, Computer, Software, and Systems Engineering
Degree	MSECE
Convocation	December 2014

Signature of Author: _____

Date: _____

"If you can't take a little bloody nose, maybe you ought to go back home and crawl under your bed. It's not safe out here. It's wondrous, with treasures to satiate desires both subtle and gross; but it's not for the timid."

Q

Embry-Riddle Aeronautical University

Abstract

Master of Science in Electrical and Computer Engineering

Characterization of Electron Number Density of Rocket Exhaust Plumes Through Microwave Transmissions

by Jorge Torres

Dr. William C. Barott, Dr. Jianhua Liu, and Dr. William Engblom
Department of Electrical, Computer, Software, and Systems Engineering

Charged rocket plumes generally exceed the length of their source vehicles, and offer lightning a favorable path to ground. Rocket plumes enhance the induced transient currents in flight electronics, and increase the risk of vehicle failure. The affinity of lightning to the plume can be associated with the plume's electrical properties, which are coupled to plasma characteristics including the electron number density. However, the electron number density of rocket plumes is not well-known. In this study, the electron number density is characterized through data from static rocket firings. A model of the plume in finite difference time domain (FDTD) simulations also supports the results. Radio frequency and radar methodologies are used to characterize the plume as a dynamic component of an electrical system, supported by the construction of an RF apparatus that includes the design and manufacture of ultra-wideband antenna arrays. The research estimates electron number density using methods exploiting signal processing techniques in time and frequency domain, but the data suggests that other dynamic elements influence delay and attenuation of the radio signal.

Acknowledgements

I would like to acknowledge Dr. William Barott for his assistance and persistent encouragement throughout the research. His support and motivation made it possible to carry on even when challenged by different pieces of this research. I would like to thank my thesis committee, Dr. Jianhua Liu and Dr. William Engblom, for support of this research, as well as Dr. Ebenezer Gnanamanickam, the Embry-Riddle Future Space Explorers and Developers Society (ERFSEDS), and the Experimental Rocket Propulsion Lab (ERPL) for their help with organizing and setting up the live tests. Acknowledged also is the Rogers Corporation, who donated milling substrate to this research. I'd also like to thank Jeanette Barott for her help in editing the document, my family for their encouragement, and lastly, my future wife, Kelly Baczuk. She is my inspiration.

Contents

List of Figures

List of Tables

Abbreviations

CAD	**C**omputer-**A**ided **D**esign
CFD	**C**omputational **F**luid **D**ynamics
DC	**D**irect **C**urrent
ECSSE	**E**lectrical, **C**omputer, **S**oftware, and **S**ystems **E**ngineering
ERAU	**E**mbry-**R**iddle **A**eronautical **U**niversity
ERFSEDS	**E**mbry-**R**iddle **F**uture **S**pace **E**xplorers and **D**evelopers **S**ociety
ERPL	**E**xperimental **R**ocket **P**ropulsion **L**abs
FDTD	**F**inite **D**ifference **T**ime **D**omain
GIMP	**G**NU **I**mage **M**anipulation **P**rogram
IR	**I**nfra-**R**ed
LPKF	**L**eiter**P**latten **K**oppier **F**rasen
MSECE	**M**aster of **S**cience in **E**lectrical and **C**omputer **E**ngineering
RF	**R**adio **F**requency
Rx	**R**eceiver
SMA	**S**ub**M**iniature, Version **A**
SNR	**S**ignal-to-**N**oise **R**atio
SLV	**S**pace **L**aunch **V**ehicle
Tx	**T**ransmitter
VNA	**V**ector **N**etwork **A**nalyzer

Symbols

B	Bandwidth	Hz
d	Vivaldi antenna ground plane length	cm
d_p	Diameter of a slab of the plume	m
h	Vivaldi antenna width	cm
l	Vivaldi antenna length	cm
L_{Np}	Attenuation through a slab of the plume	Np
L_{dB}	Attenuation through a slab of the plume	dB
N_e	Electron number density	Number / cm^3
r	Vivaldi antenna feedline cutout radius	cm
R	Range resolution	m
t_d	Time offset	s
t_0	Plasma Relaxation time	s
u_p	Phase velocity	m / s
v_e	Electron-neutral collision frequency	Hz
y	Path length	m
Y	Vivaldi antenna opening function	cm

α	Attenuation constant	Np / m
β	Phase constant	rad/m
γ	Propagation Constant	m^{-1}
ϵ	Permittivity	F / m
ϵ_r	Relative permittivity	unitless
ϵ_s	Static-frequency relative permittivity	unitless
ϵ_∞	Infinite-frequency relative permittivity	unitless
η	Refractive index	unitless

λ	Wavelength	m
μ_r	Relative permeability	unitless
μ_s	Static-frequency relative permeability	unitless
μ_∞	Infinite-frequency relative permeability	unitless
σ	Conductivity	S / m
σ_m	Magnetic conductivity	S / m
τ	Time resolution	s
ω	Radio wave angular frequency	radians / s
ω_p	Plasma frequency	radians / s

I dedicate this study to the scientists, researchers, and engineers whose works were essential to my research. If I have seen further, it is by standing on the shoulders of giants.

Chapter 1

Introduction

1.1 Summary

This thesis is a continuation of research into a precise measurement of the electron number density, N_e, in rocket exhaust plumes. N_e is quantified in this study by using radio frequency and radar techniques to measure small changes in radio waves propagating through the plumes.

1.2 Motivation

The combination of pressures, temperatures, and chemical interactions in rocket exhaust plumes creates a dusty, dynamic plasma. Plumes generally exceed the length of their source vehicles, and offer lightning a favorable path to ground. Although aircraft often endure lightning strikes, rocket plumes enhance the induced transient currents in flight electronics, and increase the risk of vehicle failure [1].

Historically, lightning strike events in rocketry include the loss of the U.S. Navy's FLTSATCOM Satellite in 1987 (Figure 1.1) [2], and the ascent of the Apollo 12 mission in which a lightning strike took the Saturn Command Service Module instrumentation offline [3] (Figure 1.2).

FIGURE 1.1: The AC-67 Atlas I SLV mission carrying FLTSATCOM resulted in failure due to a lightning strike [2]

FIGURE 1.2: Lightning strikes the Saturn V vehicle during the Apollo 12 mission [3]

Lightning's affinity to the plume can be associated with the plume's electrical properties, which are coupled to plasma characteristics, including the electron number density. These properties can be used to model the plume's observed effects on radio waves, such

as communications blackouts caused by attenuation and multipath interference [4]. The electron number density can be estimated by measurements of these effects [5].

Rigorous electromagnetic calculations of the plume's effects on radio waves and its conductivity require knowledge of the plasma frequency ω_p, collision frequency v_e, electron number density N_e, and radio wave frequency, ω.

1.3 Previous Works

Previous work was done by Nicholas Coutu in his thesis, *Implementation of Microwave Transmissions for Rocket Exhaust Plume Diagnostics* [5], in which he constructed an apparatus to measure N_e in J-class solid rocket motor plumes using C-band transmissions. Coutu's data saw distortion effects believed to have been caused by focusing of antenna beams by the plume. This was manifested as a signal enhancement during motor firing instead of an attenuation, which would have been used to determine the density of the plasma. Due to this, a precise value for N_e was not found in his thesis.

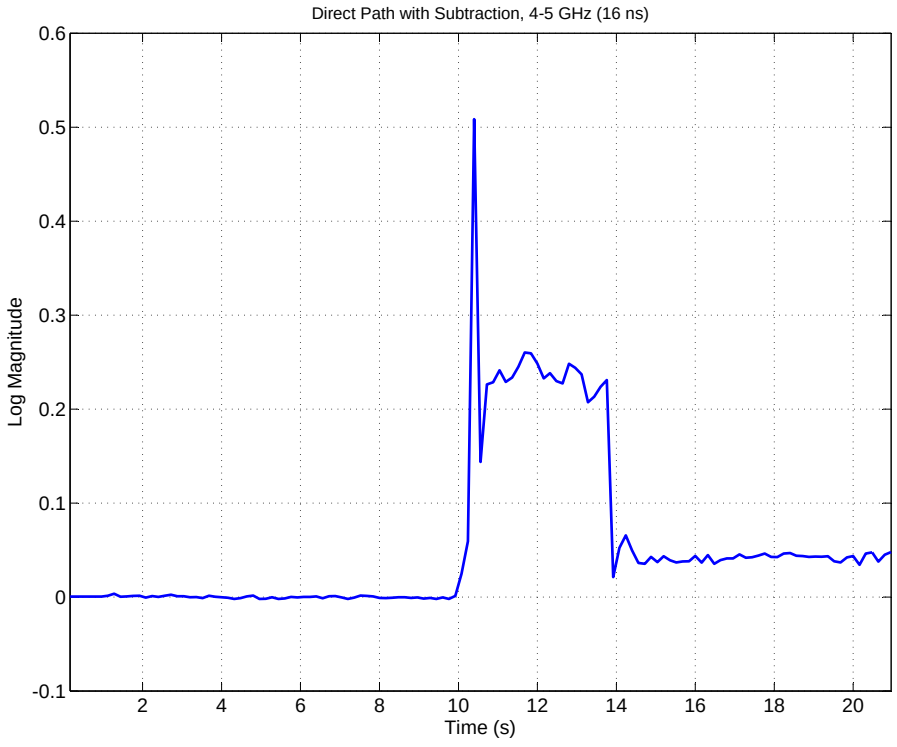

FIGURE 1.3: Increased gain found in Nicholas Coutu's thesis, believed to have been caused by beam focusing (Firing Occurs at 10 s) [5]

1.4 Scope of Works

This research extends Coutu's apparatus to work in higher frequency bands, as was recommended at the end of his thesis. This study attempts to explain whether the distortion effects were caused by focusing through electromagnetics simulations, and experimentally by observing the plume effects on a narrow (as opposed to Coutu's wide) beamwidth. The apparatus in this research has a higher sampling rate than Coutu's, allowing deeper analysis of slow-time events.

Additionally, this work introduces a new method of measuring plume properties through time-domain analysis, in terms of the phase velocity u_p of a radio wave propagating through the plume, and the plume's refraction index, η. Because of the ability to finely observe small differences in time-domain, multiple beams caused by intentional multipath are also used as a source of data

After analysis in Chapter 4, a value for N_e is determined through analysis of live rocket fire experiments.

Chapter 2

Background and Theory

The electrical properties of rocket exhaust are dominated by its plasma properties, which are largely determined by N_e, and the ion collision frequency, v_e [6]. The amount of electrons in a rocket motor plume can be influenced by many factors, including the propellant formulation, alkali impurities, exhaust temperature, motor size, chamber pressure, flight speed and altitude, and the distance down-stream from the nozzle exit [7]. Solid rocket plumes particularly contain a high amount of alkali impurities, which have low ionization potentials, leading to a higher number of free electrons [8]. Fortunately, characterization of rocket plasma has been the subject of many studies, for both academic [4, 9–11] and commercial interests [6, 8, 12, 13]. However, available estimates for attenuation or conductivity are often an order of magnitude between prediction and tests [14, 15], meaning that additional ways to estimate plume characteristics are needed in order to estimate their electromagnetic effects.

2.1 Plume Plasma Theory

The plume is a dynamic medium, whose interaction with electromagnetic waves is largely frequency dependent. Lightning attractiveness is mostly related to a plume's conductivity, σ, while radio wave attenuation is related more with its permittivity, ϵ. The conductivity of a plasma given by

$$\sigma = \frac{q_e^2 N_e}{m_e \left(v_e - j\omega\right)}, \tag{2.1}$$

where N_e is the electron number density, q_e is the elementary charge of an electron, ω is the frequency of an electrical signal, m_e is the mass of an electron, and v_e is the electron (ion) collision frequency [9].

The relative permittivity of plasmas is given by

$$\epsilon_r = 1 - \frac{w_p^2}{\omega\left(\omega - jv_e\right)}, \tag{2.2}$$

in which ω_p is the plasma frequency [15], calculated from

$$\omega_p = \sqrt{\frac{N_e q_e^2}{\epsilon_0 m_e}}, \tag{2.3}$$

where ϵ_0 is the permittivity of free space [16]. The electrical permittivity of a material is given by combining the permittivity of free space and its relative permittivity, by

$$\epsilon = \epsilon_r \epsilon_0. \tag{2.4}$$

Calculating v_e requires situational knowledge of the plasma's composition. One of Smoot's works [17] provides the approximation for collision frequency at a single point in a rocket plume, described as

$$v_e = v_{et} \sum_i n_i Q_i, \tag{2.5}$$

where v_{et} is the mean electron thermal velocity defined by

$$v_{et} = \sqrt{\frac{8kT_e}{\pi m_e}}. \tag{2.6}$$

In equations 2.5 and 2.6, k is Boltzmann's constant, T_e is the temperature of the plume at the estimating point, n_i is the number density of species i, and Q_i is the electron collision cross-section of species i. However, n_i and Q_i are dependent on the chemical interactions in the plume and must be obtained empirically by measurement or by simulation. Many other researchers in the subject [4, 9, 15], including Coutu [5], choose to derive both v_e and N_e through the rocket firings by calculating the propagation constant of the waves traveling through a rocket plume. The propagation constant can be calculated using different methods, or measured directly, but in definition is given by

$$\gamma = \alpha + j\beta, \tag{2.7}$$

where α and β are the attenuation and phase constants of the propagating wave, respectively. The attenuation constant is given by

$$\alpha = \frac{L_{\mathrm{Np}}}{y}, \tag{2.8}$$

where L_{Np} is the loss (or gain) through a medium in Nepers, and y is the path length through the medium in meters. Nepers are a logarithmic scale of power, and are converted to decibels using a factor of 10 log e^2 [18]. The phase constant is frequency dependent, and is defined by

$$\beta = \frac{\omega}{u_p}, \tag{2.9}$$

where u_p is the phase velocity of the wave traveling through the medium.

Van der Beek et al. give an analytic calculation for α and β based on plasma properties [9]:

$$\alpha = \frac{\omega}{c}\sqrt{-\frac{1-A}{2} + \frac{1}{2}\sqrt{(1-A)^2 + \frac{v_e^2}{\omega^2}A^2}} \tag{2.10}$$

and

$$\beta = -\frac{\omega}{c}\sqrt{\frac{1-A}{2} + \frac{1}{2}\sqrt{(1-A)^2 + \frac{v_e^2}{\omega^2}A^2}}, \tag{2.11}$$

where A is as described by

$$A = \frac{\omega_p^2}{v_e^2 + \omega^2}. \tag{2.12}$$

By equating the two relations for α in equations 2.8 and 2.10, and the two relations for β in equations 2.9 and 2.11, it is possible to characterize both the collision frequency and the electron number density by knowing ω, v_e, and L_{Np}.

Previous work by Smoot [14] also provides an approximation for the attenuation through a slab of plasma using only N_e, v_e, and ω, and path length y as

$$L_{\mathrm{dB}} = 0.46\left(\frac{y v_e N_e}{v_e^2 + \omega^2}\right), \tag{2.13}$$

which can be used as a secondary form of estimation for N_e if the collision frequency is known.

2.2 Time-Delay Measurements

In radar theory, the range resolution is determined by the signal bandwidth, B [19]. The smallest time interval that the radar can resolve is the inverse of bandwidth, as shown by

$$\tau = \frac{1}{B}. \tag{2.14}$$

In order to find the phase velocity u_p of a radio wave traveling through the plume, the delay of the wave in the plume must be characterized by comparing measurements in time-domain to those before and during a rocket motor fires. To the author's knowledge, characterization of u_p in rocket plumes has not previously been examined for plasma attenuation or electron density studies.

This inherently requires a wide bandwidth system to extract small delays in time-domain, which spreads the value for N_e and v_e in section 2.1, due to varying values of ω. Also, the smaller the rocket motor, the more precise the ranging information must be, since light travels at approximately one foot per nanosecond, but is slowed only slightly by most materials. Sufficient accuracy should require ranging information to be at the picosecond level for this work.

Because resolution is the inverse of system bandwidth, a 1 ps resolution requires an unrealistically high bandwidth of 1 THz. To reduce this requirement, signals in the frequency-domain may be multiplied by a phasor, e^{-jwt_d}, to shift in the time-domain by t_d seconds [20] as shown by

$$X\left(j\omega\right) e^{\left(-j\omega t_d\right)} \rightleftharpoons x(t - t_d). \tag{2.15}$$

While the resolution is proportional to the inverse of bandwidth, the ability to detect an impulse in the absence of other signals scales as

$$\tau \propto \frac{1}{B\sqrt{\mathrm{SNR}}}, \tag{2.16}$$

where SNR is signal-to-noise ratio. e.g. A 1 ps accuracy with 3 GHz of bandwidth requires 50 dB of SNR. Phasors of varying time t_d can be multiplied with frequency domain data, and the peak of the resulting time-domain signal would indicate the true direct path maximum. If this is done before and during a rocket motor fire, the change in the Δt_d required to find the signal maximum gives a delay in the electromagnetic

wave. This greatly reduces the needed bandwidth of the system, since if the plume is electrically large compared to the wavelengths of the incoming wave, its delay can be measured. This is true so long as the range resolution of the radar-like signal is able to separate the plume from multipath, where range resolution [19] is given by

$$\Delta R = c\tau. \tag{2.17}$$

It is also possible to calculate the electron density directly from the time-delay, since if the propagation velocity u_p of a wave in the plume is known, the index of refraction can be calculated as a ratio of the velocity of light in air and the velocity of light in the plume as shown by

$$\eta = \frac{c}{u_p} = \sqrt{\epsilon_r}. \tag{2.18}$$

Chapter 3

Methodology

3.1 Finite-Difference Time Domain Simulations

As a component of this study, preliminary simulation work was performed to determine whether focusing effects hypothesized in Coutu's thesis could be observed on a model of the plume using Finite-Difference Time-Domain (FDTD) software.

A model of Coutu's experiment was created in Dassault Systèmes' Solidworks and simulated in Agilent EMPro.

3.1.1 FDTD Parameters

In FDTD simulations, plasmas are typically modeled using the following parameters:

1. Infinite frequency relative permittivity, ϵ_∞
2. Infinite frequency relative permeability, μ_∞
3. Static relative permittivity, ϵ_r
4. Static relative permeability, μ_r
5. Electrical conductivity, σ
6. Magnetic conductivity, σ_m, and
7. Plasma Relaxation time, t_0.

Zhu, in his master's thesis, describes how these parameters can be derived from the plasma frequency (which is dependent on N_e) and is described in equation 2.3, and the damping (collision) frequency, v_e [21]. The parameters are defined as

$$\sigma = \epsilon_0 \frac{\omega_p^2}{v_e}, \tag{3.1}$$

$$\sigma_m = \mu_0 \frac{\omega_p^2}{v_e}, \tag{3.2}$$

$$\epsilon_s = -\left(\frac{\omega_p}{v_e}\right)^2 + \epsilon_\infty, \tag{3.3}$$

$$\mu_s = -\left(\frac{\omega_p}{v_e}\right)^2 + \mu_\infty, \tag{3.4}$$

and

$$t_0 = \frac{1}{v_e}. \tag{3.5}$$

In order to simplify the model, Zhu assumed that the values of ϵ_∞ and μ_∞ were equal to 1.

3.1.2 Model Construction

Since v_e and N_e are only known experimentally in this study, the FDTD plume model was initially constructed with values estimated using the Computational Fluid Dynamics (CFD) analysis in Coutu's thesis.

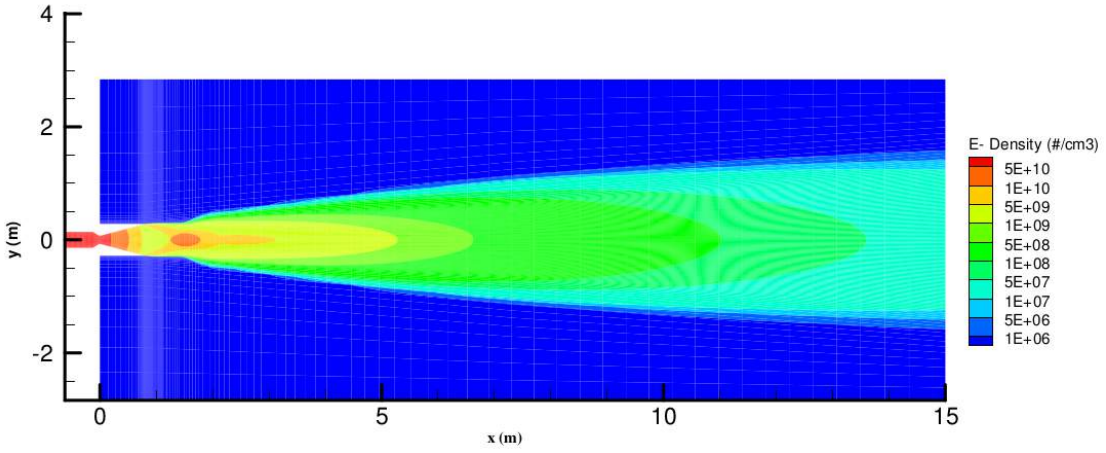

FIGURE 3.1: Coutu's simulated values for N_e [5]

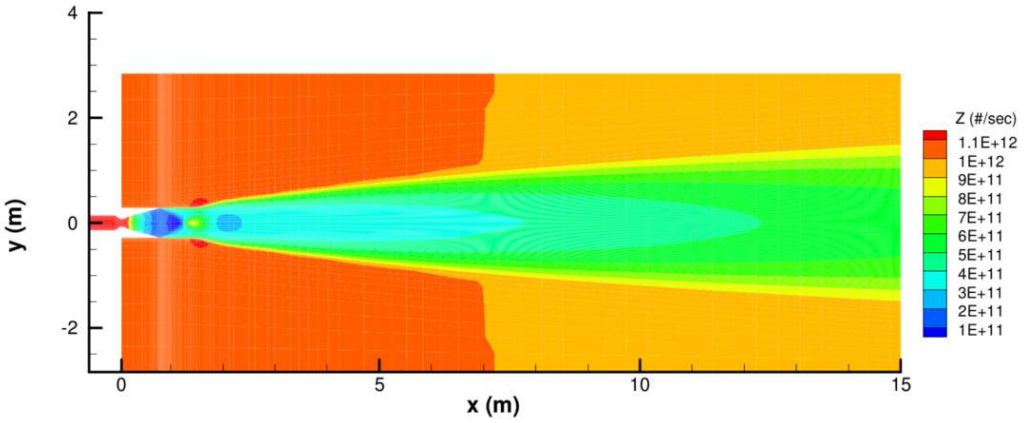

FIGURE 3.2: Coutu's simulated values for v_e [5]

Using the GNU Image Manipulation Program (GIMP), the two contours were combined to produce a set of regions with different N_e and v_e values as shown in Figure 3.3.

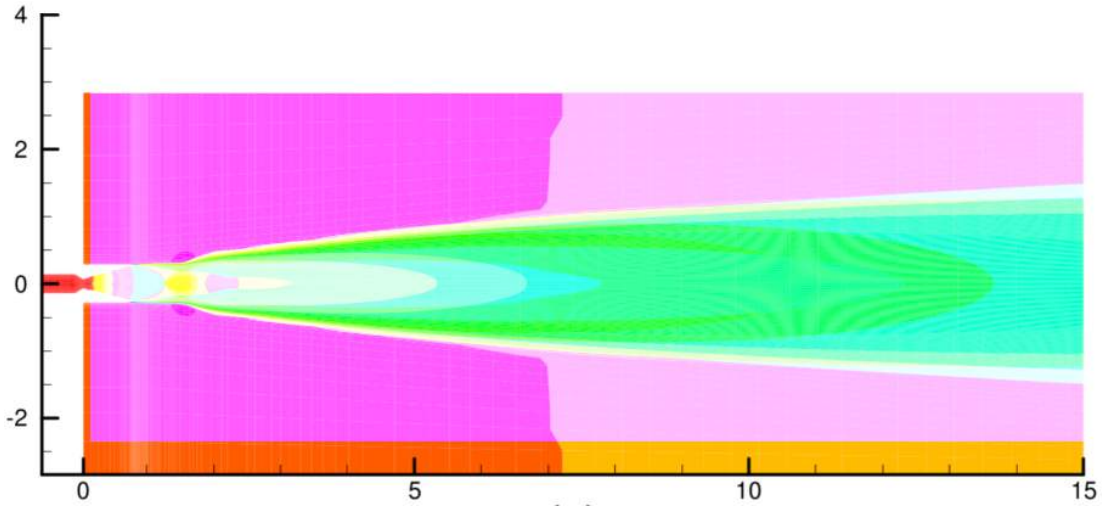

FIGURE 3.3: Composite image showing curves created by contours of N_e and v_e produced in previous CFD plots

This was then revolved in Solidworks to create a three-dimensional CAD model that could be imported into EMPro.

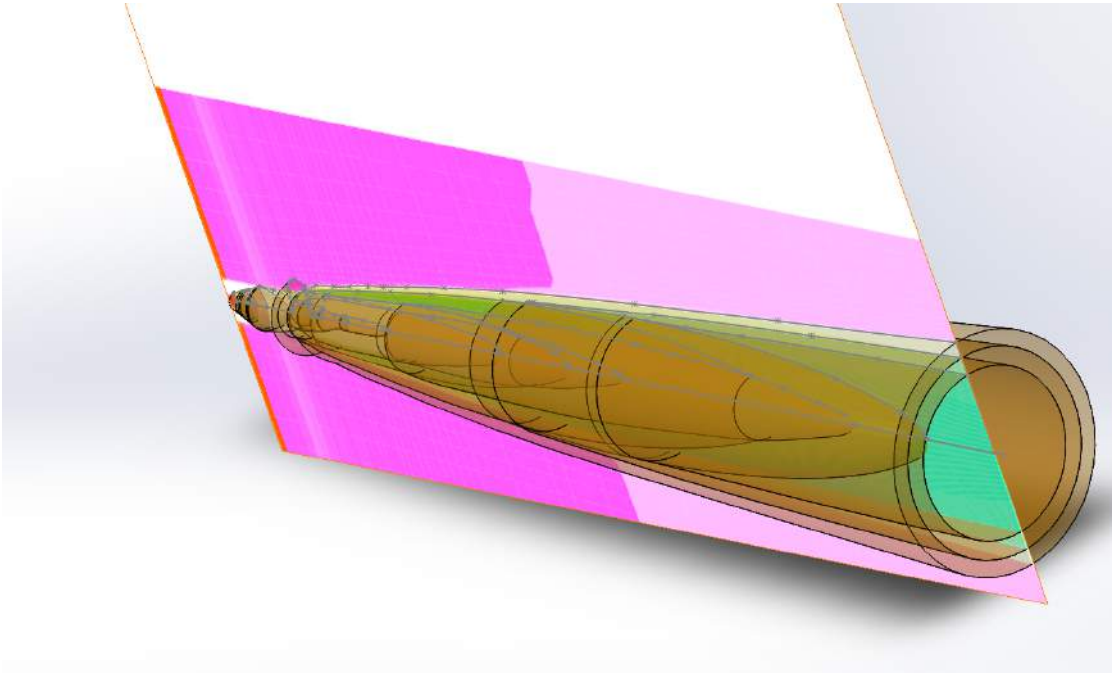

FIGURE 3.4: Solidworks model of the different plume regions

The rest of the apparatus was also modeled in Solidworks and imported into EMPro.

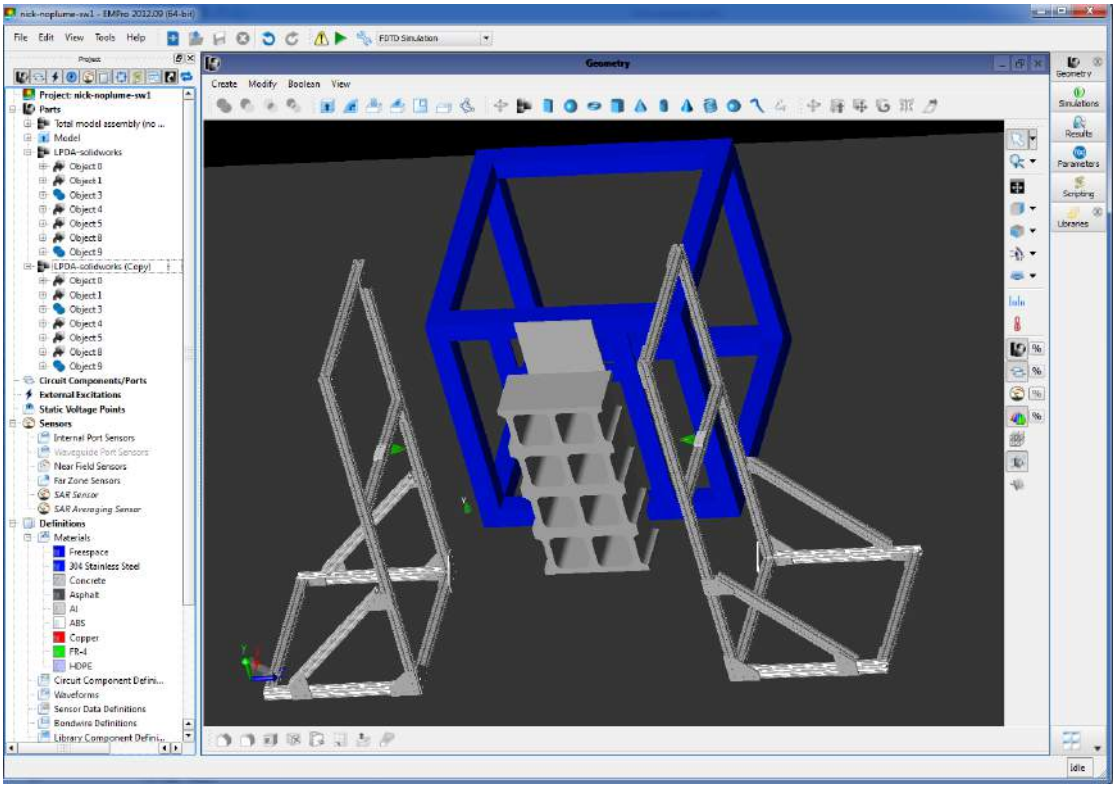

FIGURE 3.5: Model of the apparatus in Agilent EMPro

3.2 Apparatus

The apparatus was built as an extension of Coutu's apparatus [5] to enable higher frequencies and a vertically compressed beamwidth. In designing the apparatus, the plume is considered as a dynamic component of the RF system, using radio frequency and radar techniques to analyze how it attenuates and delays a radio wave. This is similar to principles established by Baghdady on characterizing radio properties through rocket plumes [10].

3.2.1 Selection of Radio Frequencies

Coutu's thesis suggested that, for the scale of rocket engines being tested, higher frequencies exhibited stronger results when passing through the plume [5]. This is logical, as a J-class rocket motor plume is not large compared to the size of a wavelength in the C-band range. The region of highest electron densities, which Coutu estimated to be 10 cm wide, is the focus of the experiment. In addition, at the lower edge of the C-band frequencies, the experiment apparatus placed the antennas before the far-field [22], and was therefore susceptible to possible near-field distortions. Being limited by equipment availability and cost, the focus of this research moved the C-band measurements in Coutu's experiment into the X and Ku-bands. Since this new range of frequencies is outside the range of the original apparatus, including its Vector Network Analyzer (VNA), the apparatus must now incorporate new hardware, including a local oscillator, mixers, filters, and antennas, to support the higher frequency range.

3.2.2 Antenna Design

The antennas are the most crucial part of the apparatus in expanding this study. The antennas for the apparatus must overcome the difficulties faced by the previous experiments in two ways. First, the vertical beamwidth of the antennas must be reduced to reduce the possibility of bending and focusing of the radio waves propagating through the plume, and minimize multipath interference from the ground in order to space the antennas at far-field distances. Second, the antennas must support as narrow a beamwidth as possible at a range of frequencies higher than the original experiment's, thereby making the wavelength smaller in relation to the size of the plume, and maintain sufficient time resolution to separate the direct path signal from reflections in order to observe time-delay effects caused by the plume. A higher gain also helps mitigate the increased path loss due to higher frequencies.

As in Coutu's thesis, horn antennas were determined to be prohibitively expensive despite the advantages provided by their wide bandwidth. Additionally, the capability to mill printed circuit boards with high precision at the laboratory enabled fabrication of antennas from RF-specialty laminates. Therefore, an array of Vivaldi antennas were implemented as both the receive and transmit elements to fulfill the specified criteria.

Yang, Wang, and Fathy describe the methodology of designing a Vivaldi antenna array. The paper details the design of both a "traditional" tapered-slot antenna and an antipodal Vivaldi antenna [23].

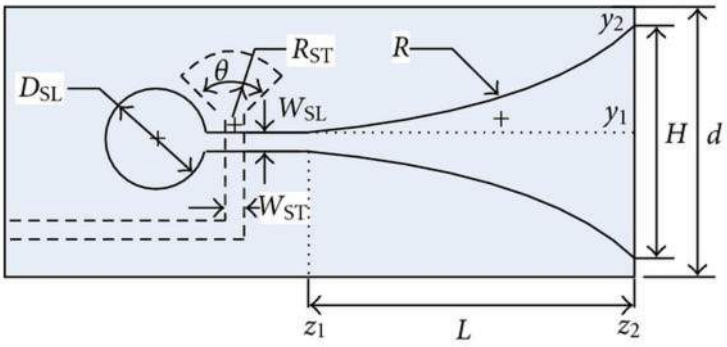

FIGURE 3.6: Traditional tapered-slot Vivaldi design [24]

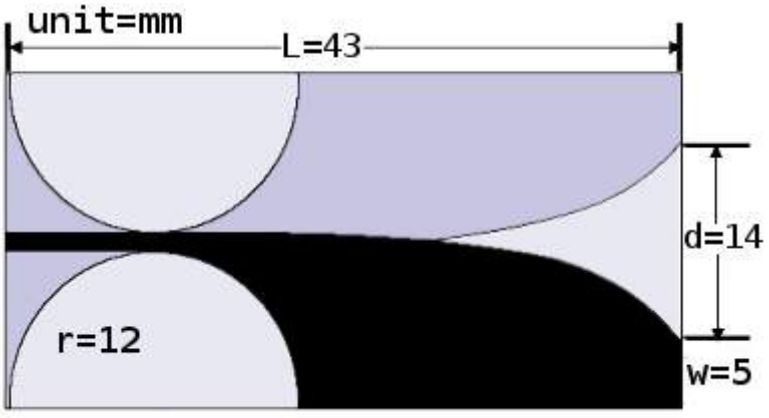

FIGURE 3.7: Antipodal Vivaldi Design from Yang et al. [23]

The antipodal design (figure 3.7) is comparable in characteristics to the traditional tapered slot (figure 3.6), but has fewer parameters to adjust, and is therefore easier to design. The antennas were modeled and tested for performance in gain across a range of 8 to 16 GHz using Solidworks and EMPro. To enable rapid prototyping of the antennas, the parameters for antipodal Vivaldis were simplified optimized for an array configuration.

Since the total opening of the Vivaldi antenna affects its bandwidth (i.e., the larger the opening, the lower the minimum frequency of the antenna becomes), the w value in Yang et al.'s antenna model (figure 3.7) is reduced to zero, where the entire width of one antenna is now h, as shown in figure 3.8.

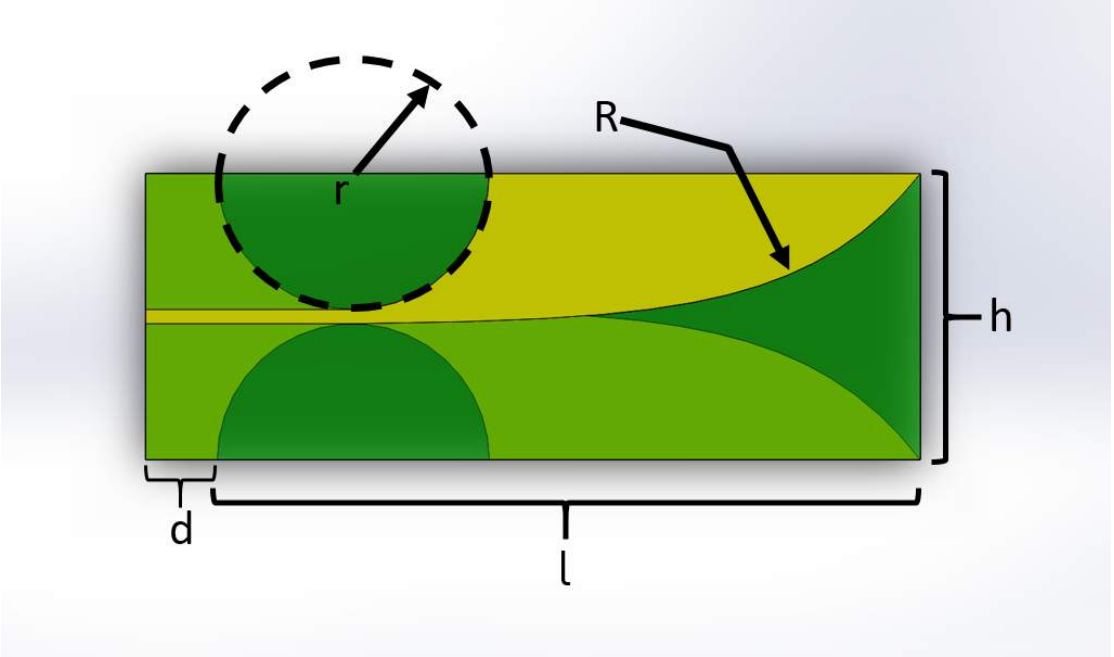

FIGURE 3.8: Modeled Vivaldi antenna describing parameters adjusted during simulation runs for optimization of gain patterns in an array

Since it is known that the antenna will be used in an array, it can also be assumed that h will be locked to

$$h = \frac{\lambda_{maxfreq}}{2}, \tag{3.6}$$

in order to maximize bandwidth and without introducing grating lobes into the overall array gain pattern [25].

The parameter R in Figure 3.8 represents the opening rate of the Vivaldi antennas, as described by Yang et al. [23] in the equation describing the antenna opening rate,

$$Y = c_1 e^{Rx} + c_2 \tag{3.7}$$

where c_1 and c_2 are described by

$$c_1 = \frac{y_2 - y_1}{e^{Rx_2} - e^{Rx_1}} \tag{3.8}$$

and

$$c_2 = \frac{y_1 e^{Rx_2} - y_2 e^{Rx_1}}{e^{Rx_2} - e^{Rx_1}} \tag{3.9}$$

respectively. However, assuming that y_1 and x_1 are the origin, $[0, 0]$, the equation can be reduced into

$$y = \frac{h}{e^{R(l+d)} - 1} \left(e^{Rx} - 1\right), \tag{3.10}$$

the parameters for which are as labeled in figure 3.8. The value of R affects the gain of the antennas at an inverse of bandwidth. For the apparatus antenna, the R value of -0.12 was chosen as an optimal compromise between bandwidth and gain, as described in Abbosh's paper [26].

The values of r and d in figure 3.8 are adjusted only for impedance matching the antennas to the rest of the feed. In this case, r is adjusted to change the impedance of the feed strip into the radiating element. The parameter d needs to be large enough to make a proper match, and can extend from then on until the end of the antenna printed circuit without affecting performance. For an antenna array, d encompasses the entire backplane of the antenna leading up to the half of the radiating element. The overall length of the antenna is adjusted to the value at which the y function in equation 3.10 intersects the corner of the board at a 45-degree angle, past which the antenna sees decremental gains in bandwidth.

Using, Rogers 4003C Laminate with a thickness of 0.508 mm, the selected antenna parameters were as described in table 3.1

d	>5 mm
l	43 mm
r	12 mm
h	19.5 mm
R	-0.12

TABLE 3.1: Parameters chosen after empirical testing of antenna performance

producing an antenna pattern as illustrated in figures 3.9 - 3.11 indicating the principal polarization strength in dBi.

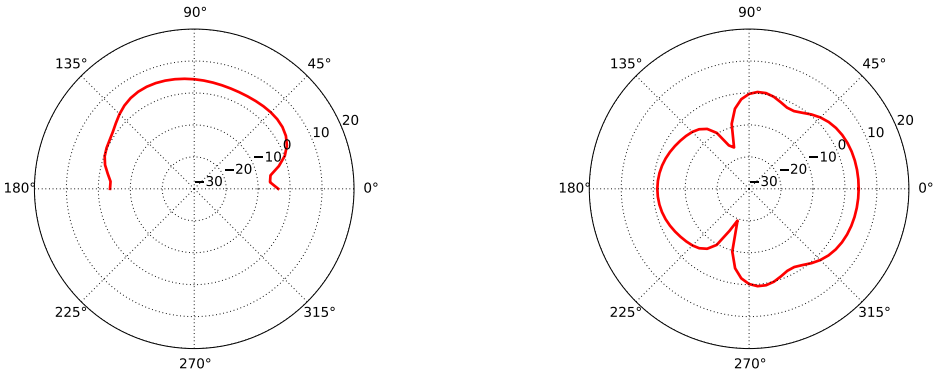

(a) E-plane of 9 GHz Radiation Pattern (b) H-plane of 9 GHz Radiation Pattern

FIGURE 3.9: Single Vivaldi antenna radiation pattern at 9 GHz

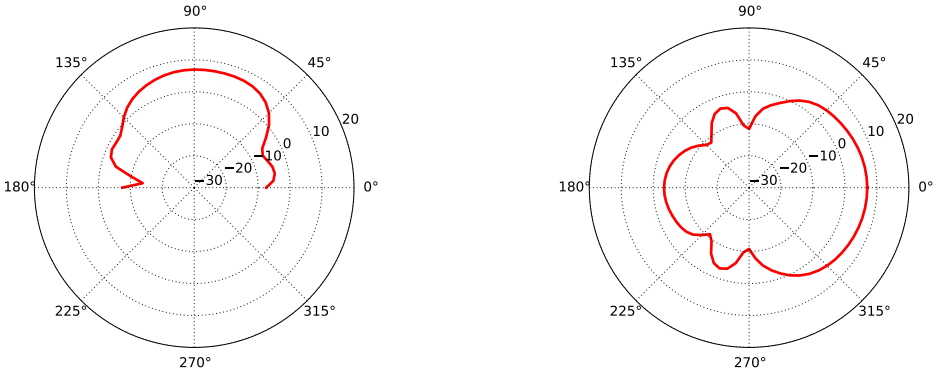

(a) E-plane of 13 GHz Radiation Pattern (b) H-plane of 13 GHz Radiation Pattern

FIGURE 3.10: Single Vivaldi antenna radiation pattern at 13 GHz

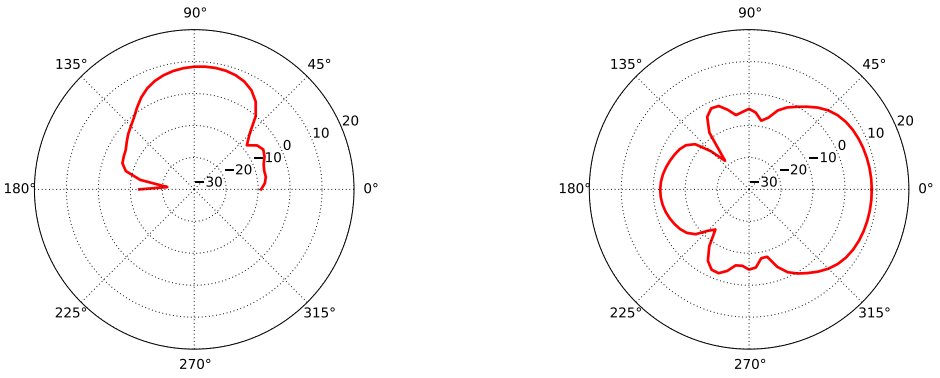

(a) E-plane of 15 GHz Radiation Pattern (b) H-plane of 15 GHz Radiation Pattern

FIGURE 3.11: Single Vivaldi antenna radiation pattern at 15 GHz

The RO4003C material available in the laboratory was 12" x 18", which limited the array size to eight elements if exotic wideband power splitter configurations are avoided.

An antenna pattern produced by eight elements of this antenna with power perfectly split would result in pattern described in figures 3.12, 3.13, and 3.14.

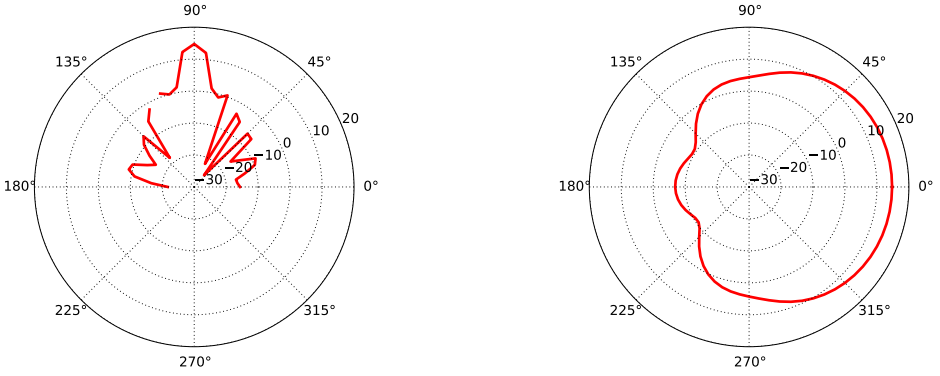

(a) E-plane of 9 GHz Radiation Pattern (b) H-plane of 9 GHz Radiation Pattern

FIGURE 3.12: Ideal Vivaldi array radiation pattern at 9 GHz

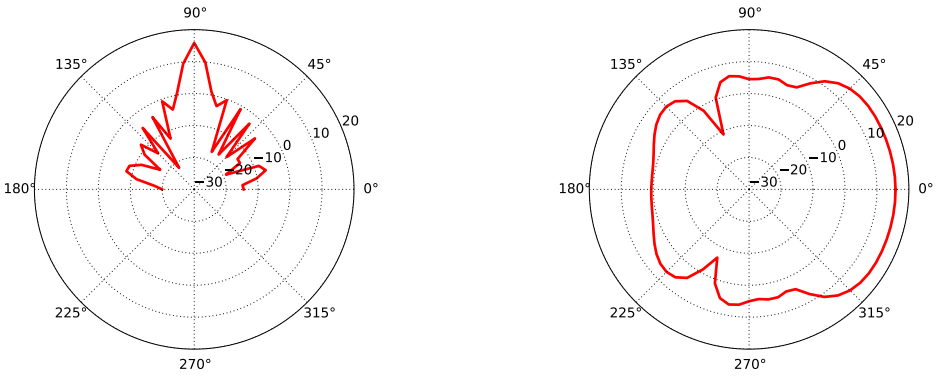

(a) E-plane of 13 GHz Radiation Pattern (b) H-plane of 13 GHz Radiation Pattern

FIGURE 3.13: Ideal Vivaldi array radiation pattern at 13 GHz

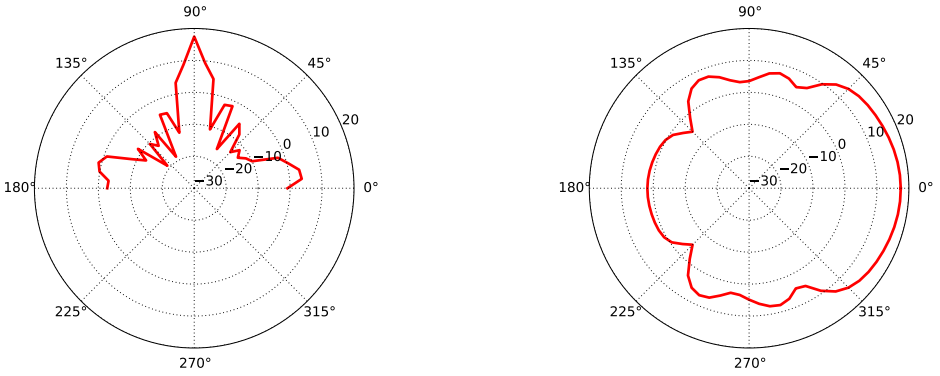

(a) E-plane of 15 GHz Radiation Pattern (b) H-plane of 15 GHz Radiation Pattern

FIGURE 3.14: Ideal Vivaldi array radiation pattern at 15 GHz

In order to split power equally among the eight array elements while maintaining an optimal response across the antennas' bandwidth, a five-stage Wilkinson transformer was chosen as a splitter for the array. The transformer's impedances were determined with microwaves101's spreadsheet tool [27], which produced resistor values and line impedances as listed in table 3.2.

Section	Resistor value	Line impedance	Line width for 0.508 mm RO4003C
1	52.3 Ω	1.22 kΩ	0.33 mm
2	59 Ω	206 Ω	0.44 mm
3	71.5 Ω	210 Ω	0.65 mm
4	84.5 Ω	122 Ω	0.91 mm
5	95.3 Ω	65.8 Ω	1.11 mm

TABLE 3.2: Wilkinson section impedances and resistor value, and line width corresponding to the line impedance in 0.508 mm RO4003C (Refer to figure 3.16)

The response of the five-stage section calculated by the spreadsheet tool is given by the the graph in figure 3.15.

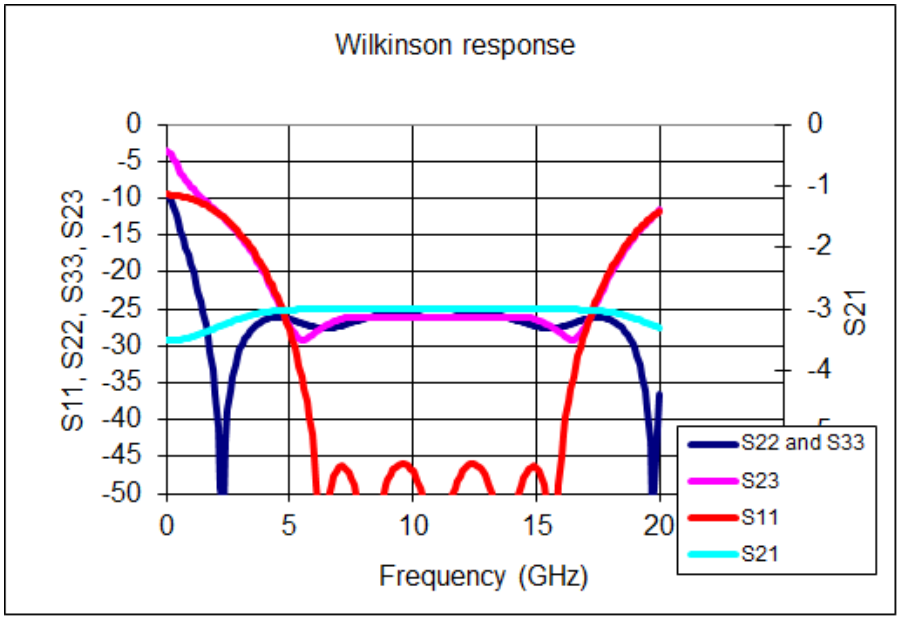

FIGURE 3.15: S-parameters of 5-stage Wilkinson for 6-16 GHz range

Utilizing 0402 resistor dimensions, the section was synthesized in Solidworks, producing a section illustrated in figure 3.16.

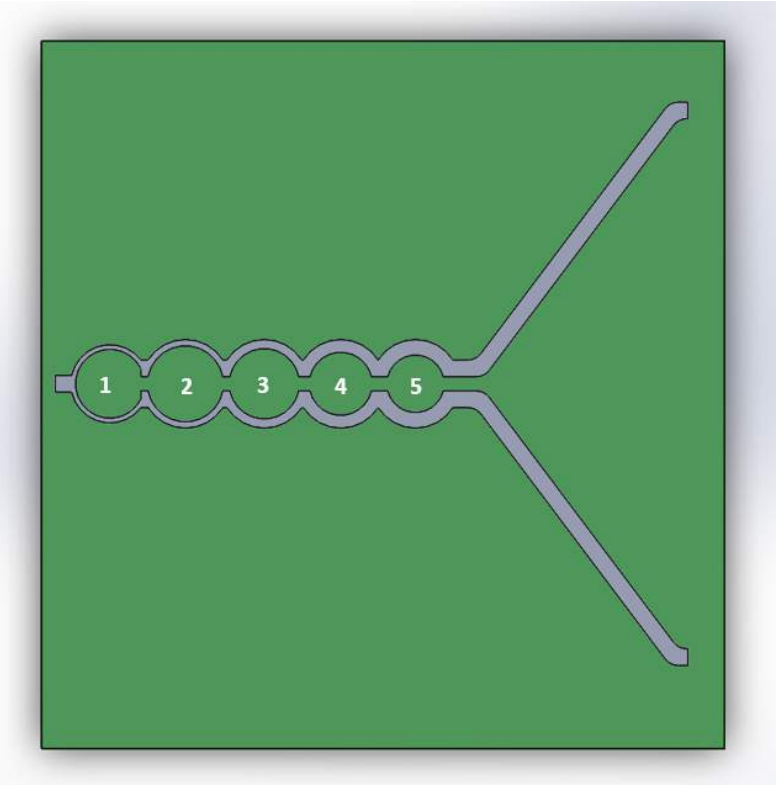

FIGURE 3.16: 5-stage Wilkinson design with labeled sections

Assembling all of the previous elements together yields a complete array as depicted in figure 3.17.

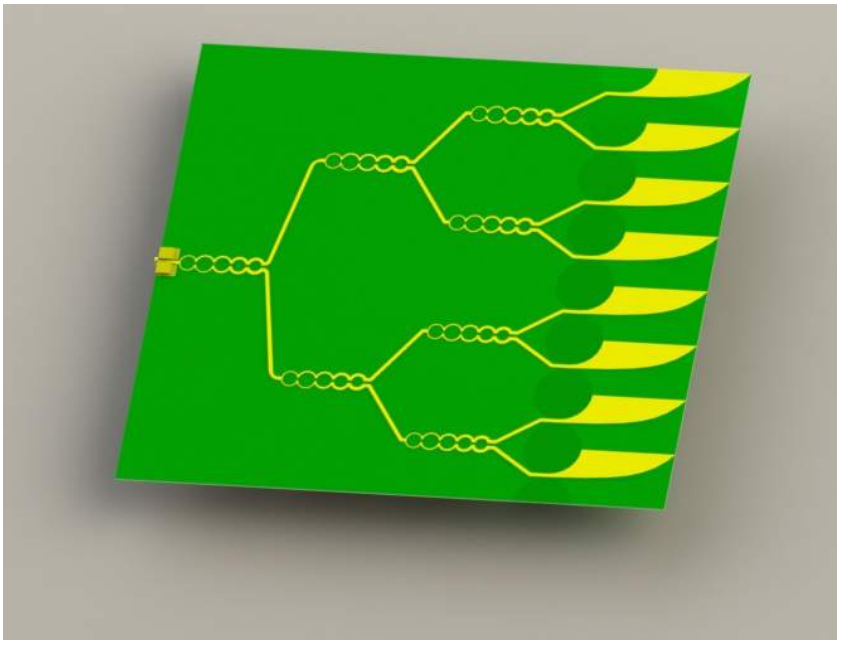

FIGURE 3.17: Complete 8-element Vivaldi array

Finally, the performance of the entire array is measured in terms of the gain and beam pattern by simulating the array in EMPro, with its patterns described at 9 GHz, 13 GHz, and 15 GHz, in figures 3.18, 3.19, and 3.20 respectively.

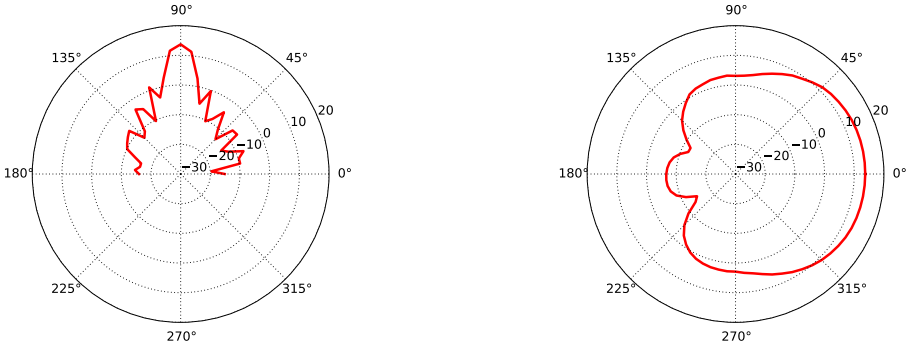

(a) E-plane of 9 GHz Radiation Pattern (b) H-plane of 9 GHz Radiation Pattern

FIGURE 3.18: Simulated Vivaldi array radiation pattern at 9 GHz

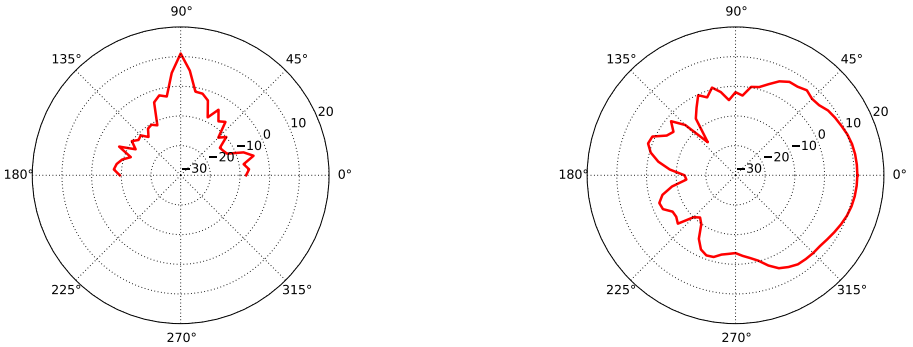

(a) E-plane of 13 GHz Radiation Pattern (b) H-plane of 13 GHz Radiation Pattern

FIGURE 3.19: Simulated Vivaldi array radiation pattern at 13 GHz

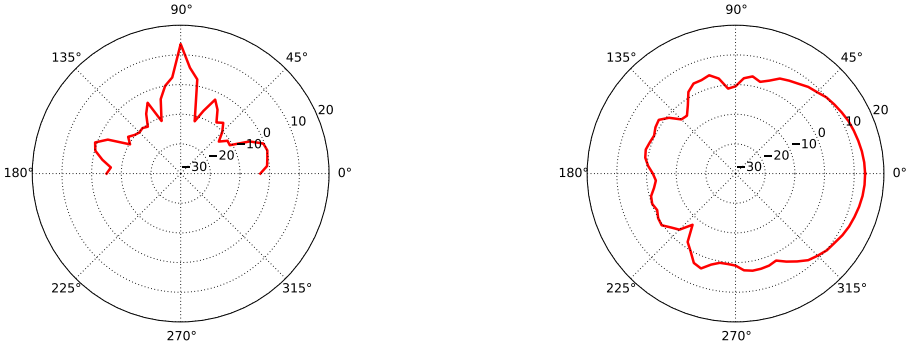

(a) E-plane of 15 GHz Radiation Pattern (b) H-plane of 15 GHz Radiation Pattern

FIGURE 3.20: Simulated Vivaldi array radiation pattern at 15 GHz

As expected, the radiation pattern of the full array with the power dividers implemented is measurably weaker than the ideal eight-way split seen earlier in figures 3.12, 3.13, and 3.14. The five-stage Wilkinson transforms have a flat response across their design bandwidth, at the cost of a higher insertion loss over the 8 GHz frequency range. The realistic case loses about 5 dB in the radiation pattern, due to inefficiencies in the system.

The Vivaldi array was fabricated using an LPKF S103 mill in the Radar & Microwaves Lab, and is shown in figure 3.21.

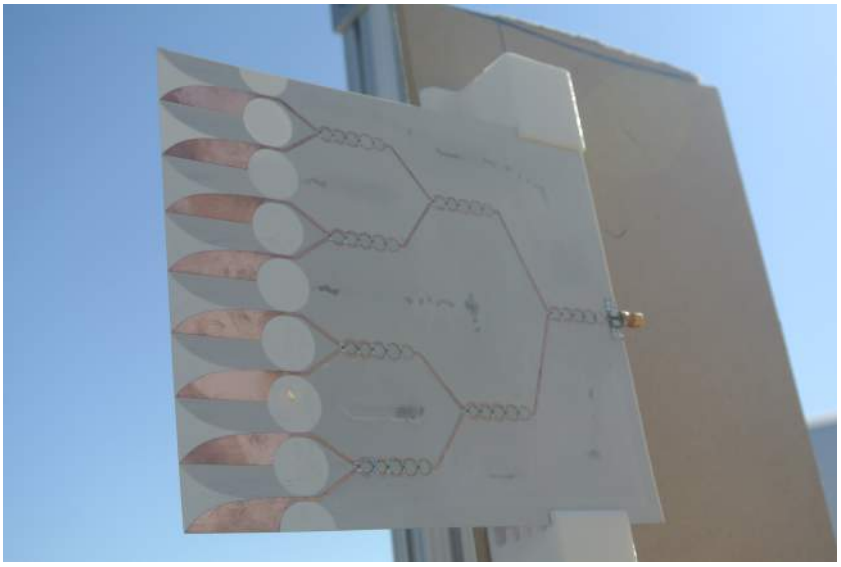

FIGURE 3.21: Fabricated Vivaldi array

3.2.3 RF Hardware

The apparatus uses an Agilent E5071B Vector Network Analyzer (VNA) provided by the Radar & Microwaves Laboratory as the radio source and data acquisition device. A step-up/step-down heterodyne at 8.5 GHz interfaces the VNA with the antennas, which operate over the measurement band of 8.53 to 13 GHz. Attenuation is measured with a repeatability of 0.01 dB, and the 4.5 GHz bandwidth supports a time resolution of roughly 250 ps, as calculated using equation 2.14, and a range resolution of 3.75 centimeters as calculated using equation 2.17. The VNA captures approximately eight frames per second, with 400 points in a frequency sweep, at an intermediate frequency (IF) bandwidth of 100 KHz.

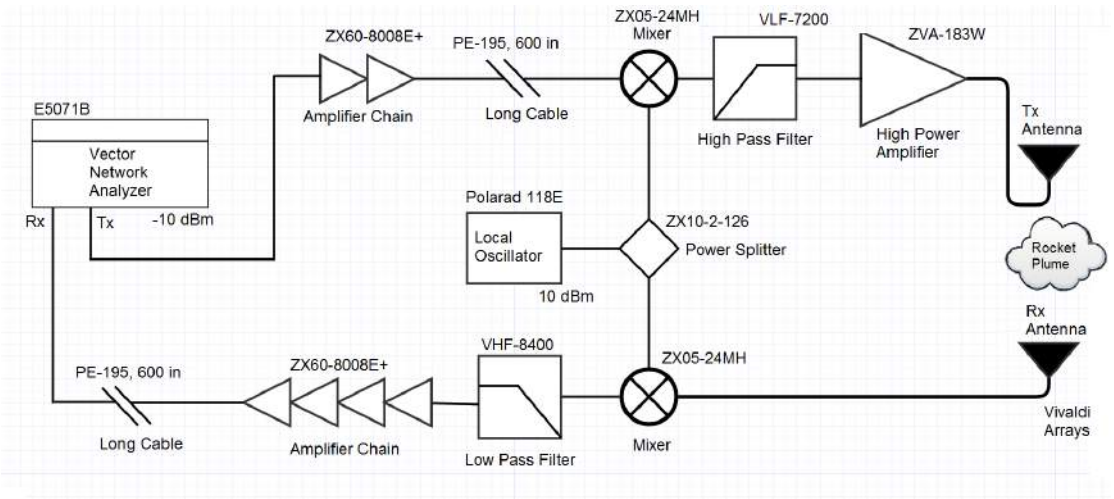

FIGURE 3.22: Block diagram of RF hardware operating in apparatus

Most of the RF hardware shown on the block diagram in figure 3.22 is composed of small components from Mini-Circuits with SMA connectors, fastened to a wooden board as shown in figure 3.23. A full list of components in the RF system can be found in Appendix A.

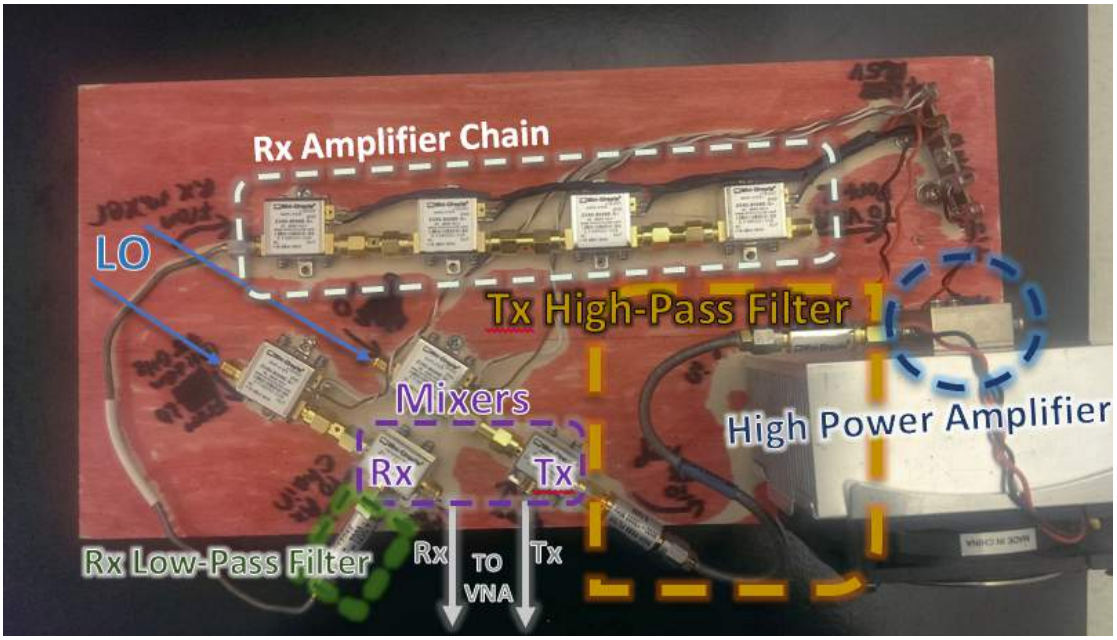

FIGURE 3.23: Amplifier-mixer board

The VNA and the Tx amplifiers are separated from the rest of the test apparatus by a long RG316 SMA-terminated cable, in order to enable the VNA operation at a safe distance away from the firing.

Other equipment used in the study is shown in figure 3.24 and 3.25.

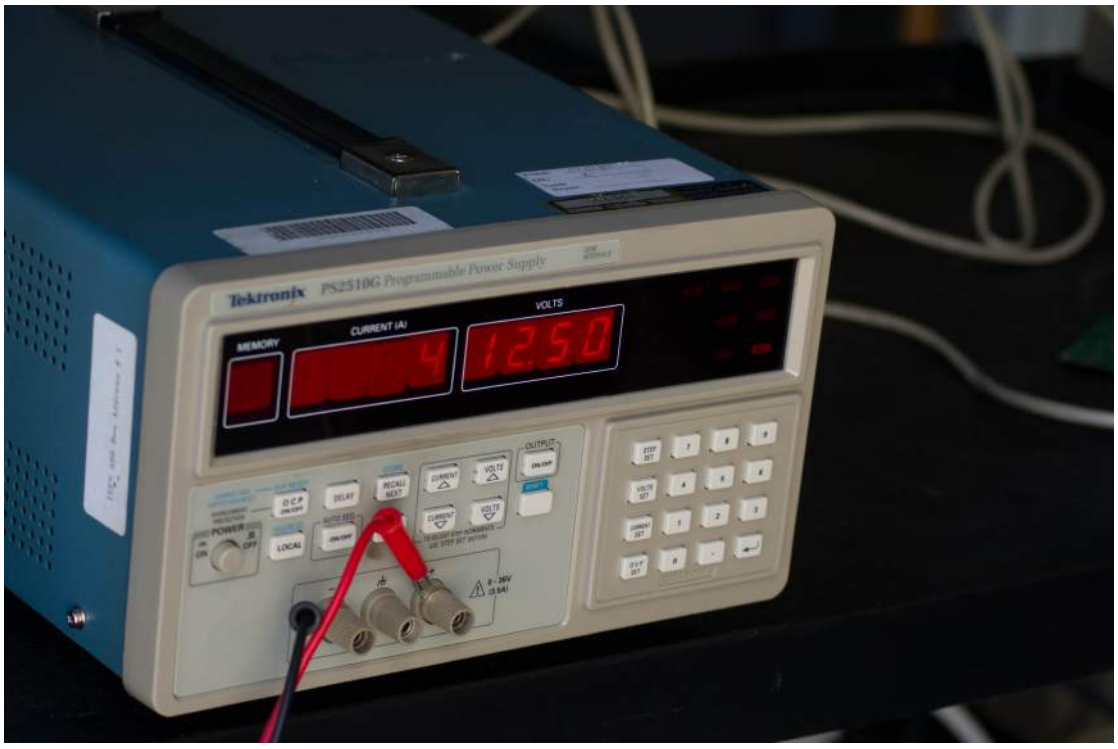

FIGURE 3.24: One of the set of three DC power supplies

FIGURE 3.25: Local oscillator unit

The system is shown as deployed in figure 3.26, in the garage area of the Lehman Science and Technology Building.

FIGURE 3.26: Readying the test equipment for a firing

3.2.4 Experimental Setup

Two sets of live fire experiments were conducted behind the Lehman Science and Technology Building by mounting the J and K-class motors on a large steel frame braced with a waste receptacle behind it. Access to the area during the firings was controlled by volunteers from the campus's local rocket societies: the Embry-Riddle Future Space Developers and Explorers Society (ERFSEDS), and the Experimental Rocket Propulsion Labs (ERPL).

A rough map of the area is provided in figure 3.27. The image marks a safe viewing distance, corresponding to the Tripoli Rocket Association Safe Launch Practices Manual's minimum safe distance for a non-complex research launch [28]. The VNA and its operator were placed under a roll-down blast door in the nearby Wind-Tunnel Laboratory.

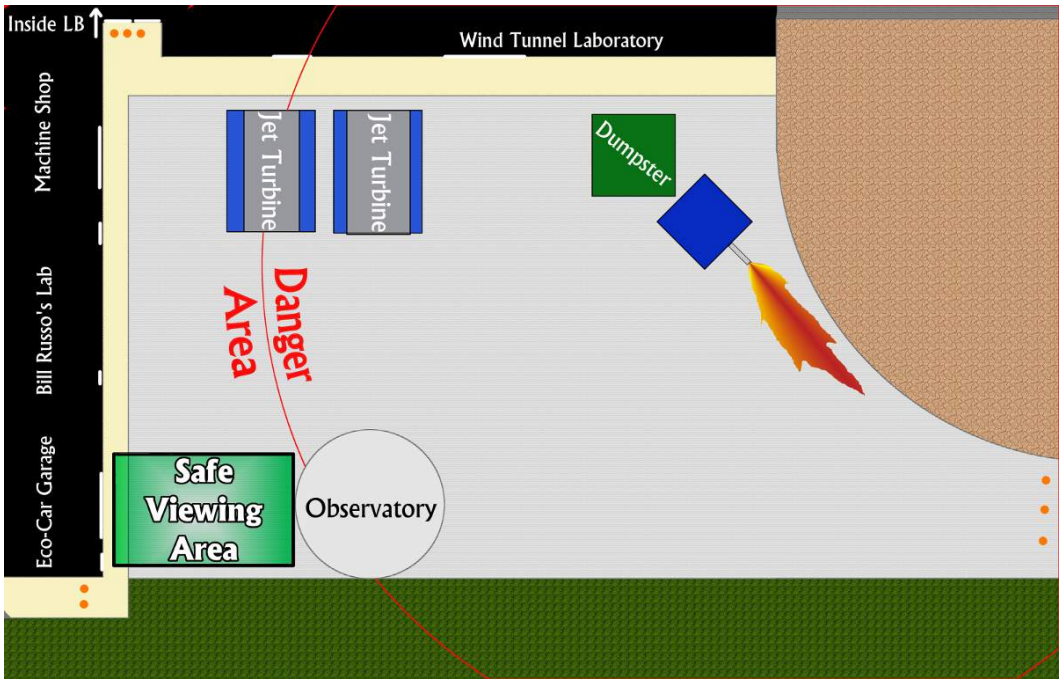

FIGURE 3.27: Test experiment setup behind the Lehman Science and Technology Building

Because of rainy weather during testing, the two sets of tests were conducted under a canopy as shown in figure 3.28 to protect exposed electronics.

FIGURE 3.28: Live testing under canopy

A close-up image of one of the rocket firings is shown in figure 3.29.

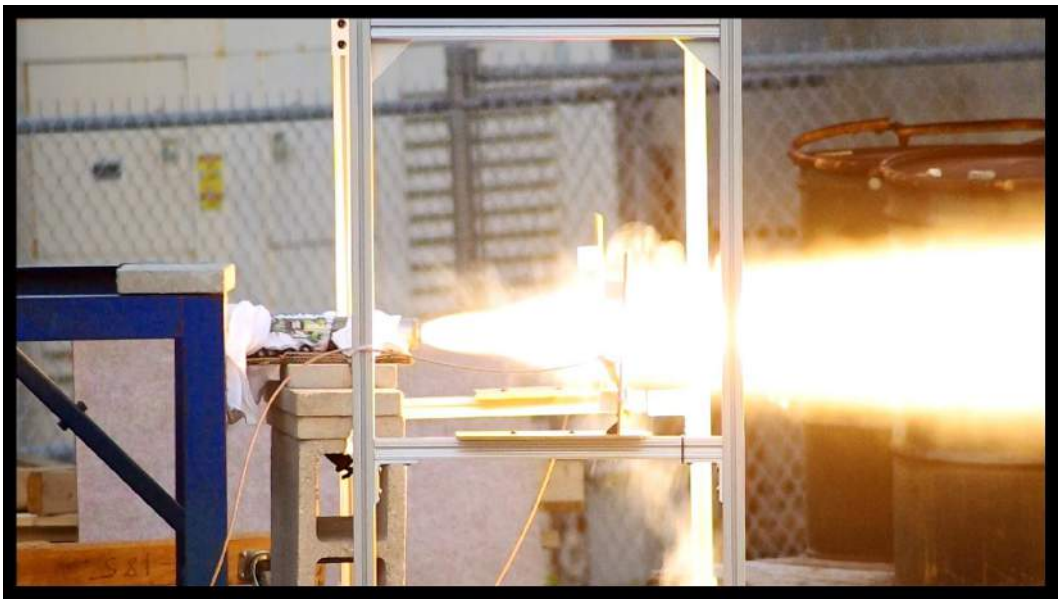

FIGURE 3.29: Closeup of rocket firing

3.2.5 System Response

The frequency-domain response of the entire system in the experiment setup can be seen in figure 3.30. Note that, because frequencies are heterodyned, the VNA is offset by 8.5 GHz from the transmitted signal.

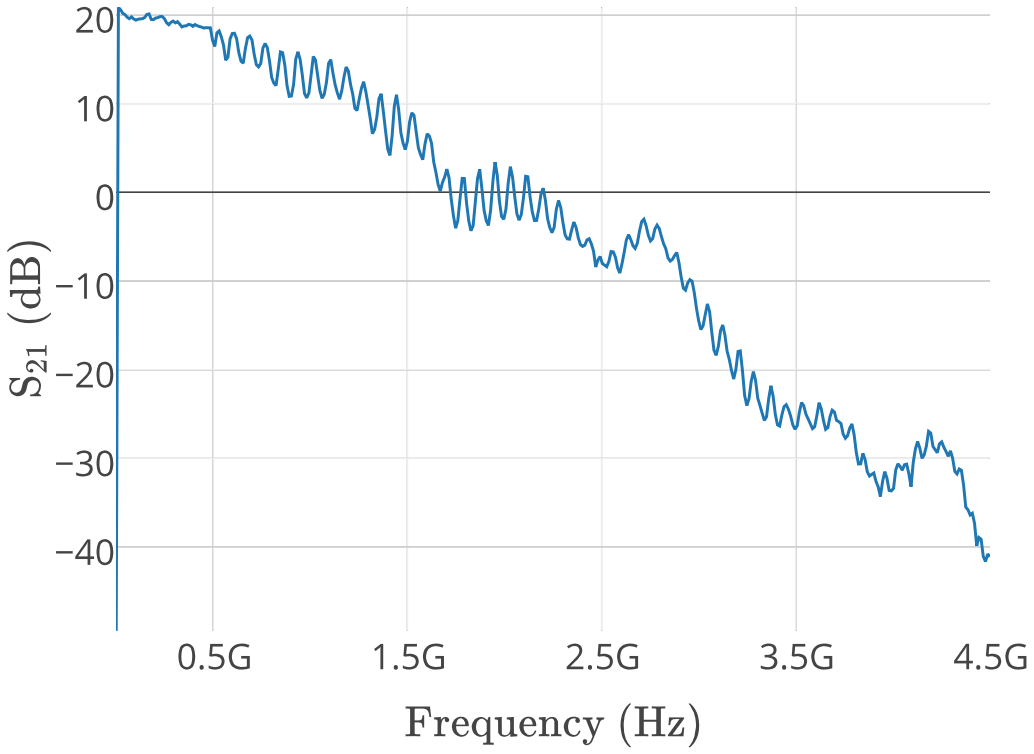

FIGURE 3.30: Frequency response of apparatus, S_{21} measured at VNA

The frequency response shows some aliasing due to the reflections in the environment. This seems to be confirmed after the elliptical section described in section 3.2.7 is added, since the frequency response at that time does not exhibit the same rippling behavior. While the antennas and power dividers obtaining other RF components with as wide a frequency range was cost-prohibitive. The high-pass filters introduce the most significant cutoff, and produce a favorable response from only 8-13 GHz.

The system time-domain response obtained after performing an inverse Fourier transform on the frequency-response data is shown in figure 3.31. The time-domain signal exhibits a strong main beam peak, as well as some reflections from the environment.

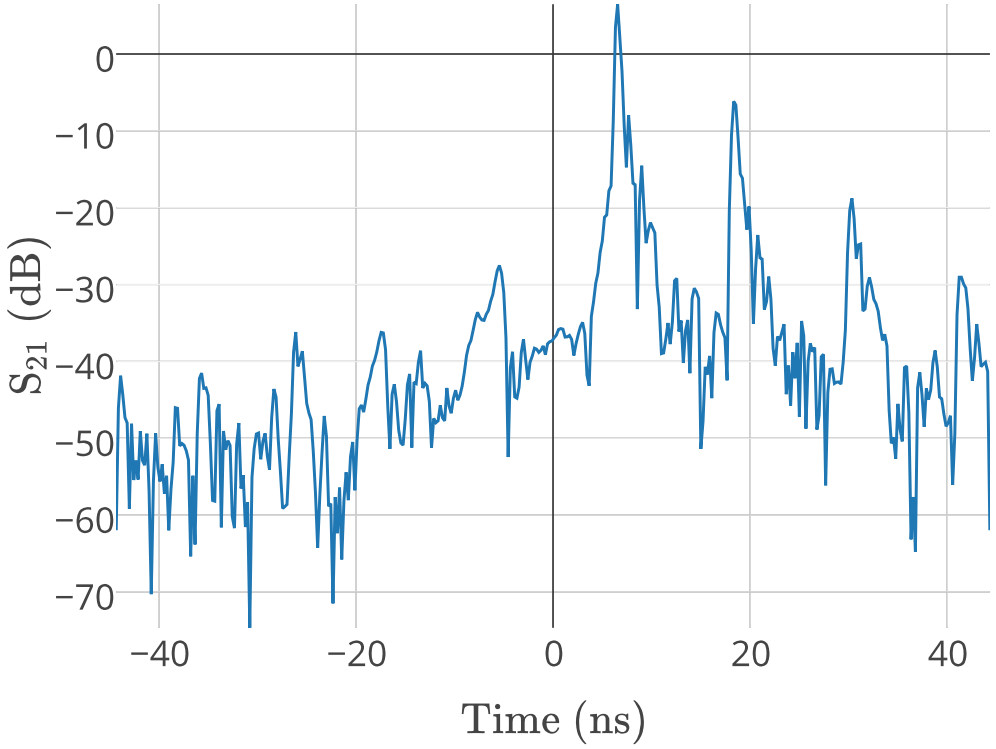

FIGURE 3.31: Time-domain response of apparatus, S_{21} measured at VNA

3.2.6 Antenna Testing

Using the thesis apparatus, a same-scale experiment of relative signal strength across a set of measured points was performed using a flat surface and large sheets of paper, as shown in figure 3.32.

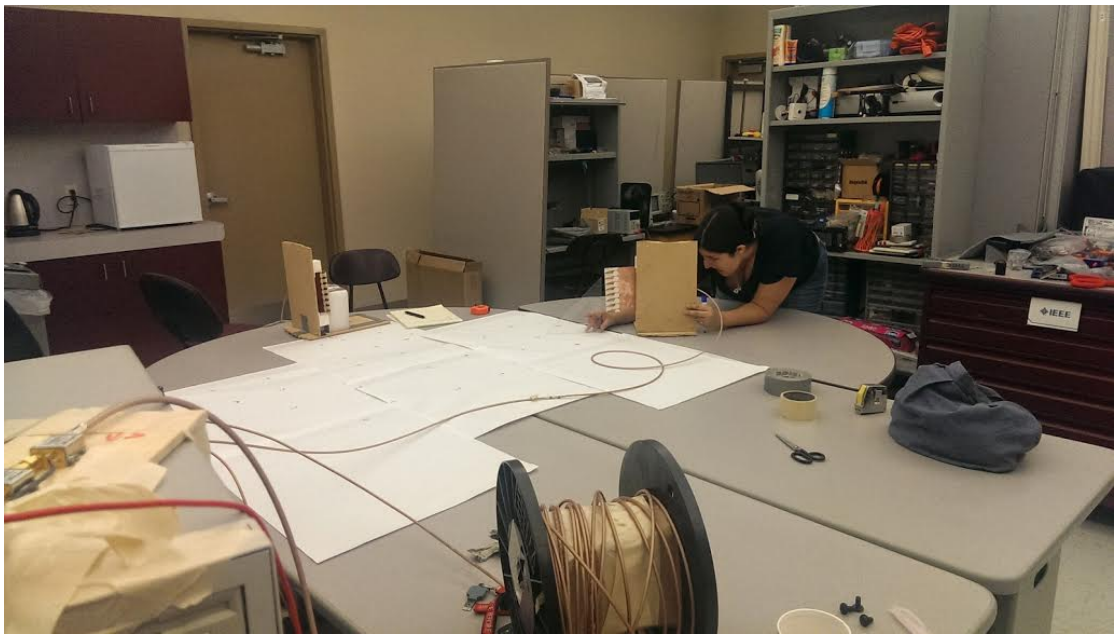

FIGURE 3.32: Measuring relative strength of the response of the entire apparatus with the help of a laboratory assistant

The scale of the distance in the measurements reflects a larger distance than in actual field tests. Despite the other components in the apparatus not being able to achieve as wide a bandwidth as the antennas and power splitters, the radiation pattern of the antennas is captured by mapping the strengths of the measurements on paper to a color by using image manipulation software. These colors are "blended" together using the Gaussian blur and smudge tools in the GNU Image Manipulation Program (GIMP). The results are in figures 3.33, 3.34, and 3.35.

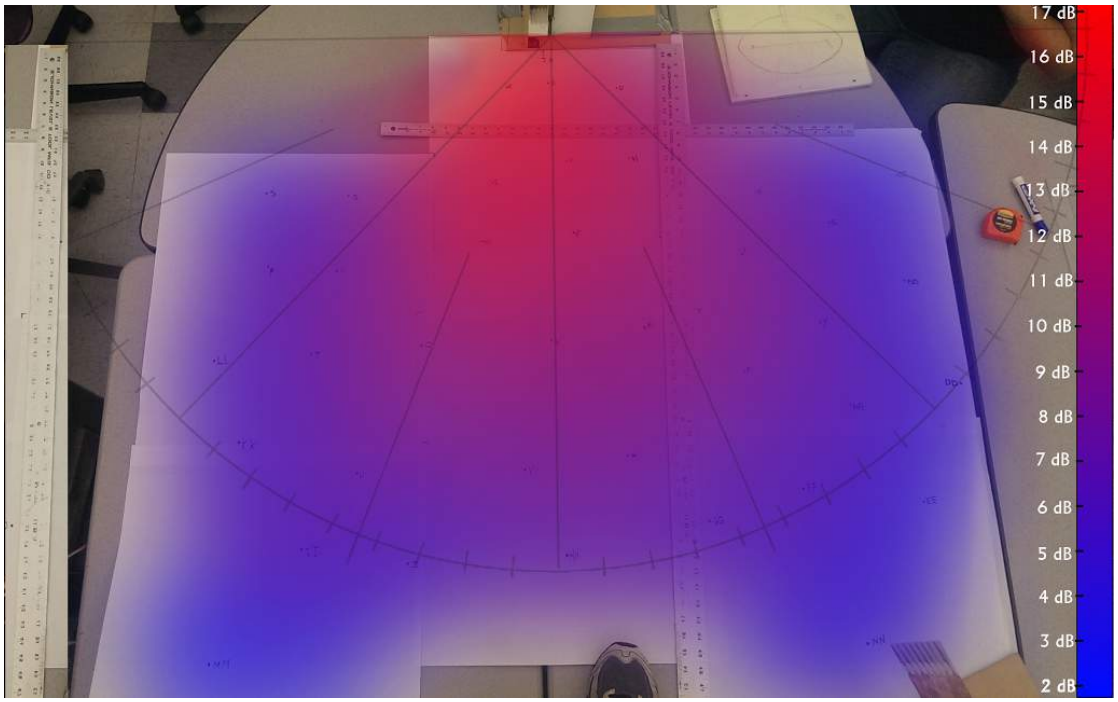

FIGURE 3.33: Relative strength of the response of the entire apparatus at 9.5 GHz

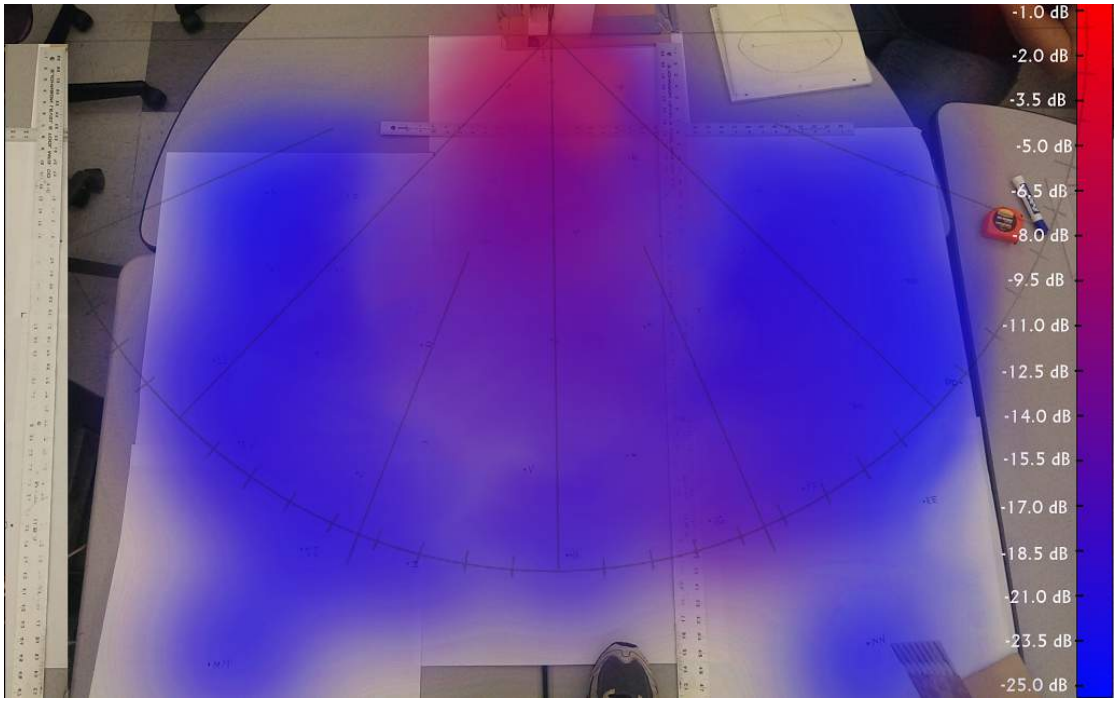

FIGURE 3.34: Relative strength of the response of the entire apparatus at 11.5 GHz

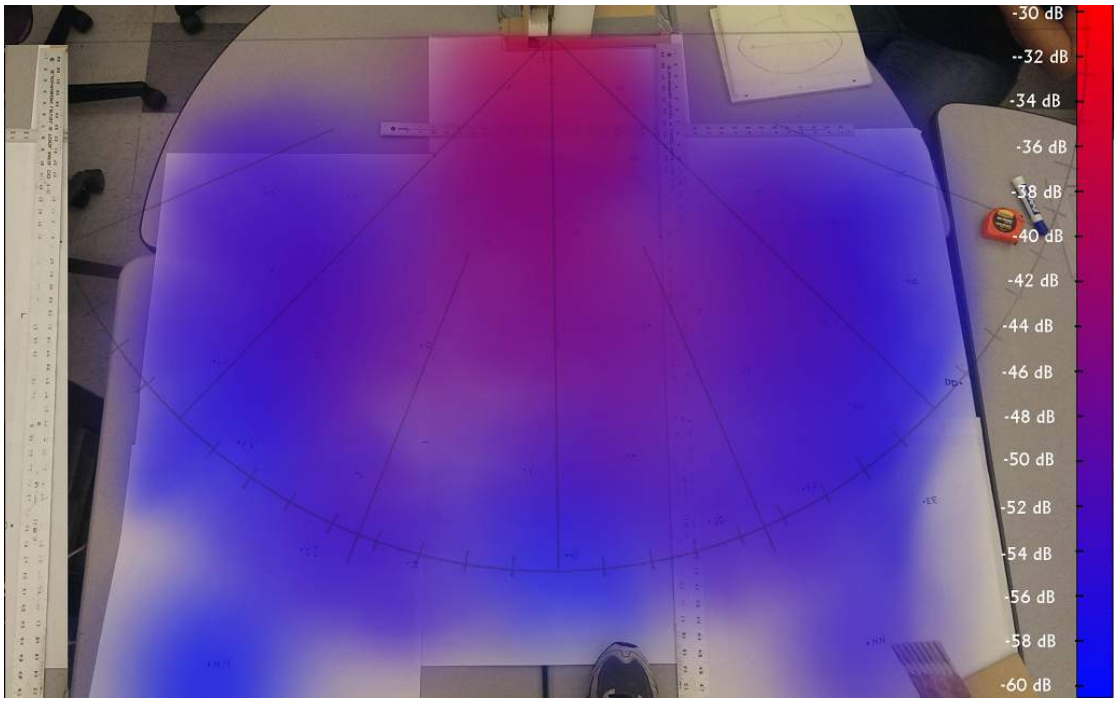

FIGURE 3.35: Relative strength of the response of the entire apparatus 16 GHz

3.2.7 Elliptical Reflector

The results shown in the first two motor firings (see section 4.2.1), demonstrated that the time domain response of the apparatus exhibited some reflections as shown in figure 3.31. These reflections were strong enough, and the apparatus's time resolution good enough, that it would be possible to measure their peaks over time if their path through the plume was known. To that end, a reflector was added to the apparatus, in order to introduce another set of data corresponding to an RF signal following a different path through the plasma. Since the apparatus can ideally sample 222 ps, the reflector is placed such that it is on a path approximately 1,110 ps away, assuming the speed of light c is approximately 3×10^8 m/s. The reflector consists of a 1 ft x 1 ft square metal sheet, mounted on a wooden frame forming a section of a ellipse with the two experiment antennas at the foci and the reflector at an approximately 45-degree angle to the receive antenna. A diagram showing approximate positioning can be seen in figure 3.36.

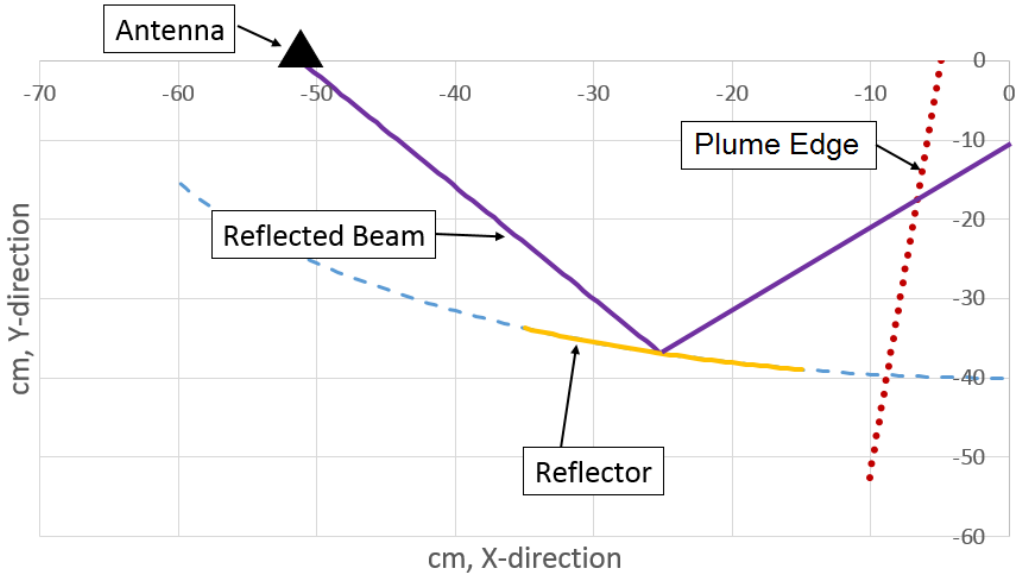

FIGURE 3.36: Elliptical RF reflector positioning. Note that this image shows half of the apparatus plane from above where 0,0 corresponds to halfway between the plume, in the antennas' direct path

The reflector itself can be seen in testing in figure 3.37.

FIGURE 3.37: Elliptical RF reflector during testing

The presence of the reflector in the apparatus adds a strong secondary main beam, as shown in the time response graph in figure 3.38.

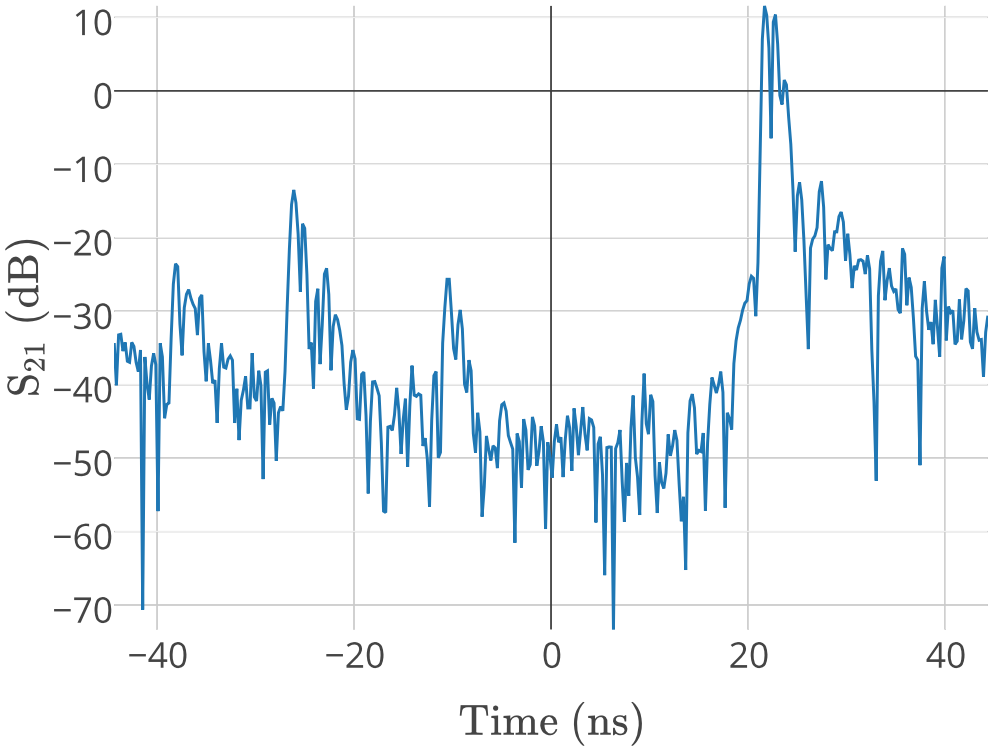

FIGURE 3.38: System time response after adding elliptical section. Note the two large peaks a few nanoseconds apart, corresponding to the main beam and the elliptical reflected beam

As a result, a noticeable null is introduced in the frequency response at about 1.9 GHz (which corresponds to 10.4 GHz actually transmitted) due to the intentional multipath interference.

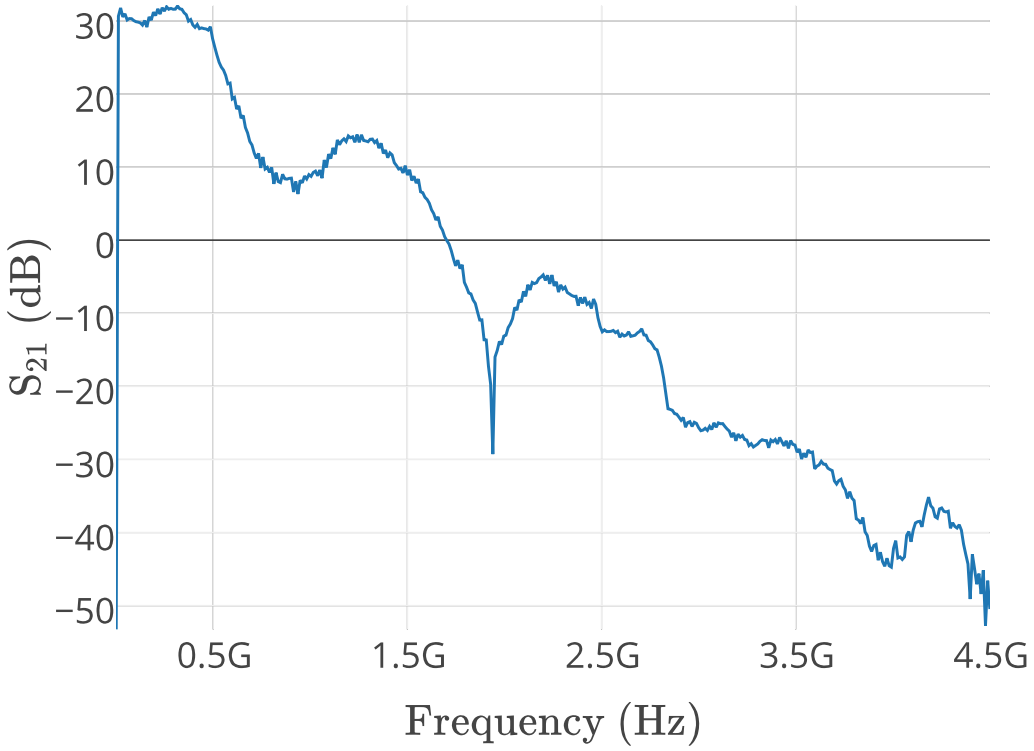

FIGURE 3.39: System frequency response after the elliptical is added shows multipath interference effects, including a null at approximately 1.9 GHz on the graph

3.2.8 Additional Test Instrumentation

In order to observe the effects of heat and antenna movement postulated in section 4.2.1, a microcontroller and a set of sensors was added to the third, fourth, and fifth firing that include a three-axis accelerometer, ambient temperature sensor, barometric pressure sensor, IR spot thermometer, and a distance sensor. The sensors and microcontroller were mounted to the same material the antenna sits on, and the distance sensor was aimed directly at the antenna to quantify how much it moved during a firing. A picture of the sensor instruments is shown in figure 3.40.

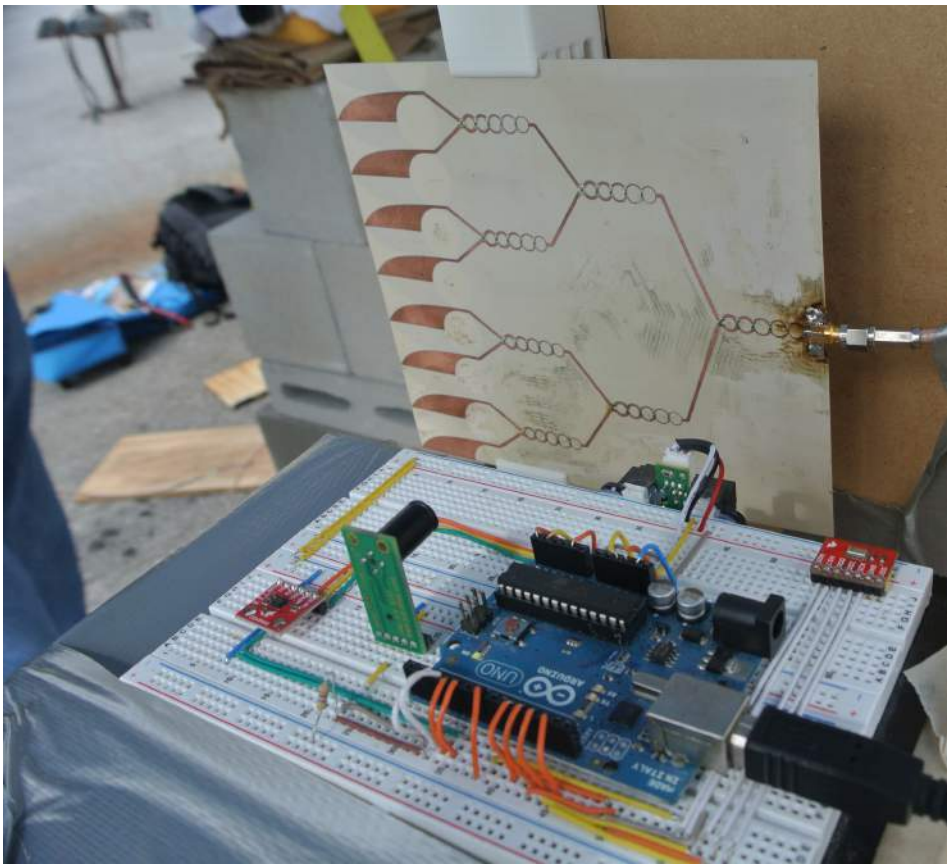

FIGURE 3.40: Instrumentation added to the second set of tests

An additional microcontroller was added near the RF amplifier-mixer board, shown in figure 3.23, to measure the temperature of components on the board using Type-K thermocouples while testing.

3.3 Software

The data generated by the VNA is saved in S2P (touchstone) files, which contain complex frequency-domain data in decibels. Data analysis is performed through Python scripts, which use the scikit-rf library for extracting information from the touchstone files. Time-delay analysis is an exception, being produced in MATLAB by thesis committee chair, Dr. William C. Barott.

The VNA is controlled via telnet by a laptop running a distribution of GNU/Linux with a tcl expect script, which is responsible for communicating with the VNA to store information, and ensuring that live data is being saved. Another Python script can display time or frequency information for those stored files.

The source code used in this thesis is found in Appendix B.

Chapter 4

Results

4.1 FDTD Results

4.1.1 CFD Values

Due to the extremely high simulation times on a detailed model, the simulated area on the FDTD simulation was confined to the area in the direct path of the plume. Using the CFD values from Coutu's thesis [5], simulations performed in Agilent EMPro were not able to duplicate focusing effects postulated by Coutu.

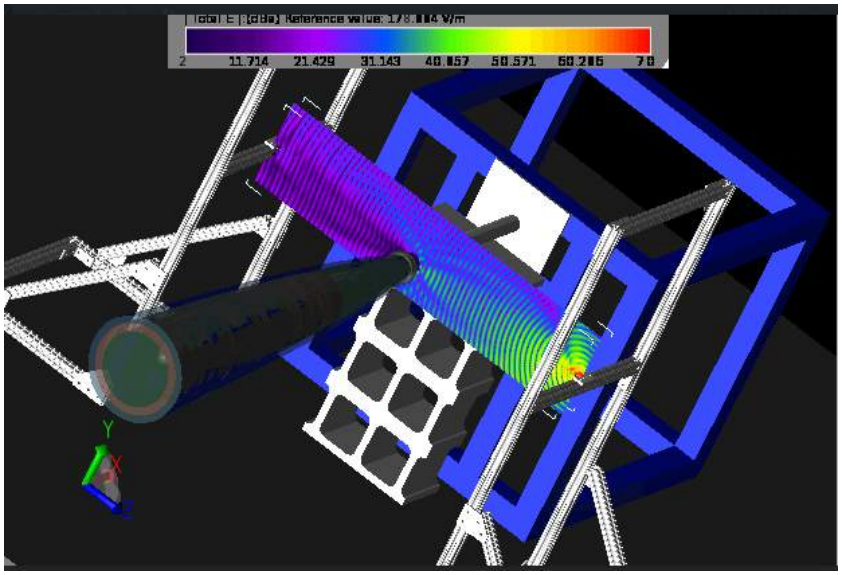

FIGURE 4.1: FDTD simulation of RF beam over the plume

Additionally, the attenuation prediction from the FDTD software did not match expected real-life results provided in the literature. This implies that either the model

generating values for N_e and v_e in CFD was inaccurate, or the FDTD model was inaccurate.

The simulated S_{21} model results are as shown on table 4.1.

	3 GHz	4 GHz	5 GHz	6 GHz	7 GHz	8 GHz
No Plume	-163.7	-150.033	-139.899	-131.271	-132.861	-129.308 dB
With Plume	-176.577	-160.751	-150.634	-141.865	-142.342	-140.176 dB
Difference	-12.877	-10.718	-10.735	-8.481	-9.481	-10.868 dB

TABLE 4.1: S_{21} values in decibels (dB) as predicted by the FDTD model, derived from CFD values

4.1.2 Experimental Values

After the results analysis from section 4.2.1, the model was re-made with the experimentally-derived values for N_e and v_e, producing the attenuation as shown in table 4.2.

	3 GHz	4 GHz	5 GHz	6 GHz	7 GHz	8 GHz
No Plume	-163.7	-150.033	-139.899	-131.271	-132.861	-129.308 dB
With Plume	-172.560	-155.323	-144.286	-135.670	-138.146	-132.061 dB
Difference	-5.86	-5.29	-4.387	-4.399	-5.285	-3.753 dB

TABLE 4.2: S_{21} values in decibels (dB) as predicted by FDTD model, derived from experimental values

In this model, the values for attenuation are still too high. While the model does not show any signal gain, it is closer to the real-life case than when the CFD-derived values were used, suggesting the experimental values are more accurate.

Additionally, the plume in the model seemed to be bending in the RF waves passing around it, which could imply a focusing effect. A still frame of the effect is shown in figure 4.2.

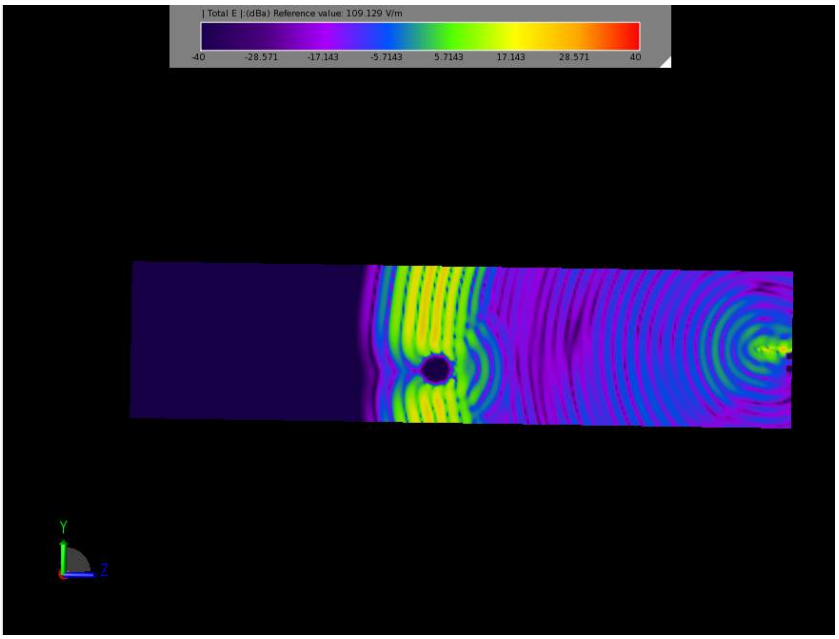

FIGURE 4.2: FDTD simulation showing some focusing effects

It is possible that the assumptions in the model are not entirely correct at lower frequencies, but using the experimental values has changed the model significantly in a way more closely resembling the effects of the plume. Additionally, the presence of slight focusing can partly validate some of the conclusions from Coutu's experiments.

4.2 Test Data

4.2.1 Motor Burns 1 and 2

The first live experiment was conducted on 9 Sepetember, 2014, with amateur sport rocket Level 2 High Power Rocket motors:

1. Cesaroni J295 54 mm 3-Grain Classic, and
2. Cesaroni J360 54 mm 3-Grain Skidmark.

The Classic motor has a total impulse of 1195 *Ns* and a burn duration of 4 s. The Skidmark motor has a total impulse of 1016 *Ns* and a burn duration of 2.8 s, with titanium particulates added to the grain for a more dramatic effect [29].

The first test performed used the Skidmark motor, and data recording was stopped a few seconds after the motor fire. By recording the peak value of the direct-path beam as described in section 3.2.5, the plot in figure 4.3 was produced.

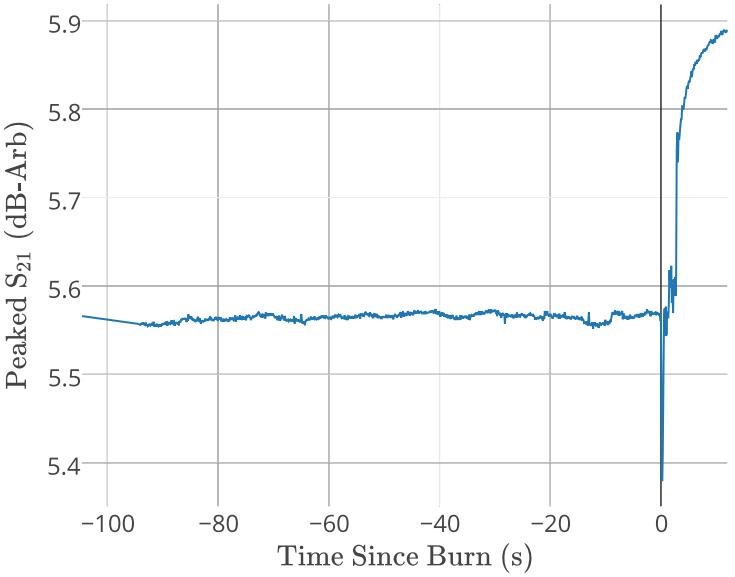

FIGURE 4.3: Skidmark burn direct-path strength over the burn

The response of the system shows a clear drop upon the motor firing. However, there appears to be an decaying increase in signal strength immediately after the motor fire. To analyze this behavior, the next motor fire's experiment recorded data for an extended period of time.

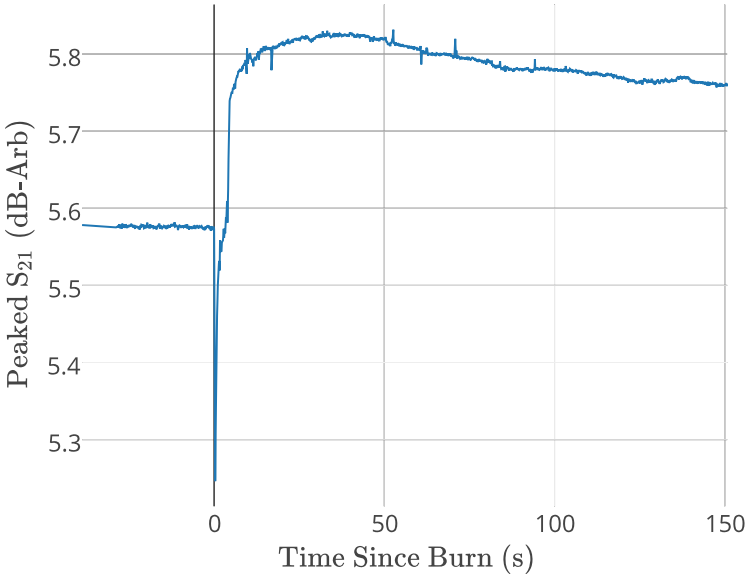

FIGURE 4.4: Classic burn direct-path strength over the burn

The same pattern appears in figure 4.4 as with the Skidmark motor, with a large initial drop, and a decaying increase in signal strength.

This pattern is similar to one encountered by Van der Beek [9] in a study of rocket plume attenuation using waveguides. The effect was attributed to heating of the air inside the waveguide, changing the permittivity of the medium.

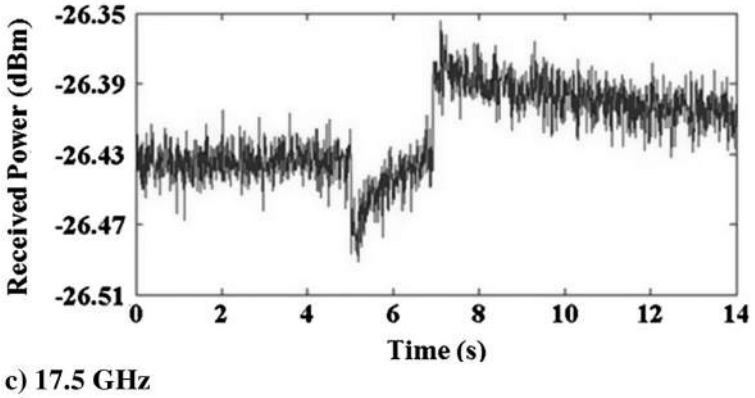

FIGURE 4.5: Van der Beek study results showing signal gain attributed to air temperature increase [9]

This effect could be a plausible explanation for the increased signal strength. The test was conducted during a hot day under a canopy because of the heavy rain during the experiment. It is possible that these conditions caused heating of the air under the canopy upon the rocket fire, with the air restoring to a normal temperature over time. Assuming these effects are true, the initial drop of the direct-path strength can be considered to be the attenuation due to the plasma.

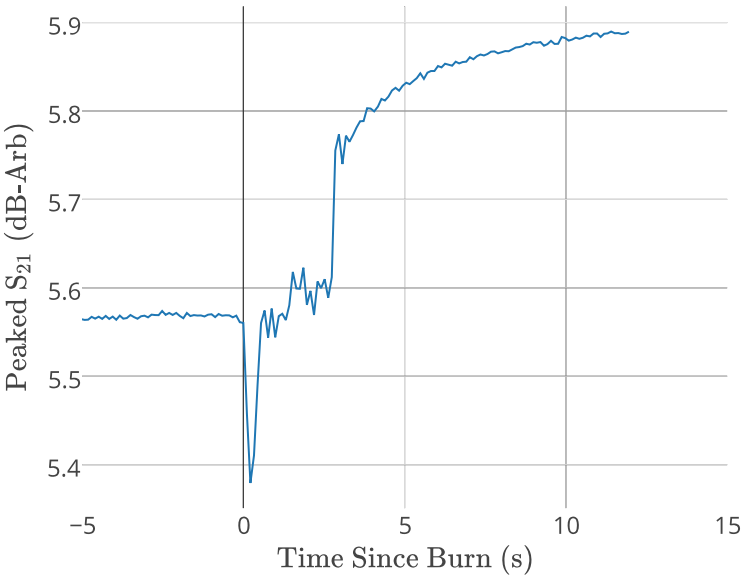

FIGURE 4.6: Skidmark burn direct-path strength over the burn, detail

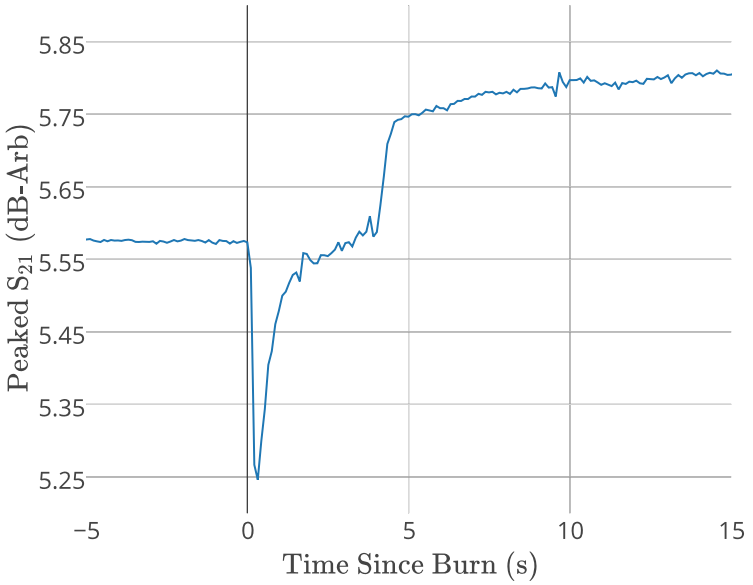

FIGURE 4.7: Classic burn direct-path strength over the burn, detail

Performing delay analysis of the two rocket motor burns produces the plots in figures 4.8 and 4.9.

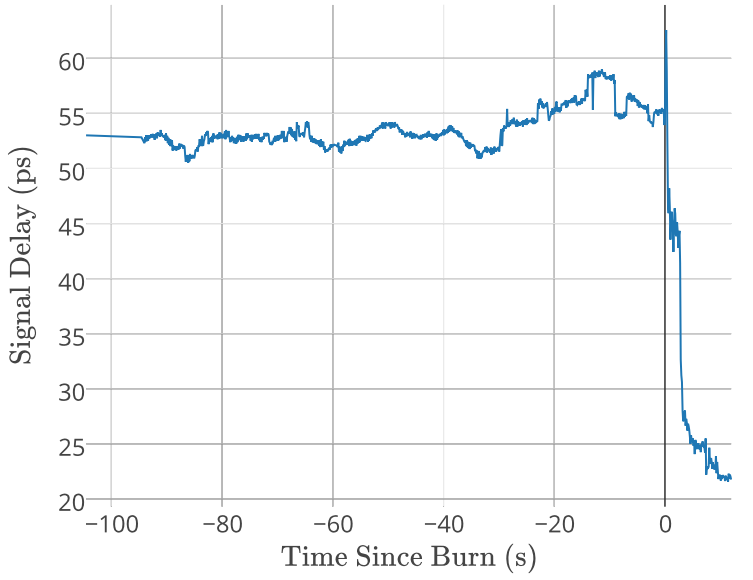

FIGURE 4.8: Time-delay required to reach peak value of time-domain response over time in Skidmark burn

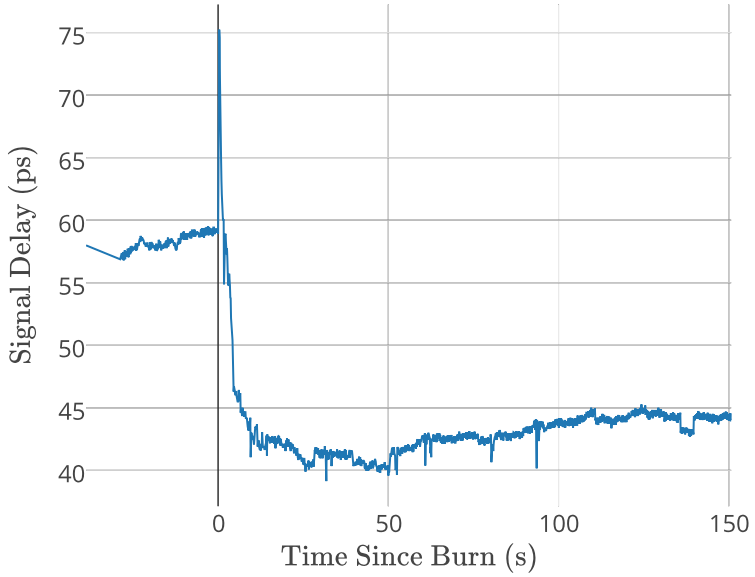

FIGURE 4.9: Time-delay required to reach peak value of time-domain response over time in Classic burn

For the delay calculations, a similar pattern emerges from the data as with the attenuation plots. Following the same assumptions, however, the peak delay can be considered the plasma effect before temperature effects take over.

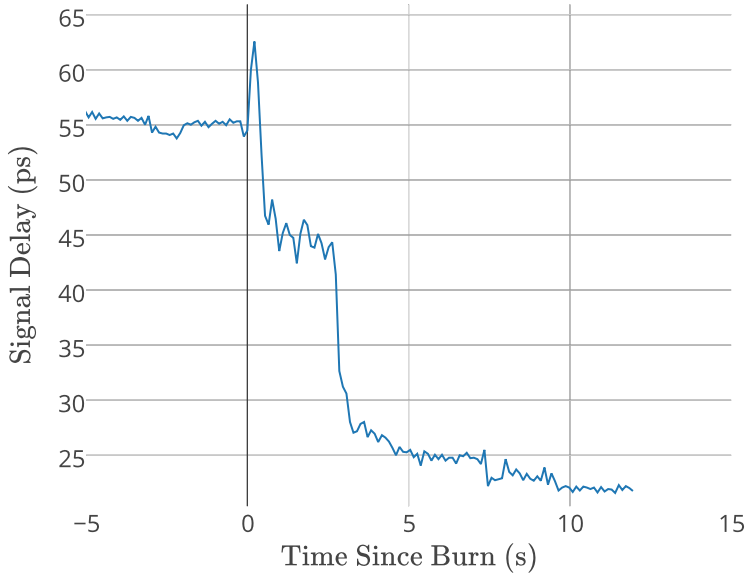

FIGURE 4.10: Time-delay response for Skidmark burn, detail

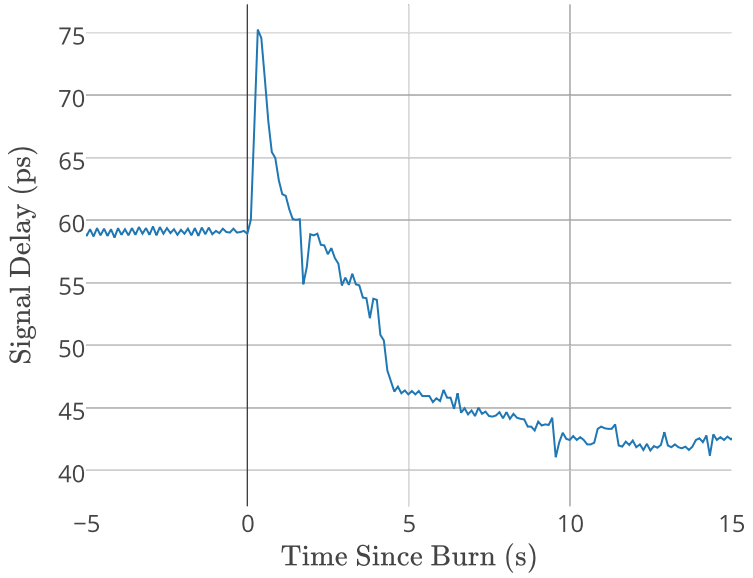

FIGURE 4.11: Time-delay response for Classic burn, detail

The experimental results are summarized in table 4.3.

	Attenuation	Delay
Classic	0.4315 dB	16.31 ps
Skidmark	0.2275 dB	8.24 ps

TABLE 4.3: Experimental results for motor burns 1 and 2

To find N_e and v_e, the attenuation and delay are used as described in Section 2.1.

However, since the radio frequency ω now spans a wide bandwidth, contending with an additional unknown to N_e and v_e in the propagation constant equations 2.10 and 2.9 resulted in an inability to determine a solution for N_e with those equations. However, using Smoot's model in equation 2.13 and the refractive-index solution in 2.18, two solution sets can be generated and plotted against each other to find a solution for N_e over a range of frequencies.

The solution for N_e in equation 2.18 in terms of the delay, plume width y, and v_e is

$$N_e = \frac{-c^2\left(c^2\left(delay\right)^2\omega + 2c\left(delay\right)^2\omega y - j\epsilon_0 v_e y^2 + \omega y^2\right)}{q_e^2\left(delay\right)^2\epsilon_0 m_e v_e^2 \omega y - \epsilon_0 m_e v_e^2 \omega y^2}. \tag{4.1}$$

The solution for N_e in equation 2.13 in terms of the attenuation, L_{dB}, y, and v_e is as described in equation 4.2,

$$N_e = \frac{2.17391 L_{\mathrm{dB}} \left(v_e^2 + \omega^2\right)}{y v_e}. \tag{4.2}$$

Plotting both solutions with varying values of v_e as iterated over ω produces the graphs in figures 4.12 and 4.13. In these plots, the solid lines represent solutions using equation 4.1, and the dotted-line solutions represent the results using equation 4.2. Both solution sets seem to be inversely related in terms of v_e, which allows for convergence between them for the right values. It follows that N_e should lie between two lines of either solution at a convergence value of v_e.

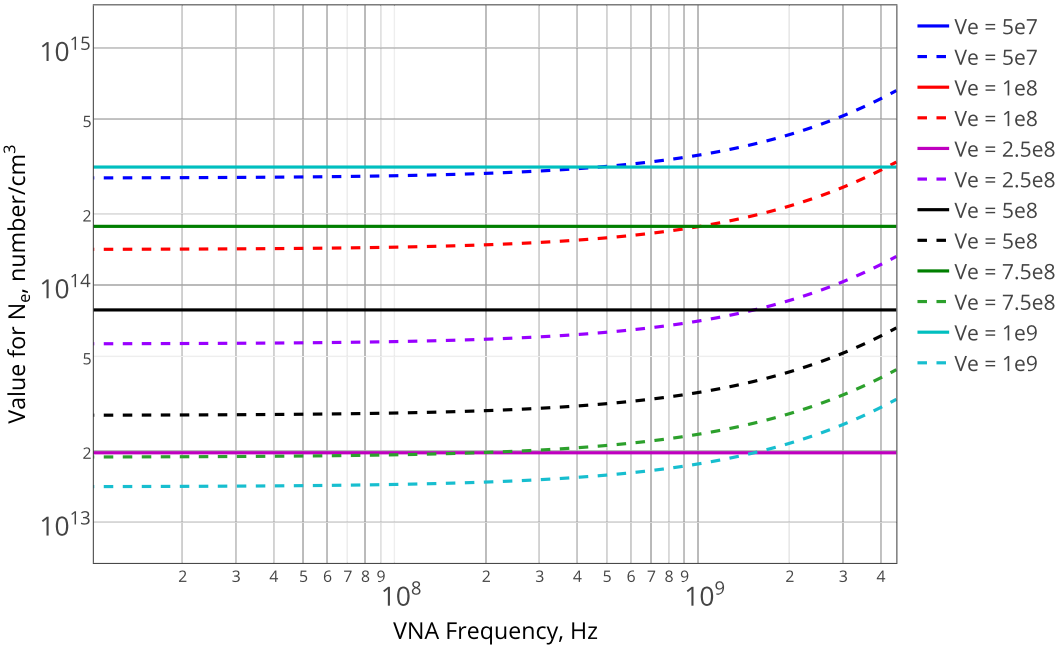

FIGURE 4.12: Solution curves for Skidmark burn

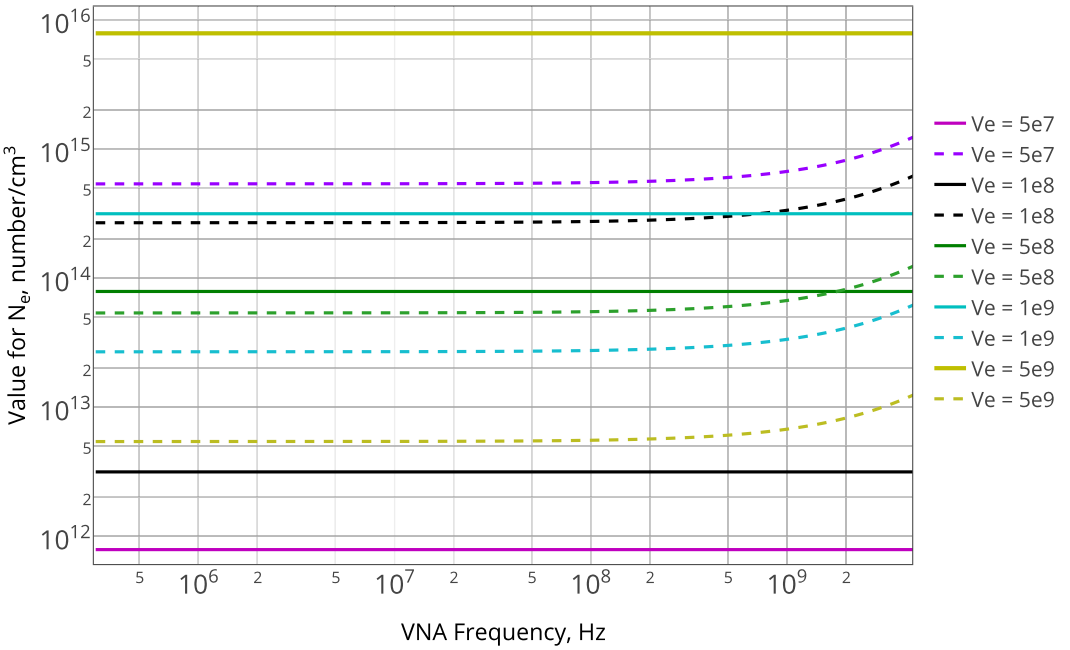

FIGURE 4.13: Solution curves for Classic burn

The solution for the Skidmark burn has a convergence between a v_e value of 2.5×10^8 and 5×10^8, where the Classic burn seems very close at a v_e of 5×10^8. The solutions for both of the motor burns are summarized in table 4.4.

	N_e	v_e
Skidmark	2.8843×10^{13} - 5.7032×10^{13}	4×10^8 Hz
Classic	5.6225×10^{13} - 7.8552×10^{13}	5×10^8 Hz

TABLE 4.4: N_e solutions for both of the motor burns in the first experiment

4.2.2 Motor Burns 3, 4, and 5

The next experiment was constructed with the addition of the elliptical reflector and instrumentation to the apparatus as described in sections 3.2.7 and 3.2.8. The primary focus of the second experiment was to experimentally confirm whether the very small delays and attenuation observed in the system were caused by the plume or by the antennas being moved by the rocket motor's firing. The motors used were the following:

1. Cesaroni J1520 54 mm 3-Grain VMax,
2. Cesaroni J140 54 mm 3-Grain White Longburn, and
3. Cesaroni K360 54 mm 3-Grain White.

The VMax motor has a total impulse of 1093 *Ns* and a burn duration of 0.7 s. The Longburn motor has a total impulse of 1211 *Ns* and a burn duration of 8.5 s, and the White motor has an impulse of 1266 *Ns* with a burn duration of 3.5 s [29].

The weather on the day of the test was colder than the previous test day. The canopy from the first experiment was still used because of a forecasted chance of rain; however, no rain occurred during testing.

The raw data collected by the added instrumentation during the first and second motor burns in the experiment is plotted in figures 4.14 - 4.18.

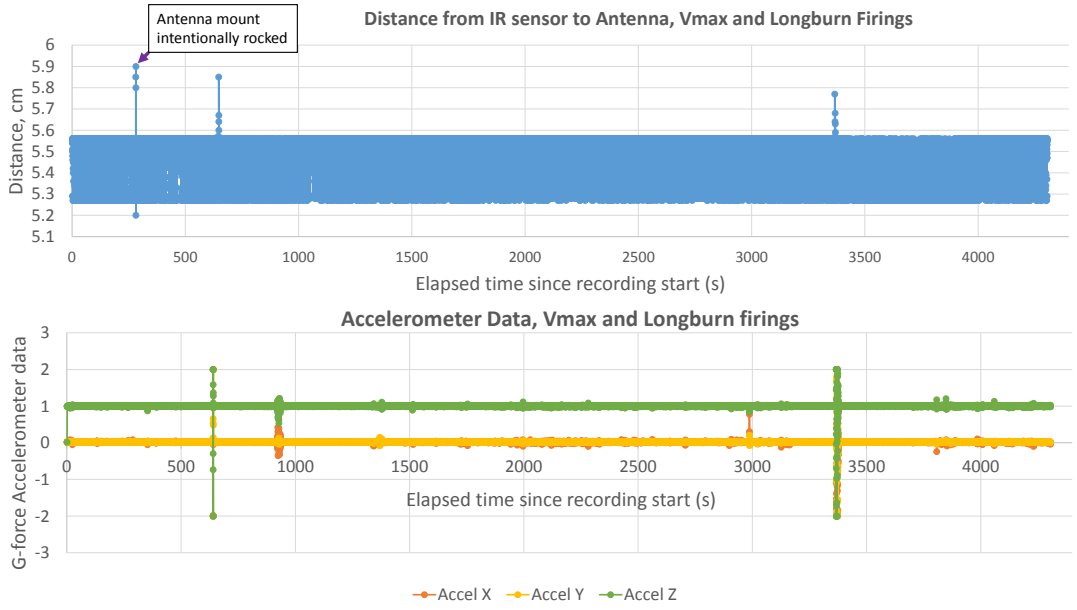

FIGURE 4.14: Collected instrumentation data - IR sensor distance, 3-axis accelerometer G-force for VMax and Longburn firings

The top graph of distance as measured by the IR sensor from itself to the antenna shows clearly when the antenna mount was intentionally moved. This was done before the VMax firing to simulate the effects of the rocket's pressure on the apparatus, in order to determine the impact on attenuation and delay from antenna movements. The other movements correlate well between antenna movements as recorded by the IR distance sensor and the accelerometer readings. The VMax and Longburn firings occurred at 650 s and 3370 s respectively. Between the Longburn and White firings, the microcontroller recording the data reset and time indexes were reset. The White firing occurred in the next set of data at 825 s.

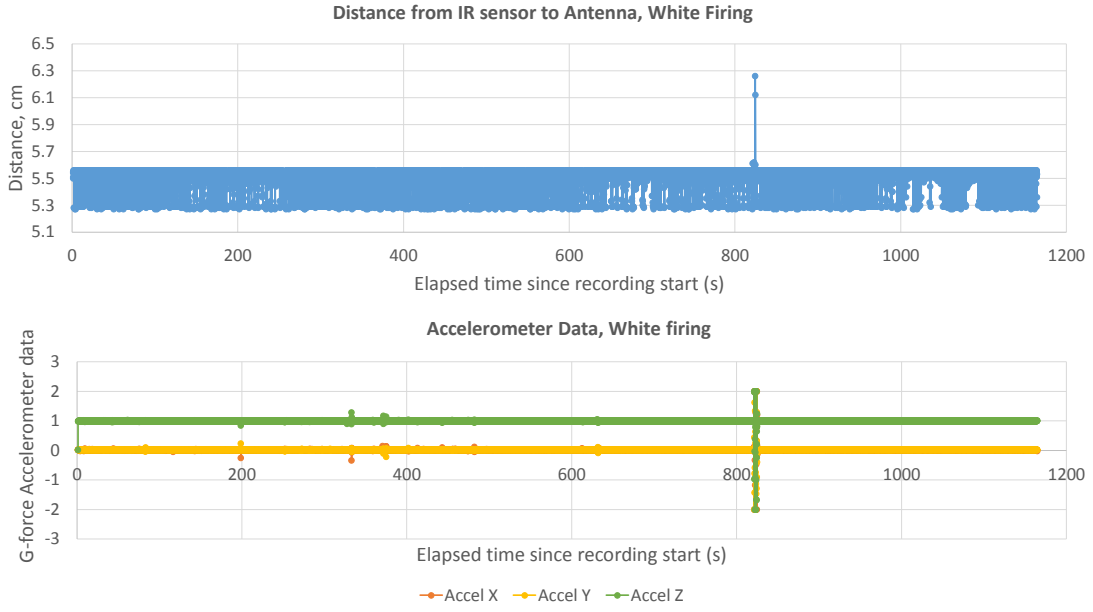

FIGURE 4.15: Collected instrumentation data - IR sensor distance, 3-axis accelerometer G-force for White firing

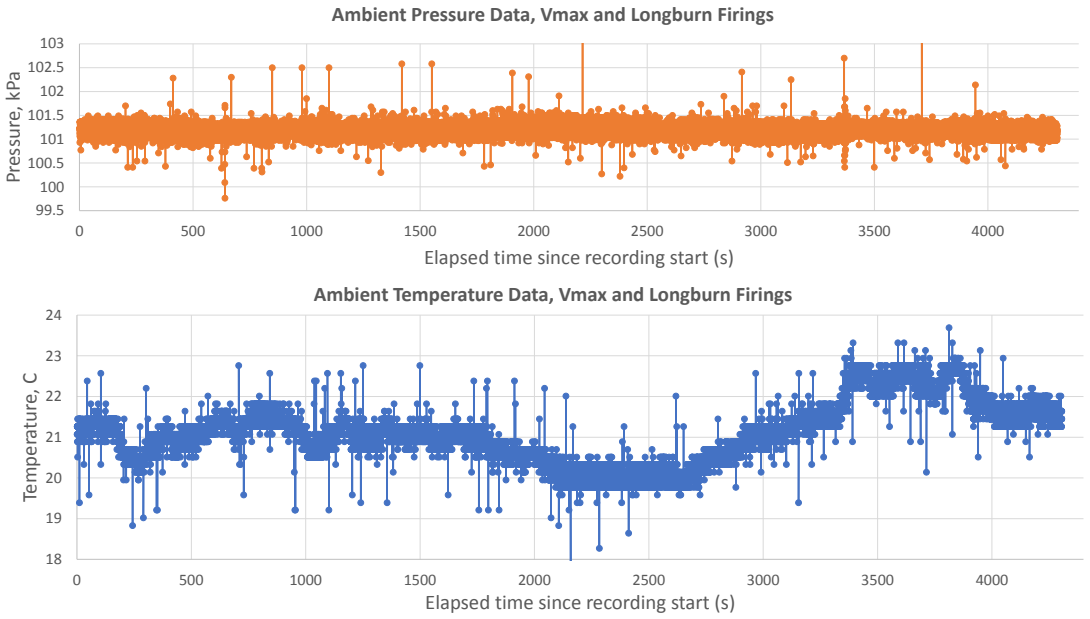

FIGURE 4.16: Collected instrumentation data - ambient temperature and pressure data for VMax and Longburn firings

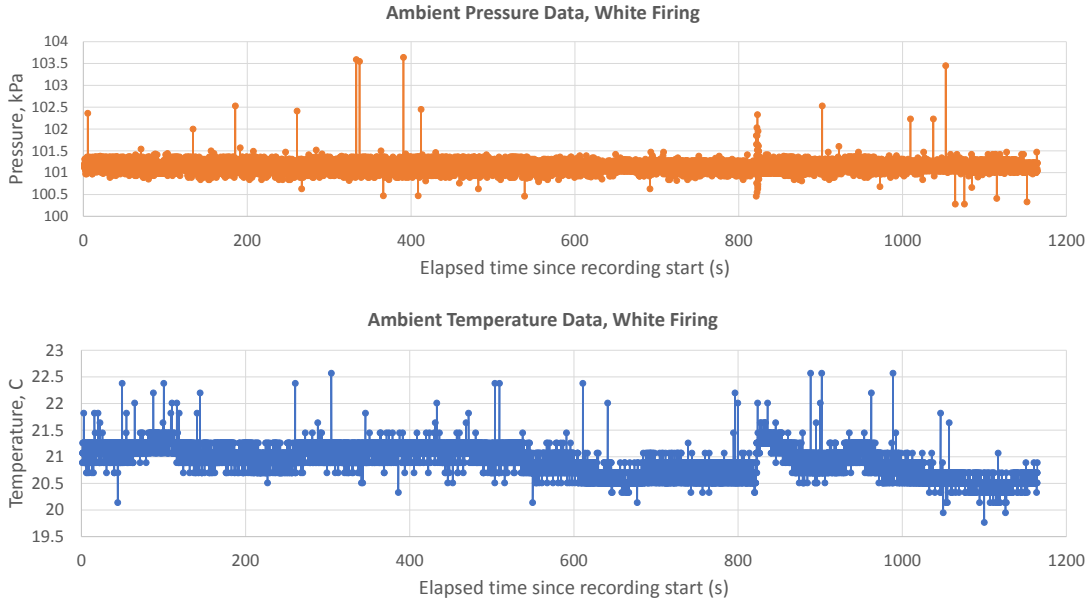

FIGURE 4.17: Collected instrumentation data - ambient temperature and pressure data for White firing

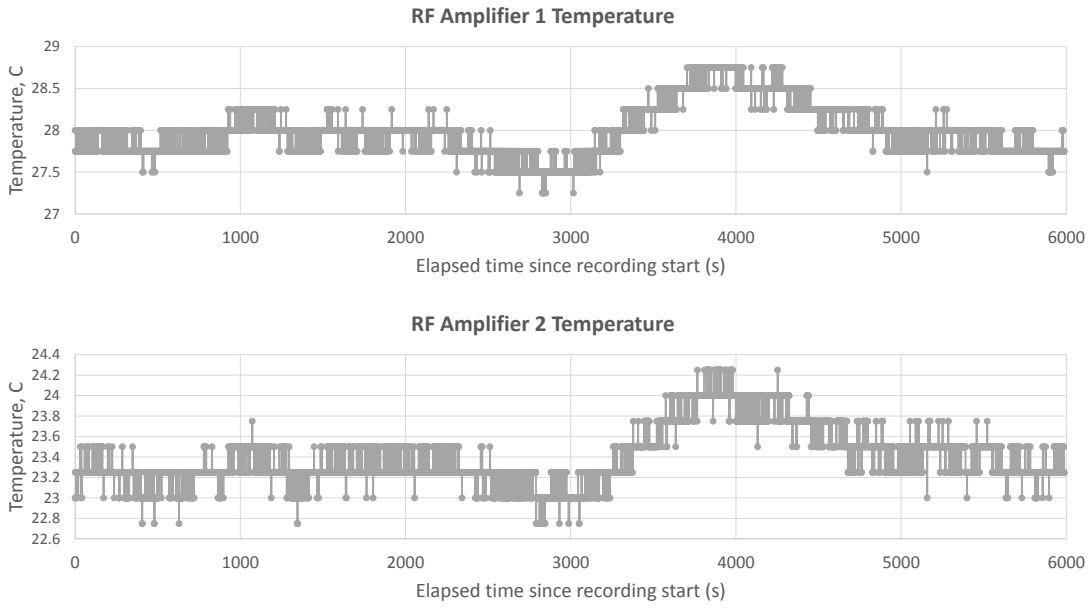

FIGURE 4.18: Collected instrumentation data - RF amplifier temperature for VMax, Longburn, and White firings.

When aligned, the instrument data seem to correlate between motor firings. The data for temperature and pressure don't exhibit strong correlation in the first motor burn, most likely due to its short fire duration. Unfortunately, the IR spot thermometer malfunctioned during the experiment and no data was gathered. While ambient temperature is measured adjacent to the antennas and not between, a small temperature increase can be observed in the data at the time of motor firings.

4.2.2.1 Direct-Path Measurements

The S_{21} direct-path curves for the first firing with the VMax motor are as shown in figure 4.19.

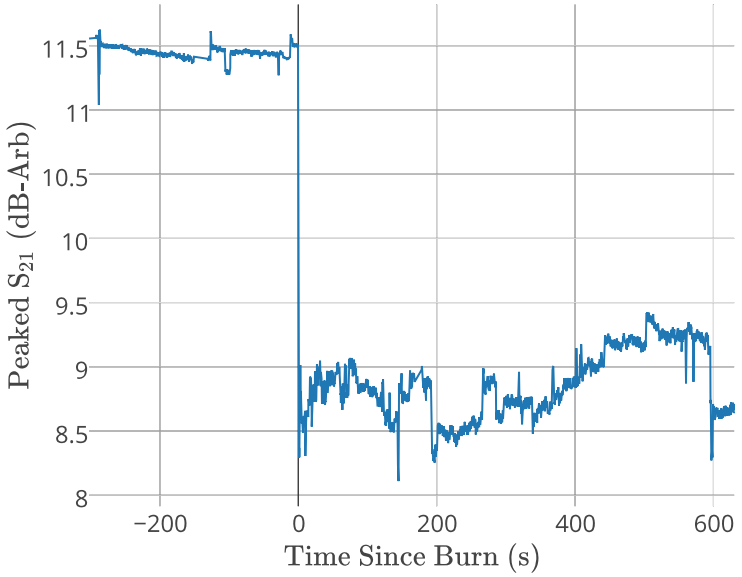

FIGURE 4.19: VMax direct-path strength over the burn

In the attenuation plot for the VMax fire, a small, momentary fluctuation can be seen at the beginning of recording, believed to be the intentional antenna movement. The rocket fire happens at approximately 300 seconds into recording, and seems to have a much more pronounced drop.

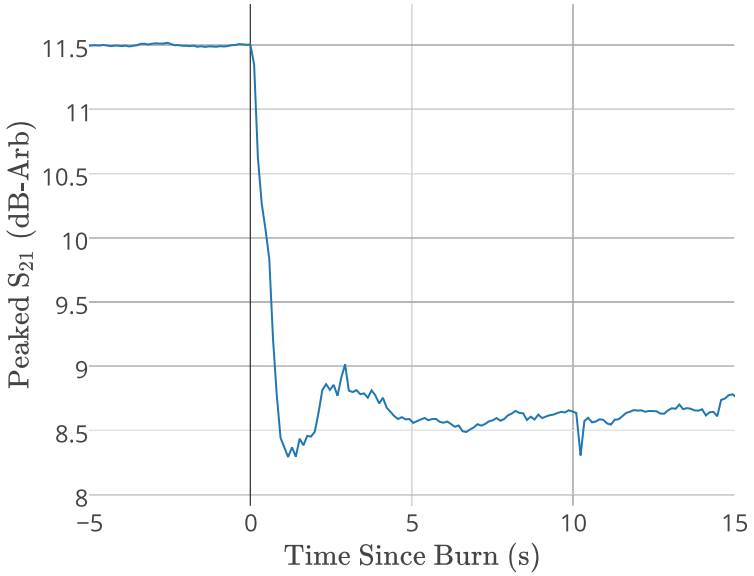

FIGURE 4.20: VMax direct-path strength over the burn, detail

Curiously, patterns of decaying gain are not evident in the data gathered in the VMax firing, and the post-firing signal levels seem significantly lower than on the initial response. Upon reviewing video recordings of the experiment, the multipath reflector

is seen shifted slightly by the thrust of the VMax motor, which may account for the discrepancy.

The delay analysis plots for the VMax motor are as illustrated in figures 4.21 and 4.22.

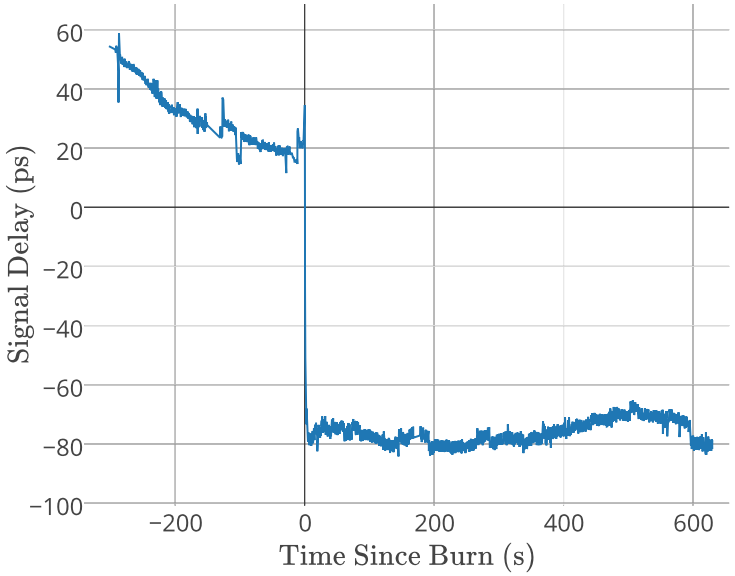

FIGURE 4.21: VMax direct-path delay over the burn

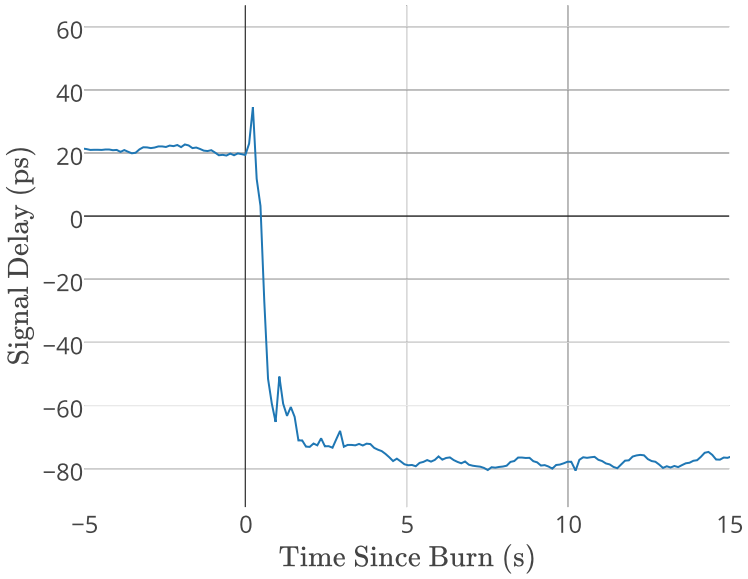

FIGURE 4.22: VMax direct-path delay over the burn, detail

The same effect as with the attenuation plots can be observed in the delay - a very pronounced delay in the data, much more so than in previous firings. This is also

believed to be an artifact of the multipath environment. The collected signal data for the Longburn and White motors can be found in figures 4.23 - 4.30.

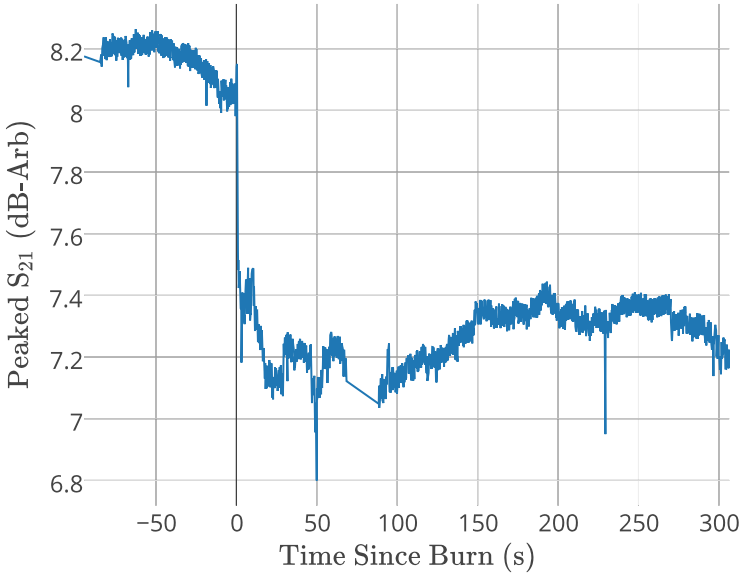

FIGURE 4.23: Longburn direct-path strength over the burn

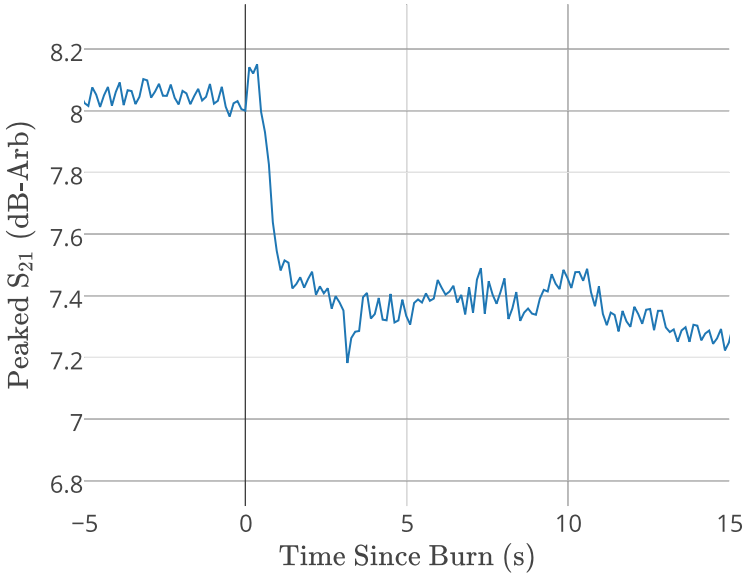

FIGURE 4.24: Longburn direct-path strength over the burn, detail

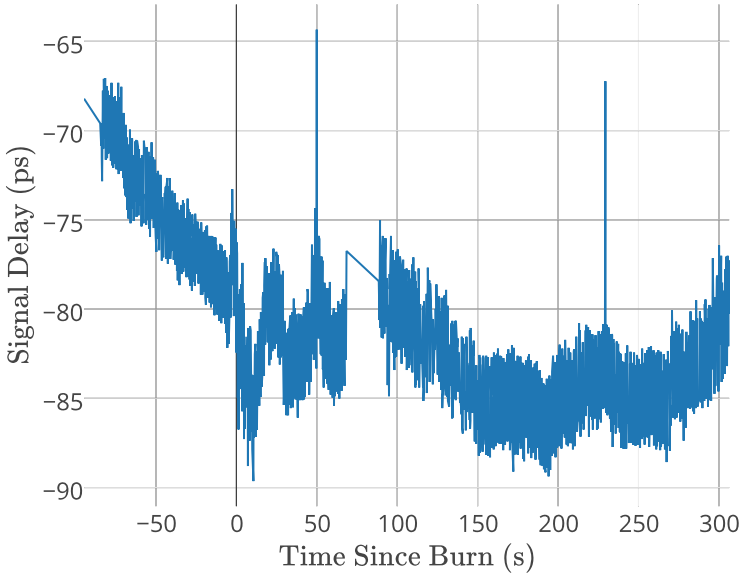

FIGURE 4.25: Longburn direct-path delay over the burn

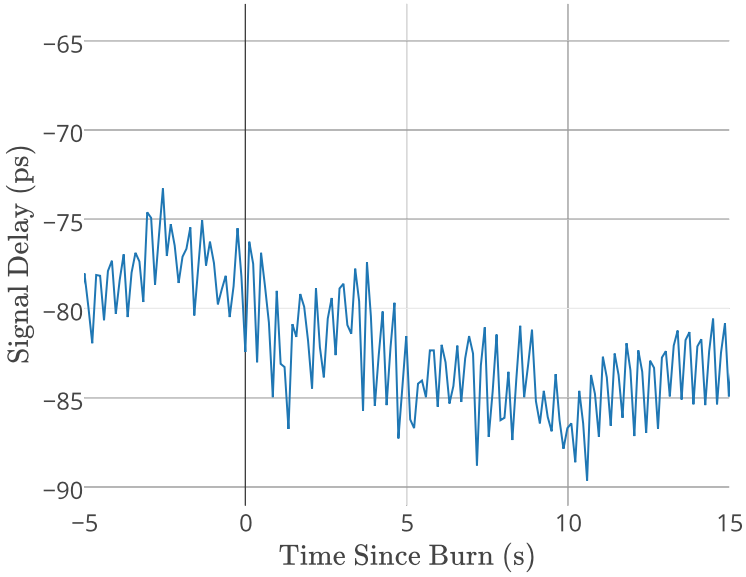

FIGURE 4.26: Longburn direct-path delay over the burn, detail

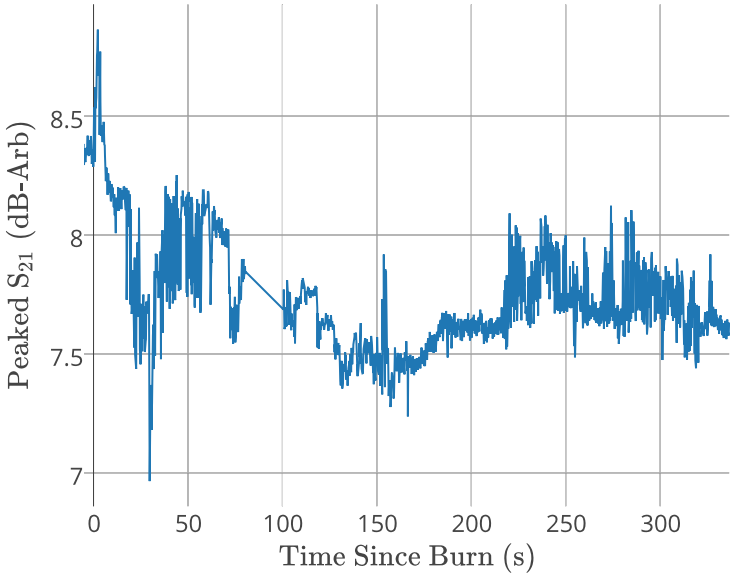

FIGURE 4.27: White direct-path strength over the burn

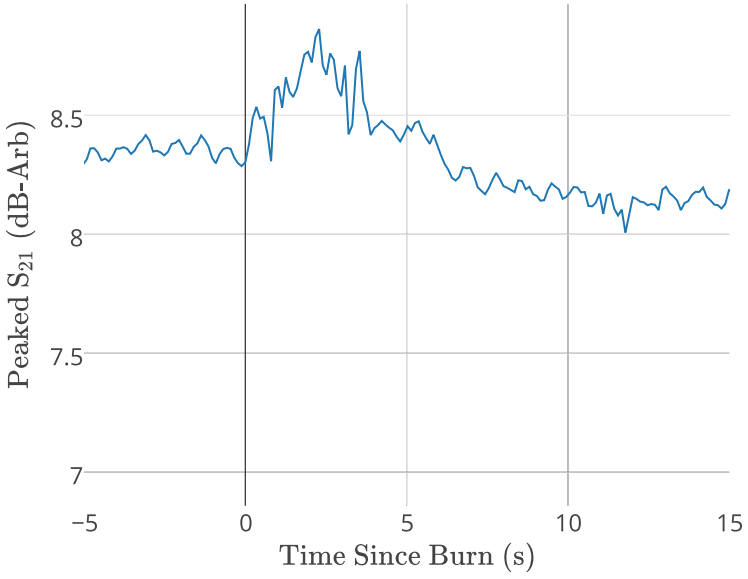

FIGURE 4.28: White direct-path strength over the burn, detail

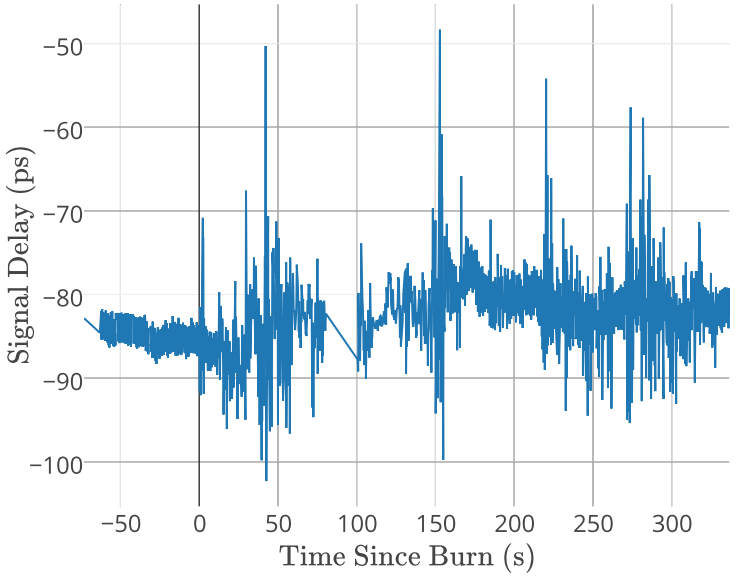

FIGURE 4.29: White direct-path delay over the burn

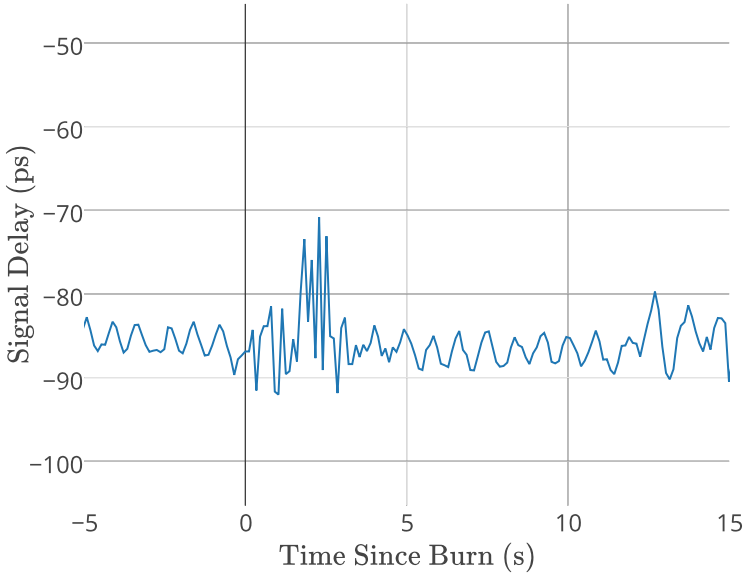

FIGURE 4.30: White direct-path delay over the burn, detail

The data for the Longburn and White firings exhibit an unclear source of oscillation due to the multipath distortions. A clear number for both attenuation and delay cannot be extracted out of the collected data for either of the firings in the direct-path. The S_{21} measurements for the White plume exhibit similar behavior to Coutu's firings, where a small gain was seen during the firings, giving plausibility to the theory of multipath beams affecting the collected data.

4.2.2.2 Reflector Measurements

The elliptical multipath reflector described in section 3.2.7 adds another peak to measure data from on each firing, through an adjacent portion of the plume. The collected attenuation and delay data are as plotted in figures 4.31 - 4.42.

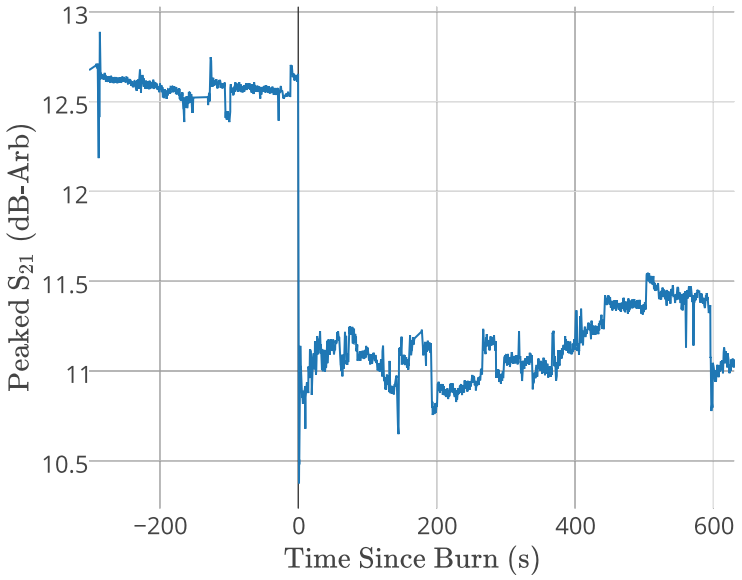

FIGURE 4.31: VMax multipath reflector strength over the burn

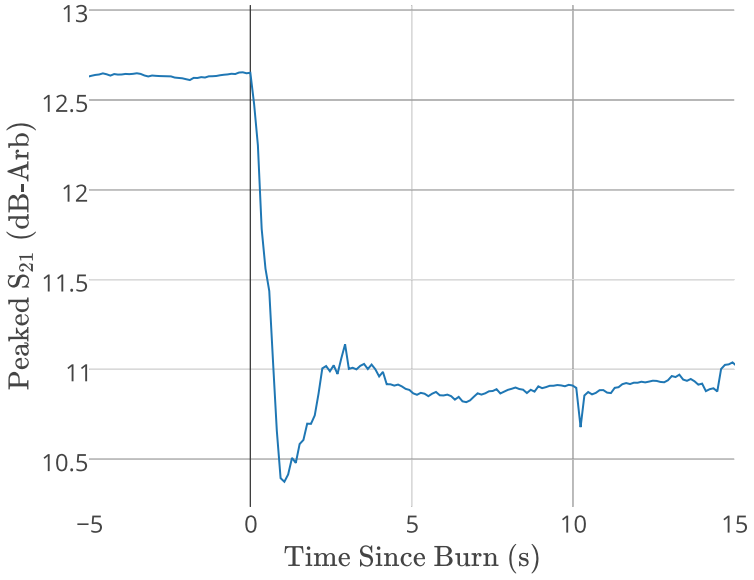

FIGURE 4.32: VMax multipath reflector strength over the burn, detail

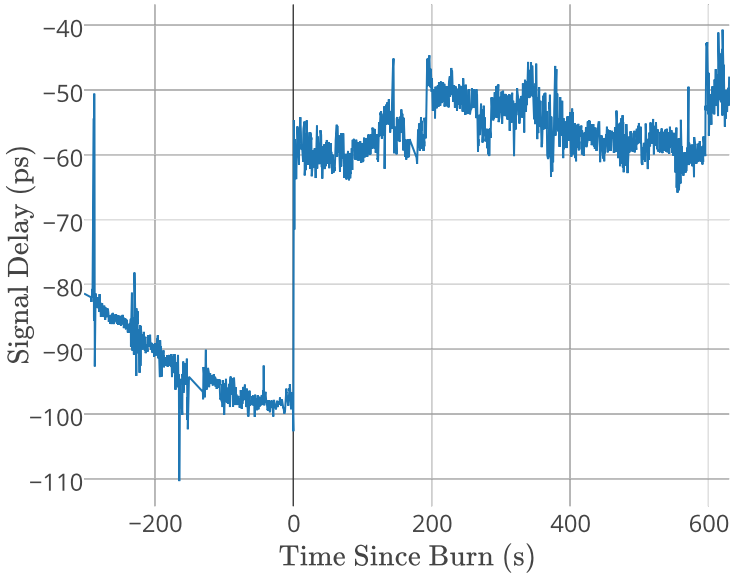

FIGURE 4.33: VMax multipath reflector delay over the burn

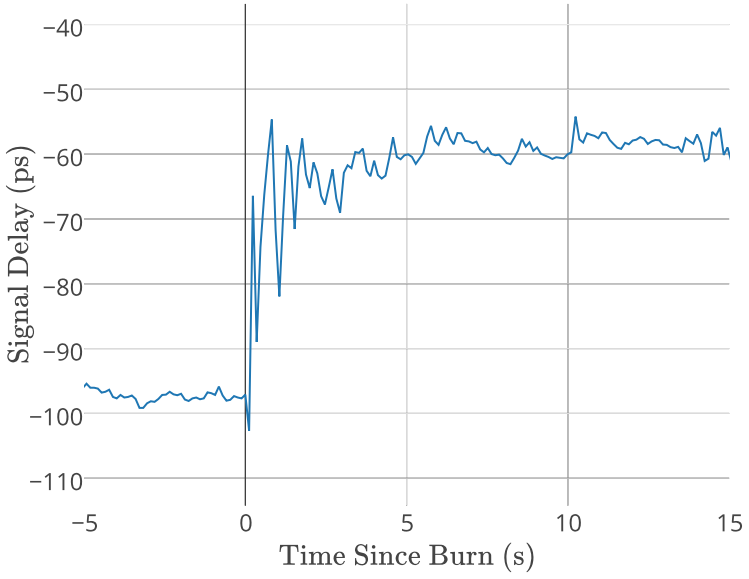

FIGURE 4.34: VMax multipath reflector delay over the burn, detail

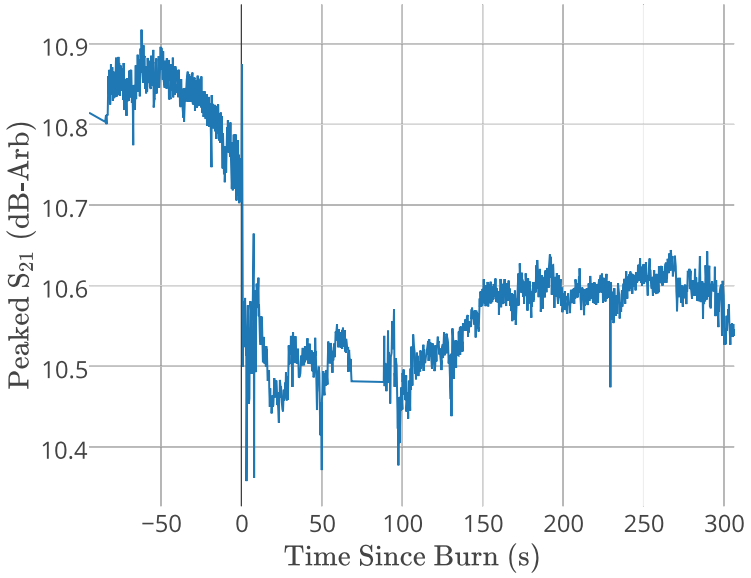

FIGURE 4.35: Longburn multipath reflector strength over the burn

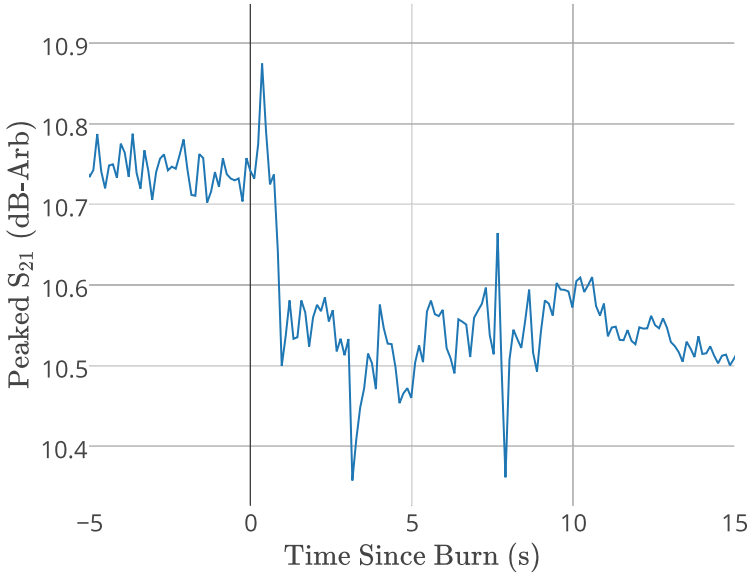

FIGURE 4.36: Longburn multipath reflector strength over the burn, detail

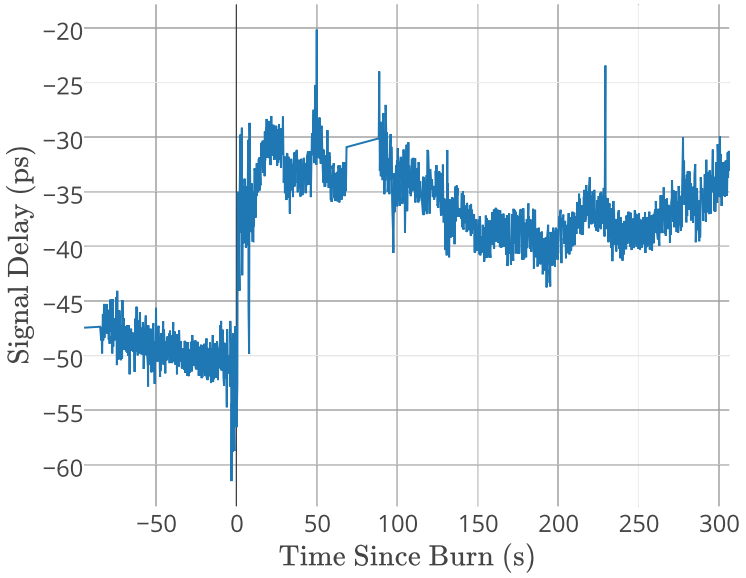

FIGURE 4.37: Longburn multipath reflector delay over the burn

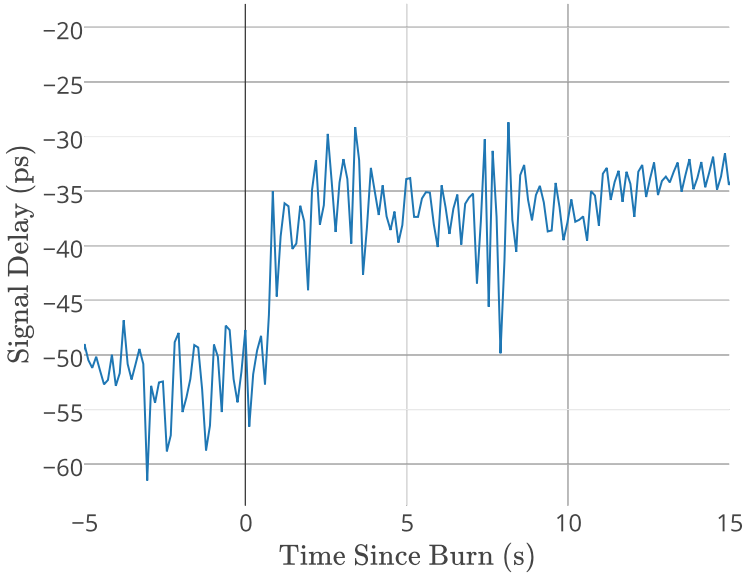

FIGURE 4.38: Longburn multipath reflector delay over the burn, detail

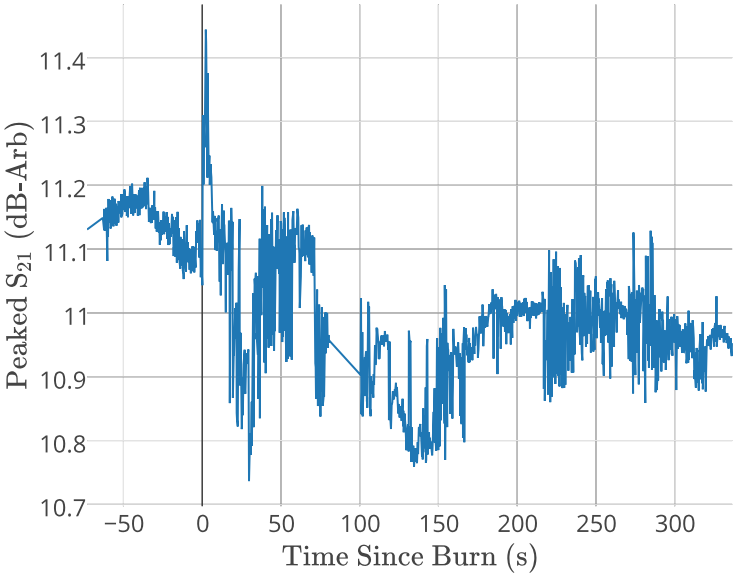

FIGURE 4.39: White multipath reflector strength over the burn

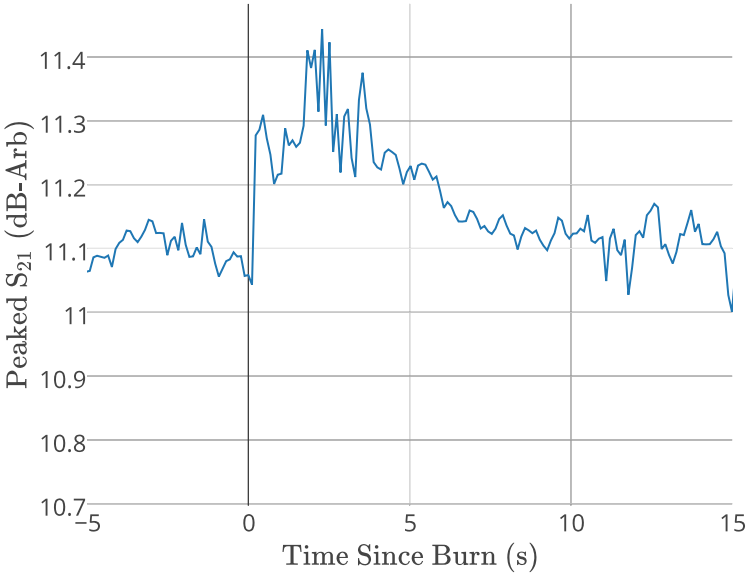

FIGURE 4.40: White multipath reflector strength over the burn, detail

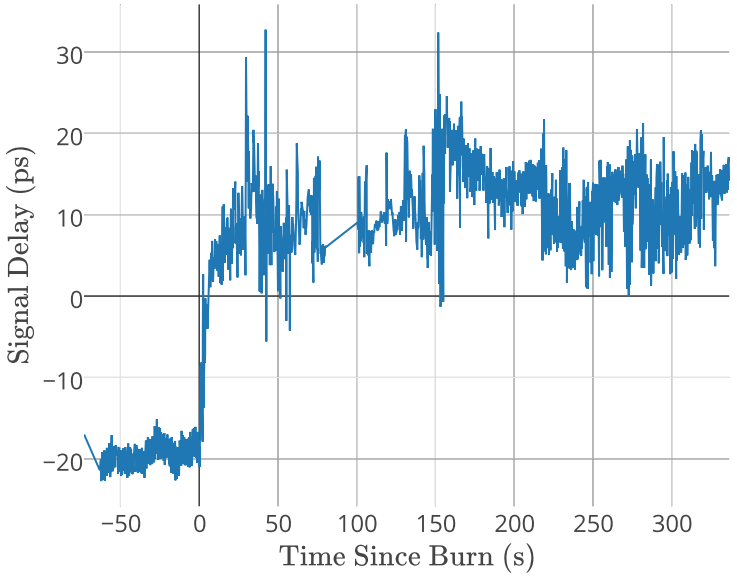

FIGURE 4.41: White multipath reflector delay over the burn

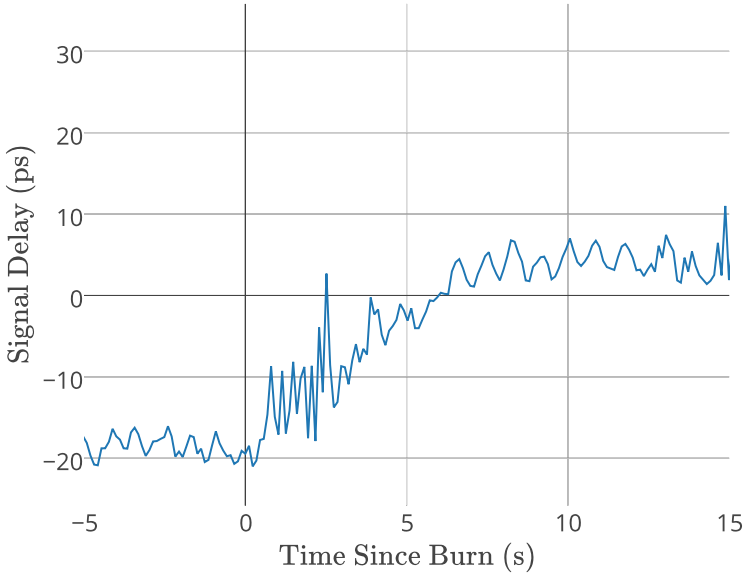

FIGURE 4.42: White multipath reflector delay over the burn, detail

The measurements for the reflector are very similar to the direct-path, in appearance and in terms of noise. The ambiguity in measurements makes a concrete number for attenuation and delay not possible to extract.

4.3 Data Whitening

Because of the high amount of noise encountered in the second set of firings, and because of the lower spatial resolution imposed by the system's low-pass response, a linear equalization factor was applied to the frequency-domain data of the burns to flatten the frequency response of (whiten) the data and increase temporal resolution [30]. Whitening the frequency response of the system reduces the overall impact of multipath on the response of the measurements, but it also changes the response of the plume over the firings.

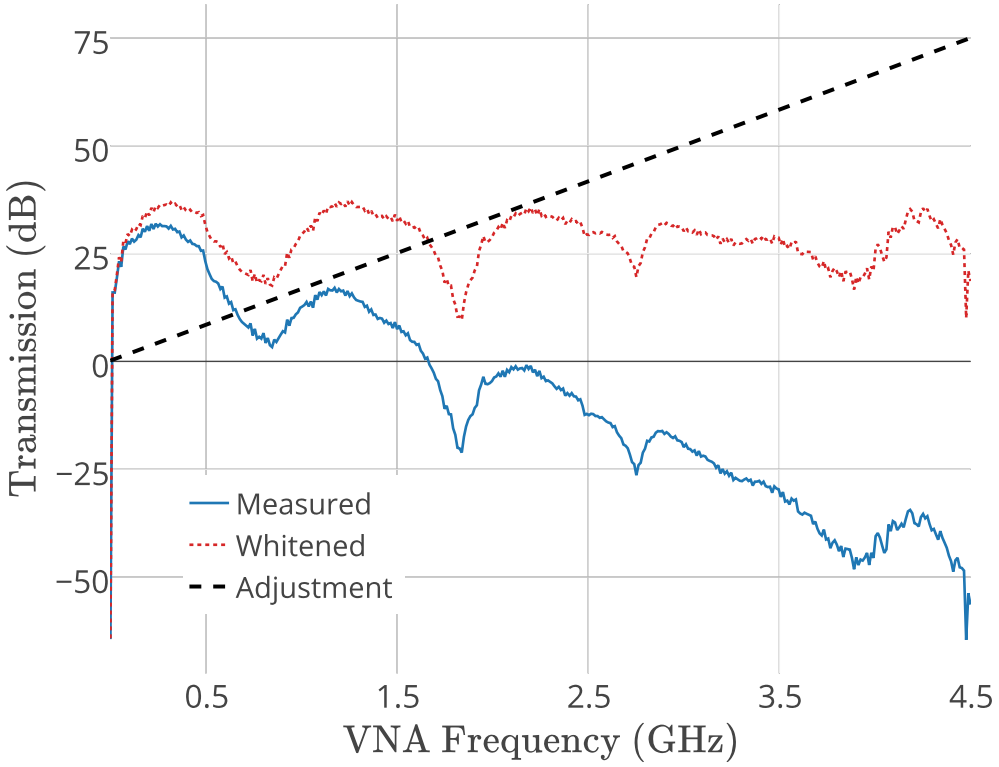

FIGURE 4.43: Whitening applied to frequency-domain data

A 75 dB linear whitening is applied to the VMax, Longburn, and White motors in section 4.3.1 in order to extract a delay and attenuation for each. To analyze the effects of whitening, a 55 dB whitening factor is also applied to the initial Classic and Skidmark burns in section 4.3.2. The whitening data was created by Dr. William C. Barott.

4.3.1 Motor Burns 3, 4, and 5

The VMax, Longburn, and White burns suffered significant noise in measurements as described in section 4.2.2. Whitening makes a correct reading of attenuation and delay

for these firings much easier to extract.

4.3.1.1 Direct-Path Measurements

The whitened data for the direct-path beam is plotted in figures 4.44 - 4.55.

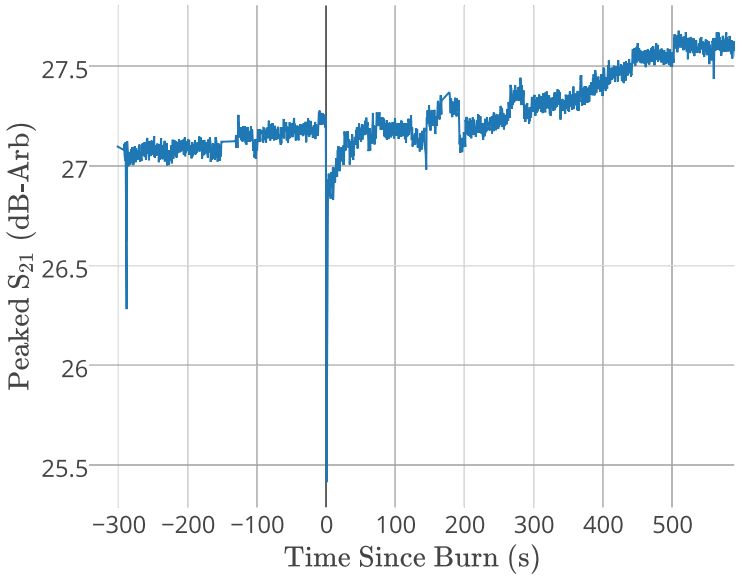

FIGURE 4.44: Whitened VMax direct-path strength over the burn

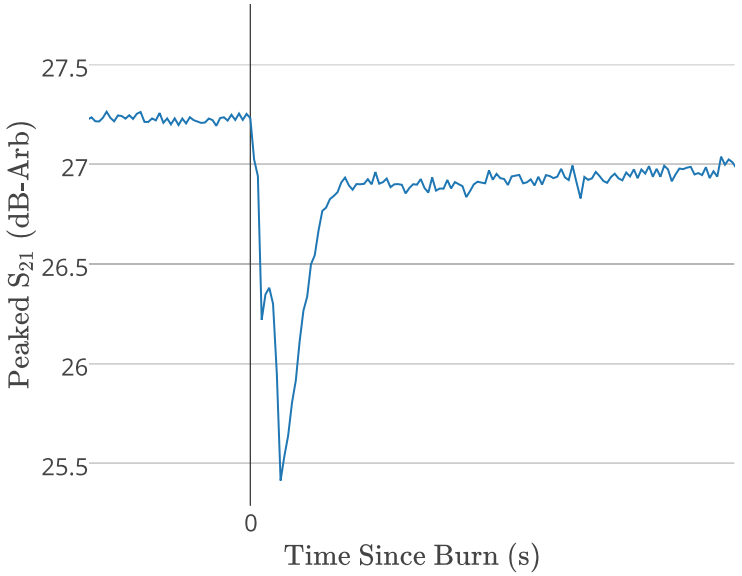

FIGURE 4.45: Whitened VMax direct-path strength over the burn, detail

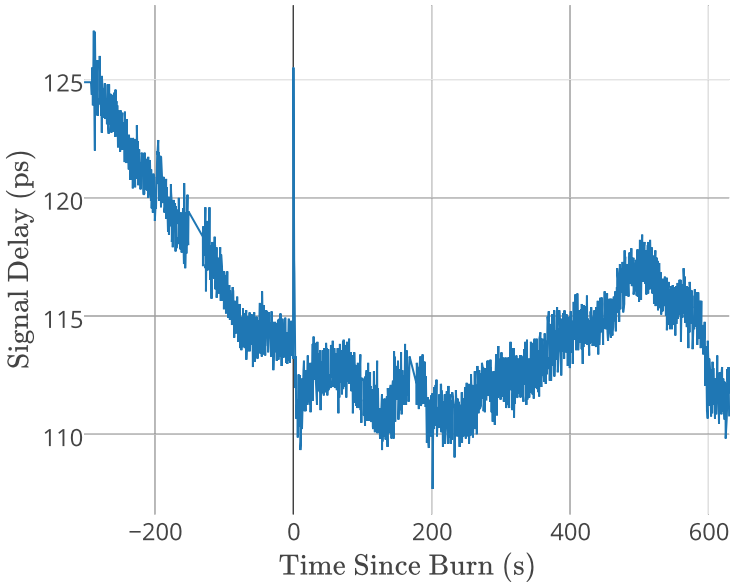

FIGURE 4.46: Whitened VMax direct-path delay over the burn

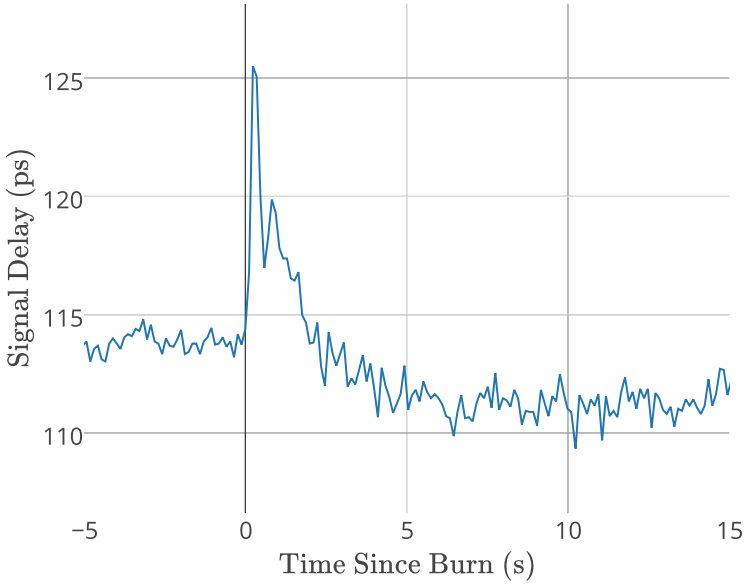

FIGURE 4.47: Whitened VMax direct-path delay over the burn, detail

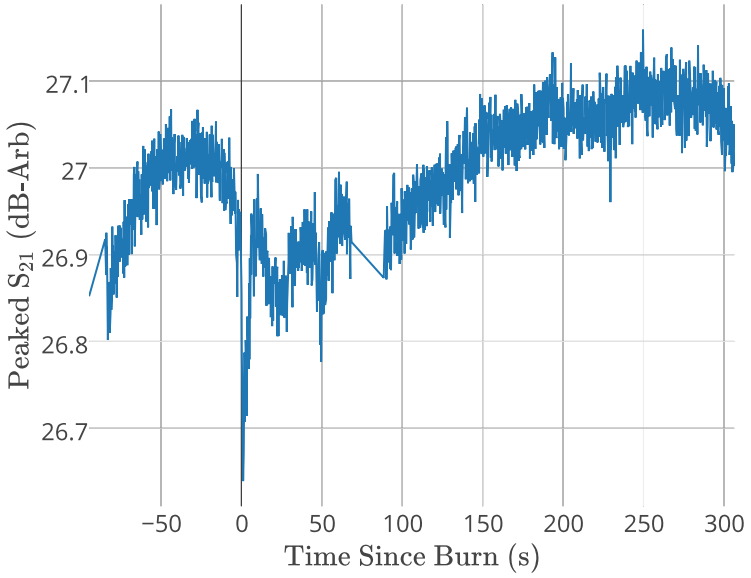

FIGURE 4.48: Whitened Longburn direct-path strength over the burn

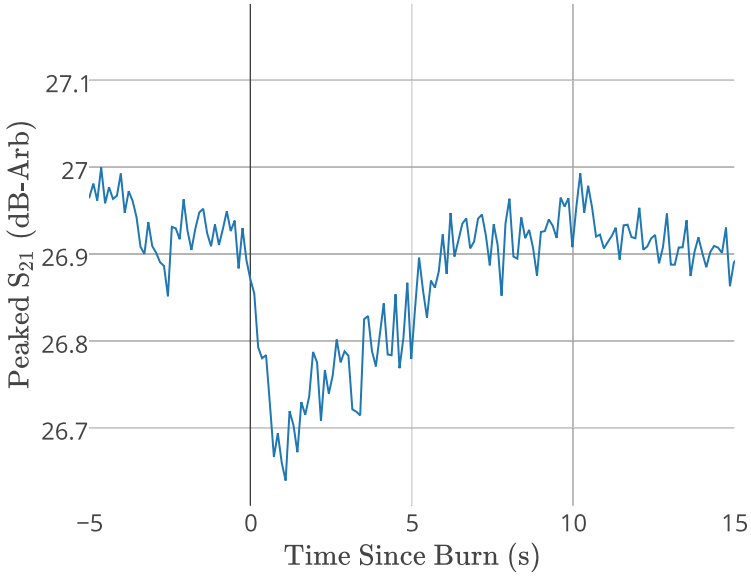

FIGURE 4.49: Whitened Longburn direct-path strength over the burn, detail

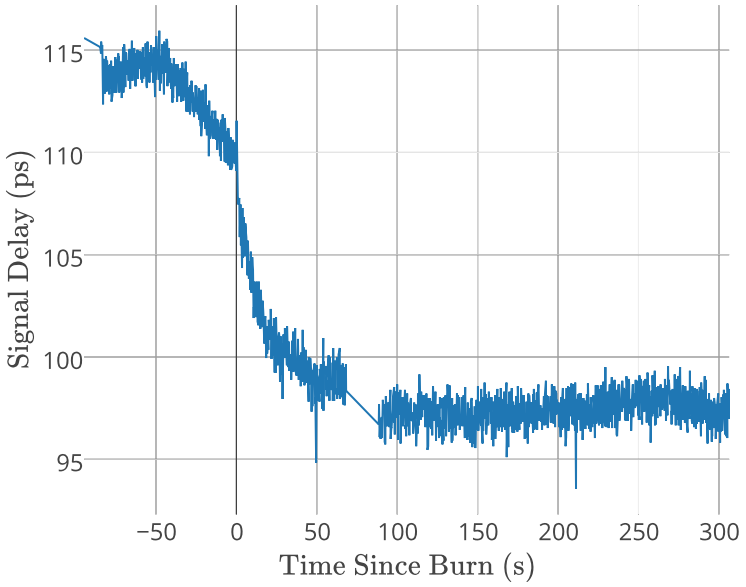

FIGURE 4.50: Whitened Longburn direct-path delay over the burn

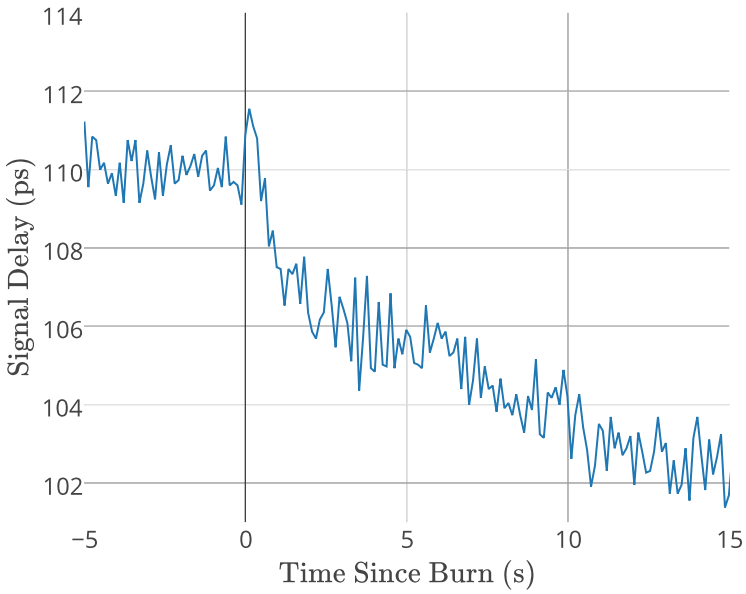

FIGURE 4.51: Whitened Longburn direct-path delay over the burn, detail

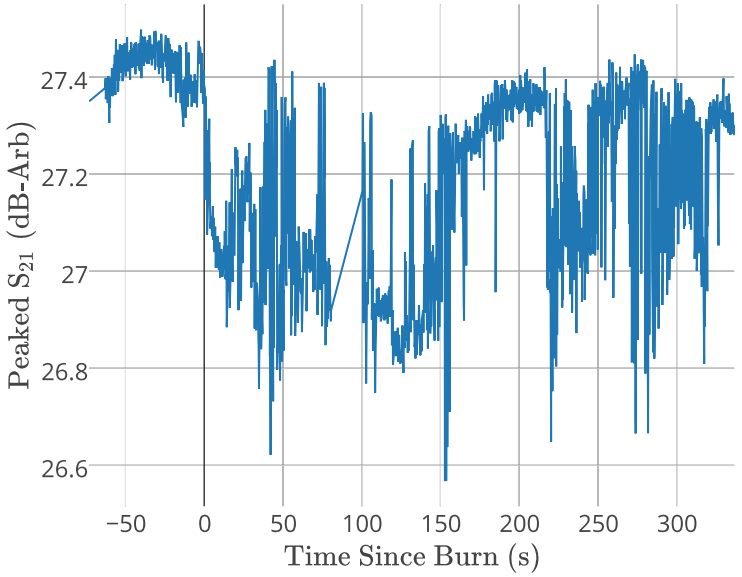

FIGURE 4.52: Whitened White motor direct-path strength over the burn

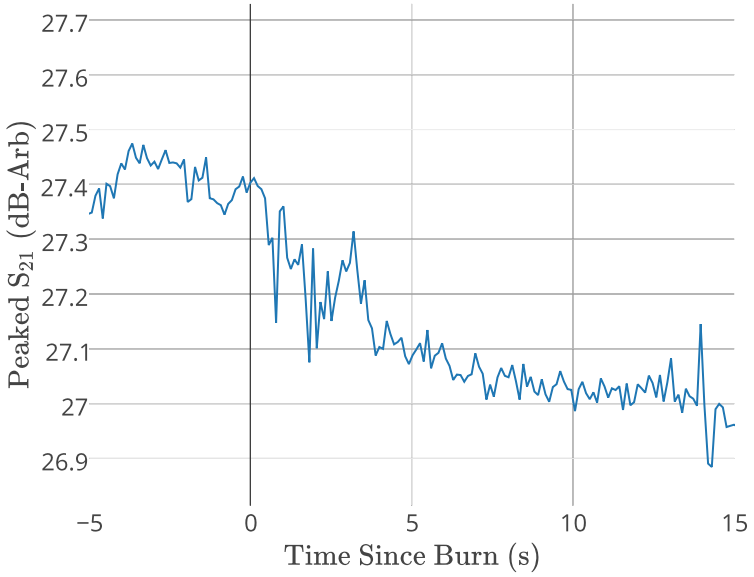

FIGURE 4.53: Whitened White motor direct-path strength over the burn, detail

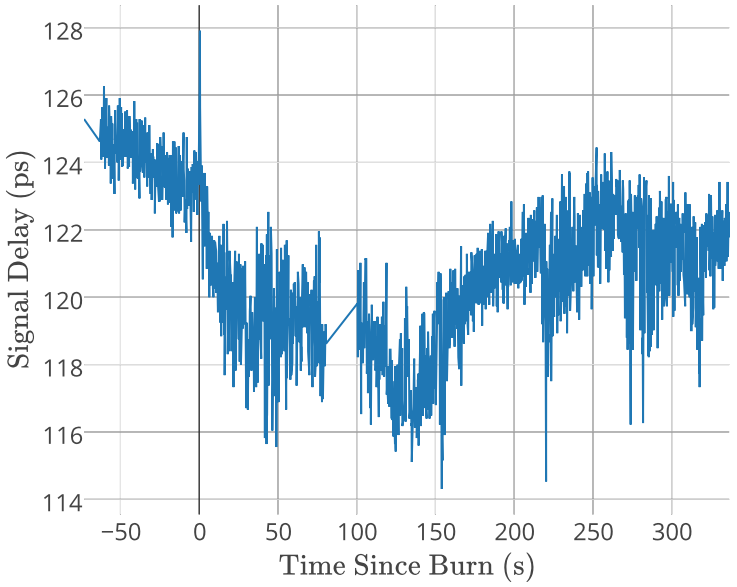

FIGURE 4.54: Whitened White motor direct-path delay over the burn

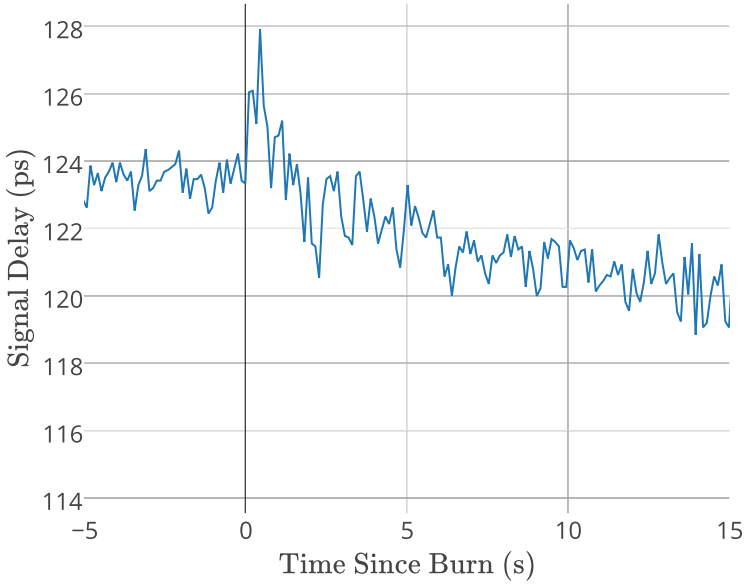

FIGURE 4.55: Whitened White motor direct-path delay over the burn, detail

Extracted measurements for direct-path beam attenuation and delays are as listed in table 4.5.

	Attenuation	Delay
Whitened VMax	1.809 dB	11.65 ps
Whitened Longburn	0.262 dB	1.51 ps
Whitened White	0.295 dB	7.868 ps

TABLE 4.5: Experimental results for whitened VMax, Longburn, and White direct-path beam measurements

Using these results, a set of solution curves created in the same fashion as in section 4.2.1 are created and plotted in figures 4.56 - 4.59.

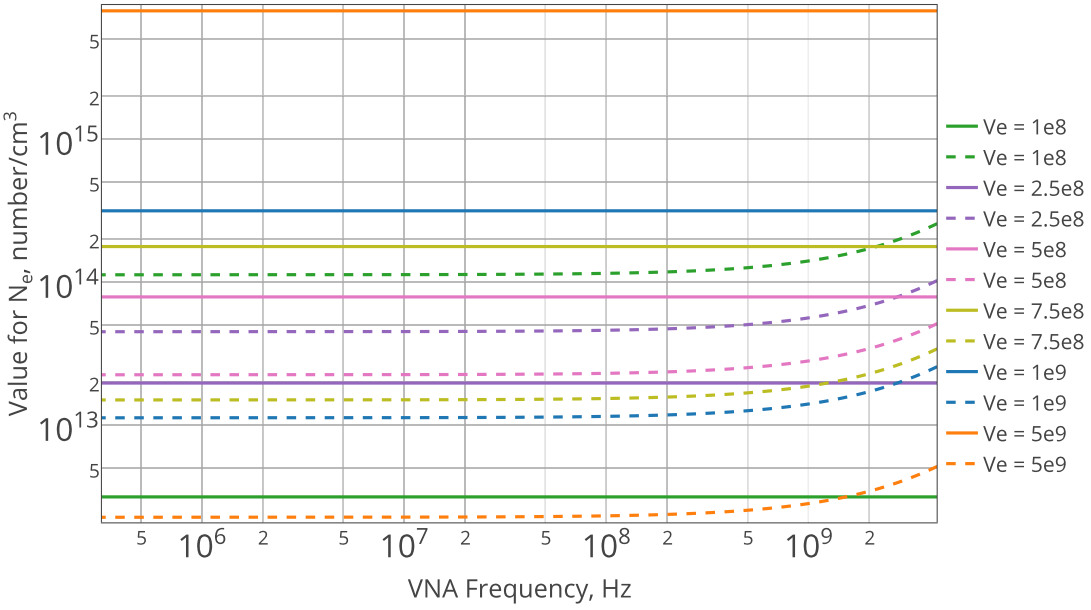

FIGURE 4.56: Solution curves for VMax firing

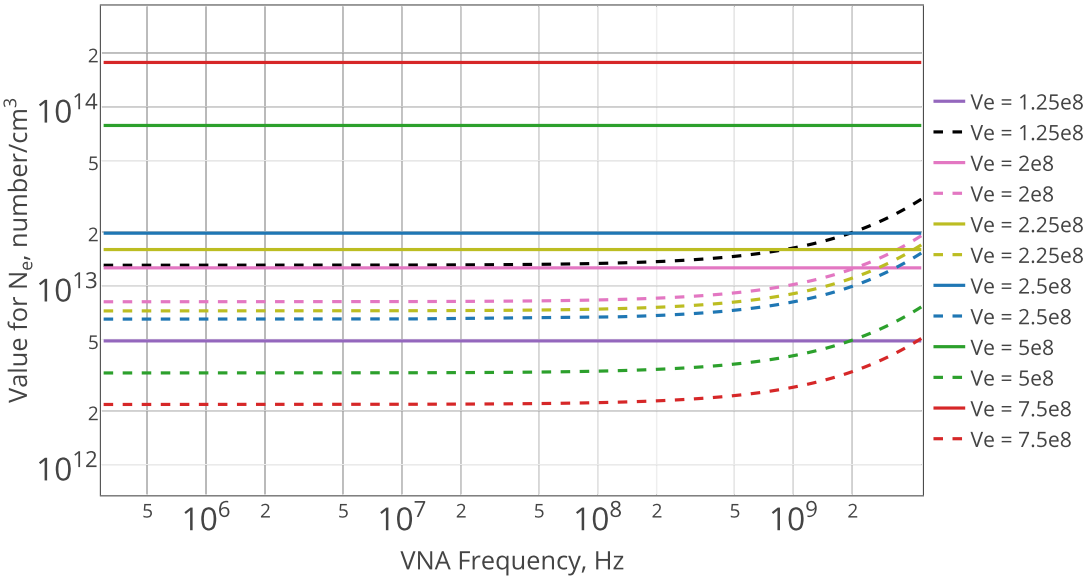

FIGURE 4.57: Solution curves for Longburn firing

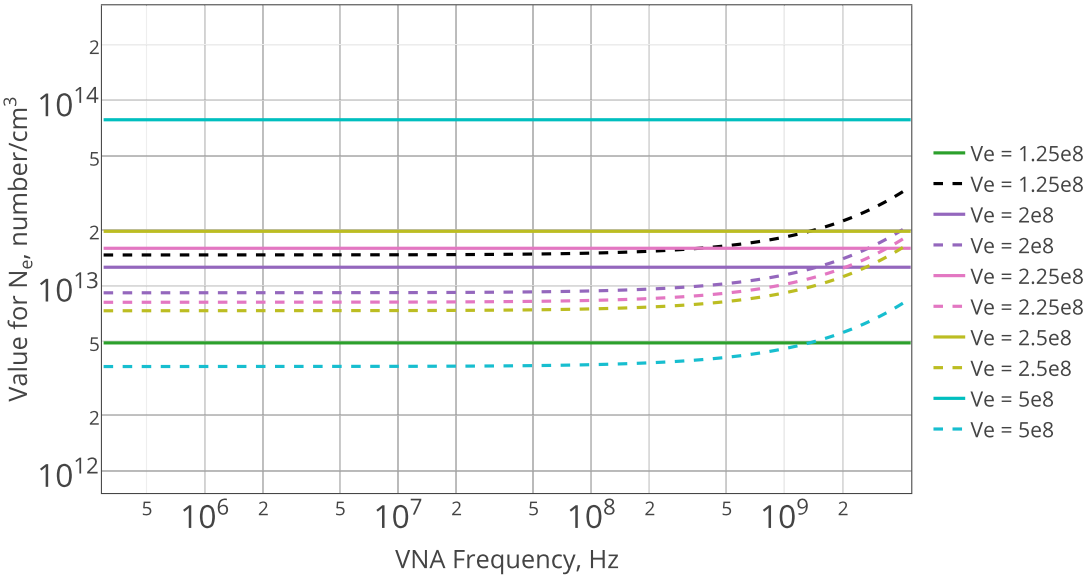

FIGURE 4.58: Solution curves for White firing

Based on the solution curves, the values for N_e and v_e can be extracted as listed in table 4.6.

	N_e	v_e
VMax	2.27×10^{13} - 4.55×10^{13}	3.75×10^8 Hz
Longburn	8.53×10^{12} - 1.25×10^{13}	2×10^8 Hz
White	1.32×10^{13} - 1.59×10^{13}	2.25×10^8 Hz

TABLE 4.6: N_e solutions for whitened VMax, Longburn, and White direct-path measurements

The solutions seem to be correlated with the average thrust of the motors. While all three motors in the last solution set have similar impulses, the VMax has approximately 20 times the average thrust as the Longburn, while the White has about three times as much. This is reflected in the values for N_e and v_e, where the VMax motor appears to have significantly higher values than the Longburn, and the White lies slightly higher than the latter.

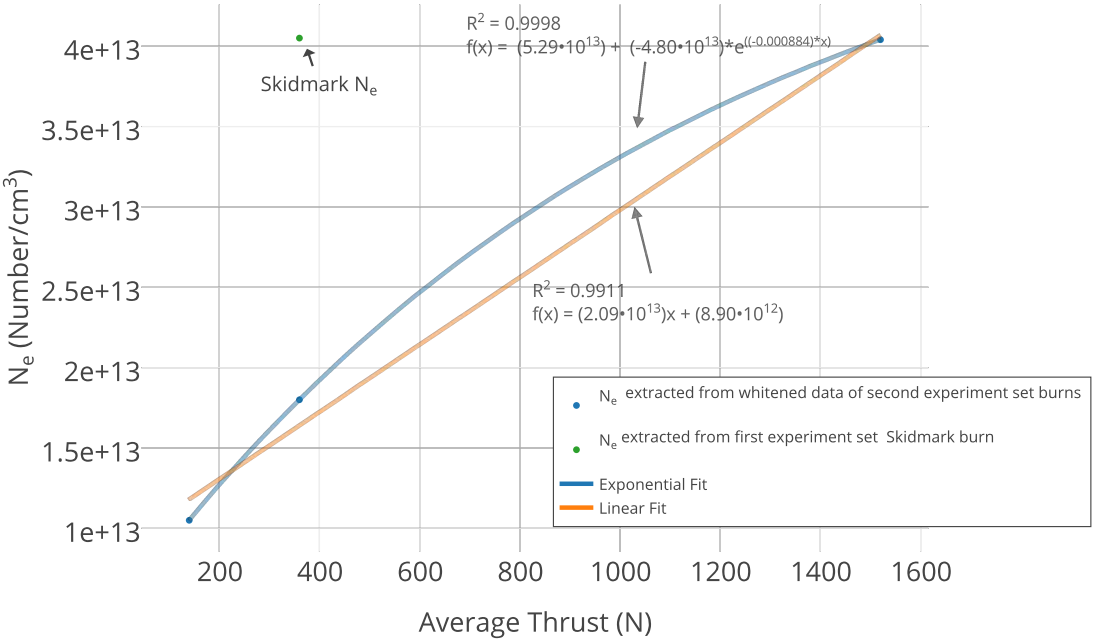

FIGURE 4.59: Plot of motor thrust against the value of N_e extracted from the Whitened data

The solutions are, however, inconsistent with the results from section 4.2.1. The average thrust of the White and Skidmark motors is approximately the same, and so it would be expected that both firings should be similar. Based on the two common average thrusts, it can be observed that the whitening process has approximately halved the measurements for N_e and v_e.

4.3.1.2 Reflector Measurements

The whitened data for the reflected beam is as plotted in figures 4.60 - 4.71.

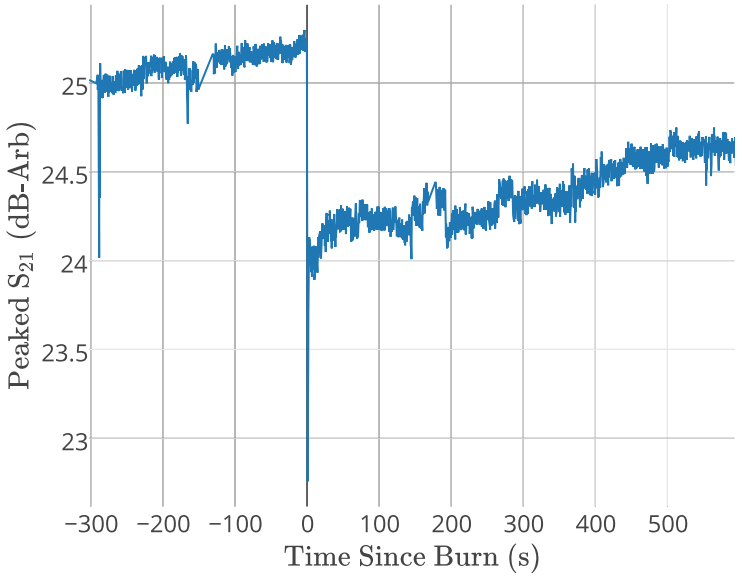

FIGURE 4.60: Whitened VMax multipath reflector strength over the burn

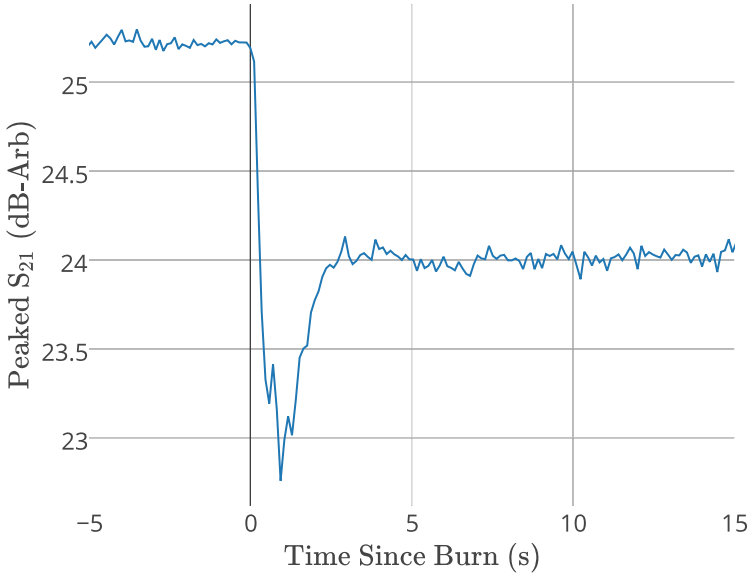

FIGURE 4.61: Whitened VMax multipath reflector strength over the burn, detail

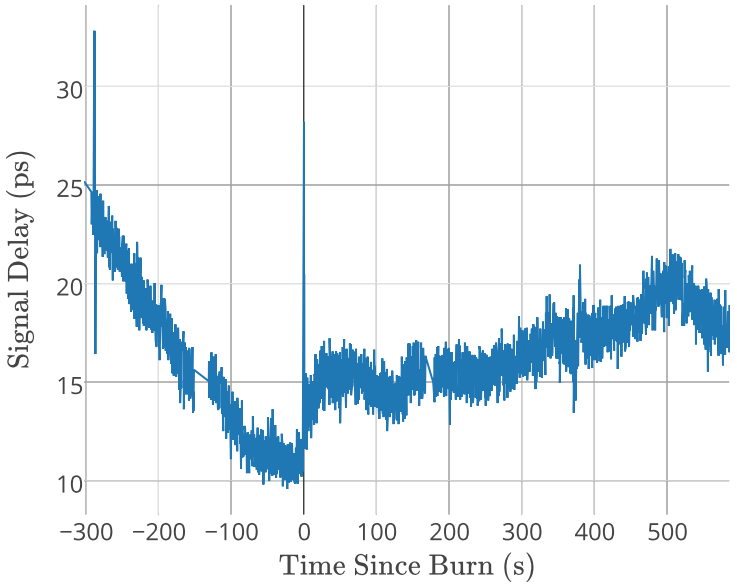

FIGURE 4.62: Whitened VMax multipath reflector delay over the burn

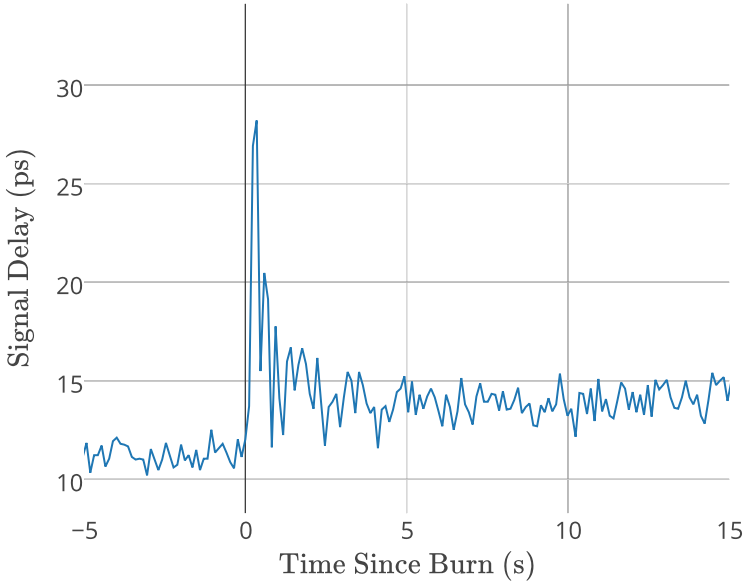

FIGURE 4.63: Whitened VMax multipath reflector delay over the burn, detail

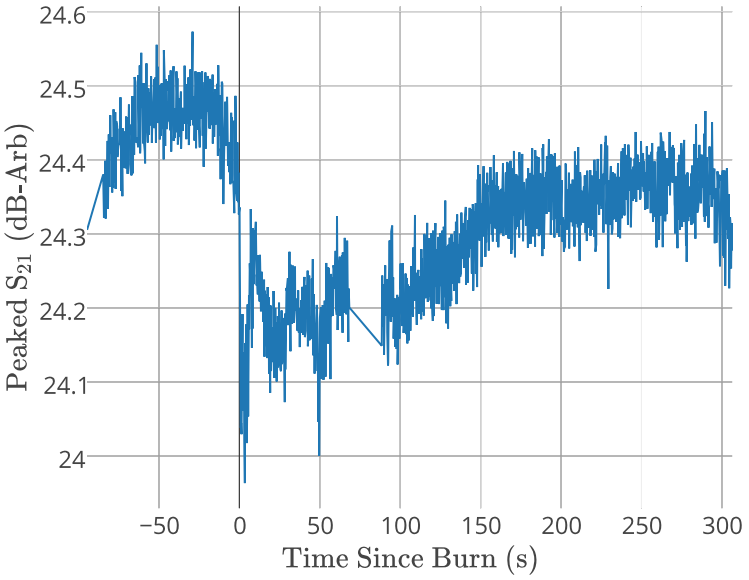

FIGURE 4.64: Whitened Longburn multipath reflector strength over the burn

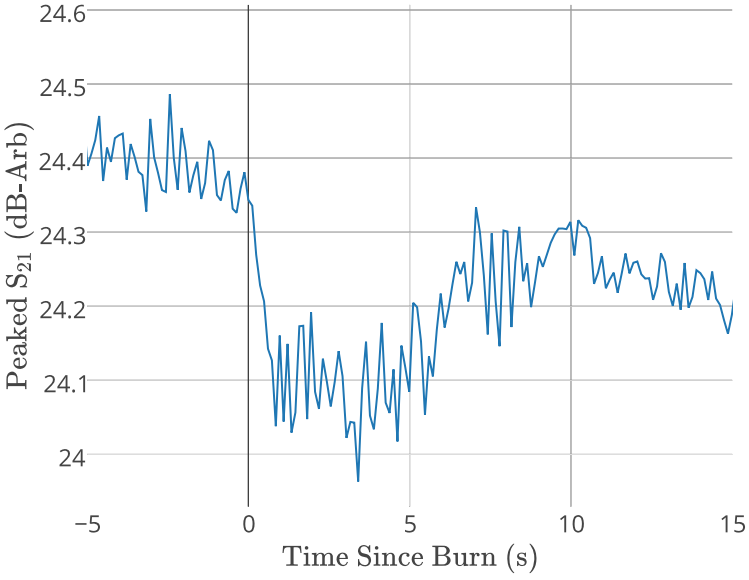

FIGURE 4.65: Whitened Longburn multipath reflector strength over the burn, detail

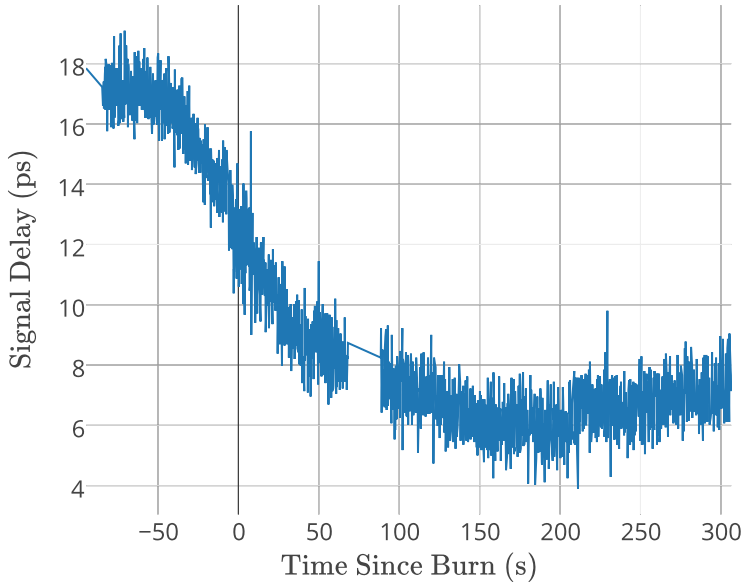

FIGURE 4.66: Whitened Longburn multipath reflector delay over the burn

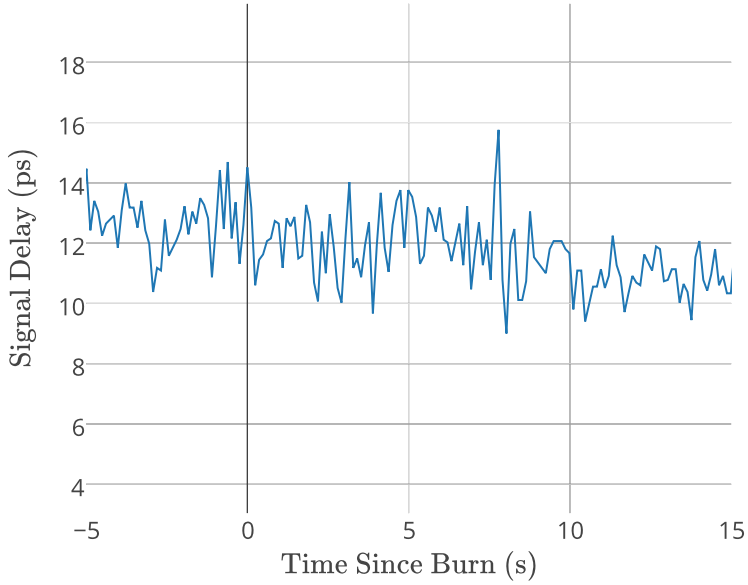

FIGURE 4.67: Whitened Longburn multipath reflector delay over the burn, detail

For the reflected beam, the whitening process does not appear to have removed enough noise from the longburn delay to claim a delay value for that firing.

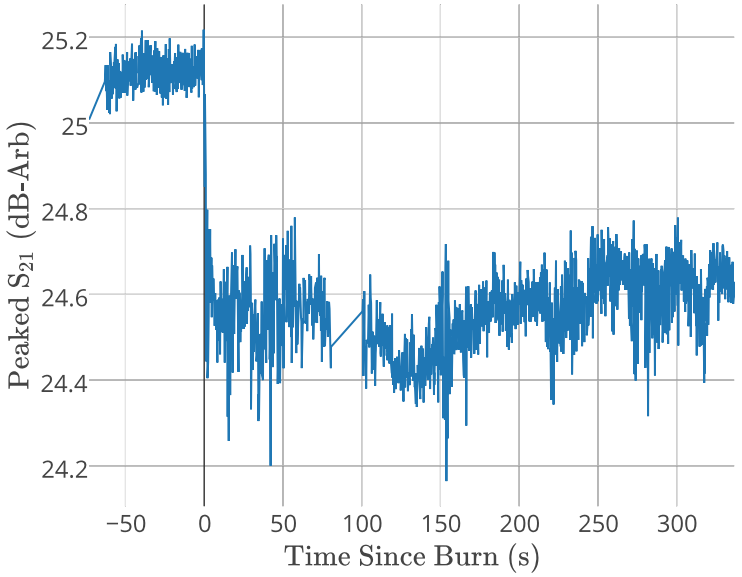

FIGURE 4.68: Whitened White motor multipath reflector strength over the burn

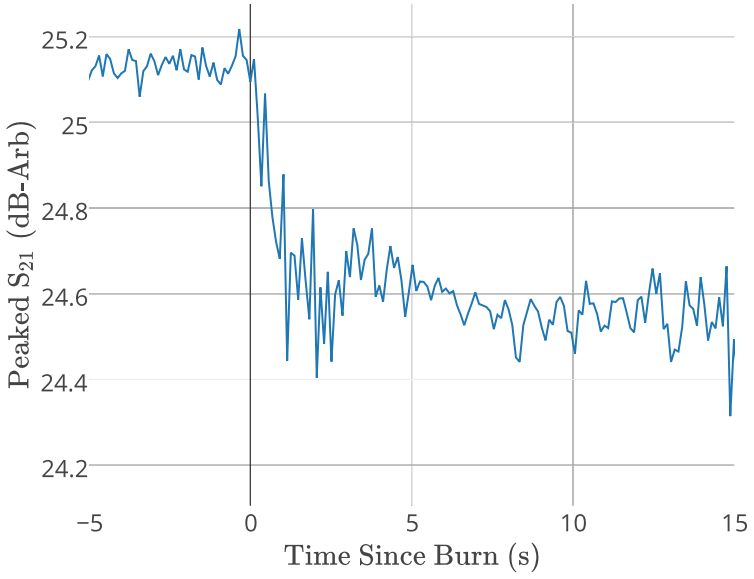

FIGURE 4.69: Whitened White motor multipath reflector strength over the burn, detail

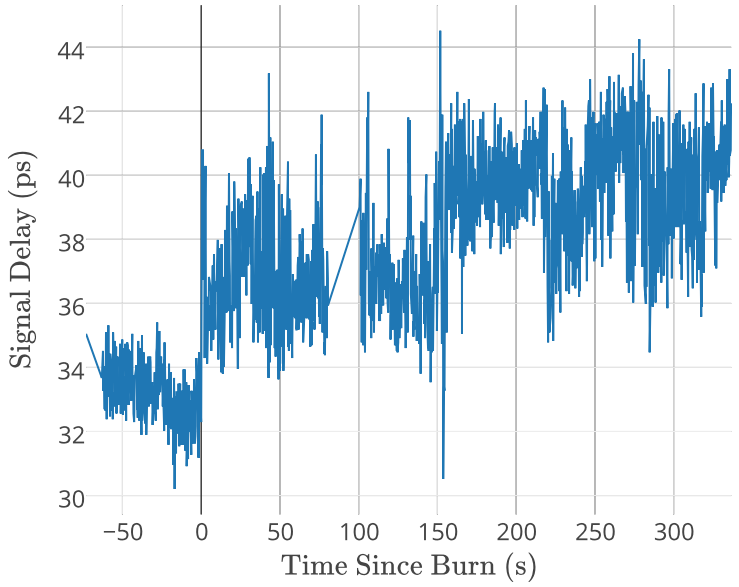

FIGURE 4.70: Whitened White motor multipath reflector delay over the burn

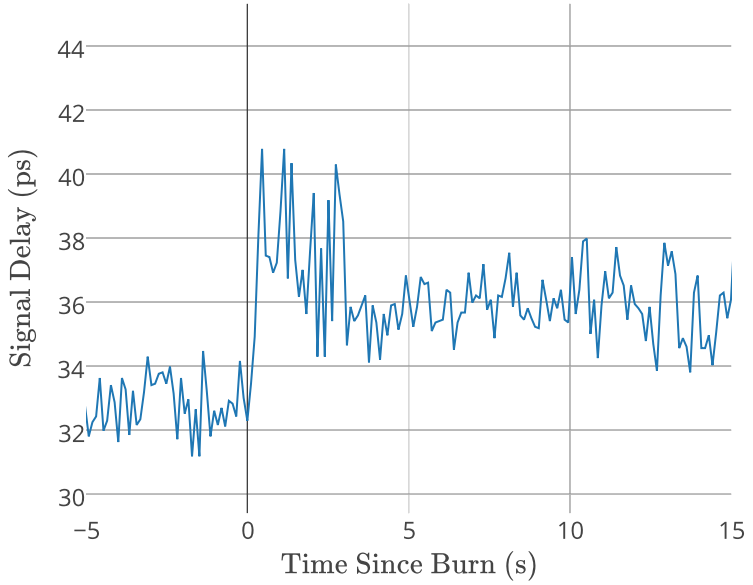

FIGURE 4.71: Whitened White motor multipath reflector delay over the burn, detail

Extracted measurements for direct-path beam attenuation and delays are as listed in table 4.7.

	Attenuation	Delay
Whitened VMax	2.265 dB	16.85 ps
Whitened Longburn	0.261 dB	-
Whitened White	0.688 dB	4.85 ps

TABLE 4.7: Experimental results for Whitened VMax, Longburn, and White reflected beam measurements

With the reflected beam results, another of solution curves are created and plotted in figures 4.82 - 4.83. Since a delay value could not be obtained for the longburn firing, there is no solution possible.

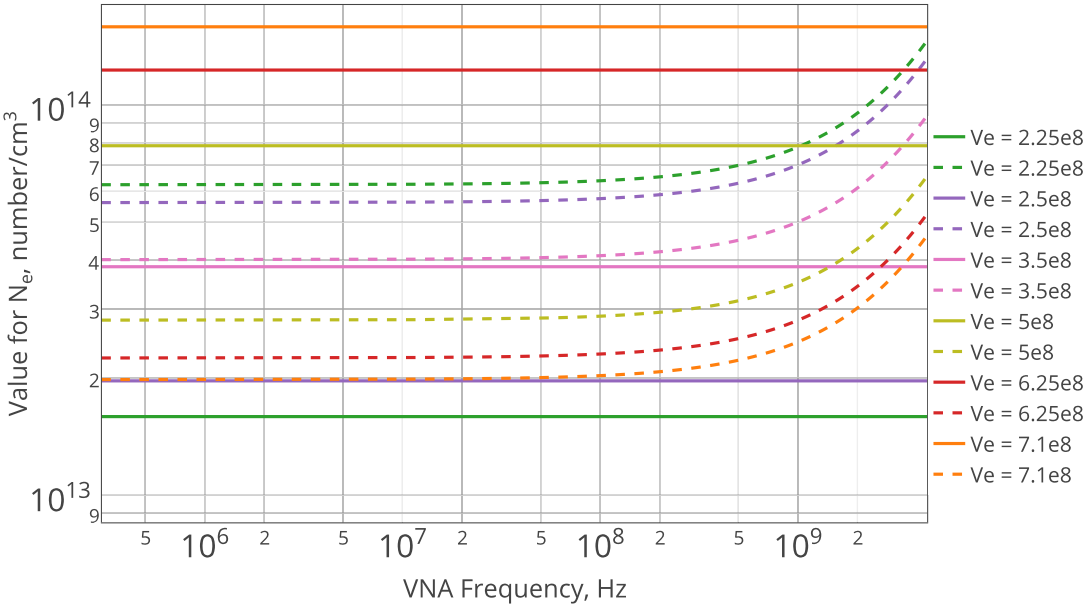

FIGURE 4.72: Solution curves for VMax firing (reflected beam)

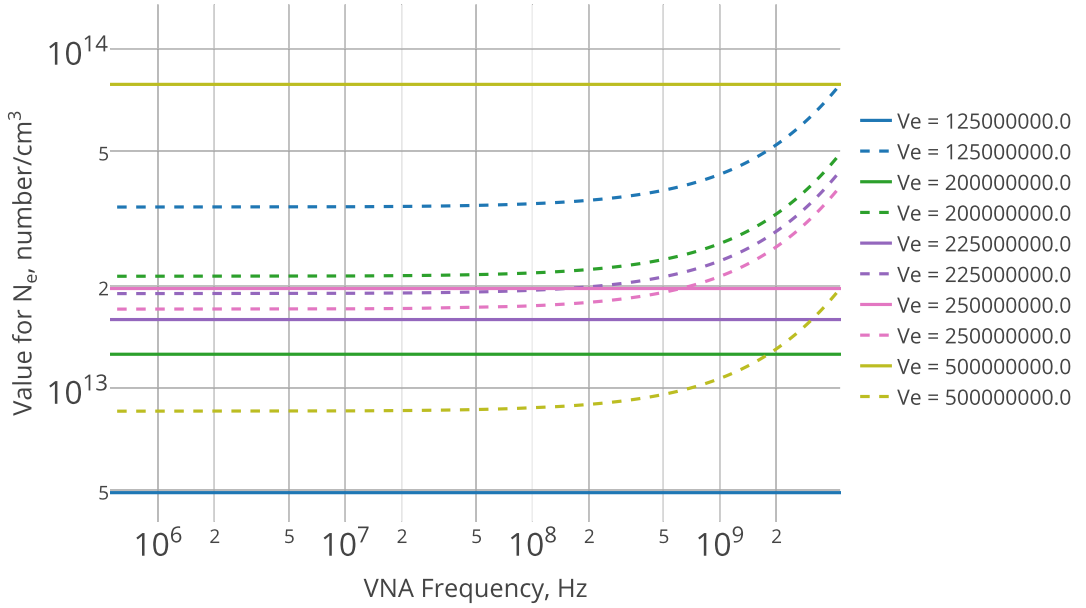

FIGURE 4.73: Solution curves for White firing (reflected beam)

The extracted N_e and v_e values for the reflected beam measurements is as shown on table 4.8

	N_e	v_e
VMax	3.85×10^{13} - 4.21×10^{13}	3.5×10^8 Hz
Longburn	-	-
White	1.71×10^{13} - 1.90×10^{13}	2.3×10^8 Hz

TABLE 4.8: N_e solutions for whitened reflected-beam measurements

For the VMax and White burns, there is an increase in N_e in the reflected beam, implying that the region of highest density was further back on the plume from were the antennas were placed.

4.3.2 Motor Burns 1 and 2

In order to compare the effects of whitening with a known set of data, the previous Skidmark and Classic burns were also whitened in frequency-domain. The resulting new plots are as shown in figures 4.74 - 4.81.

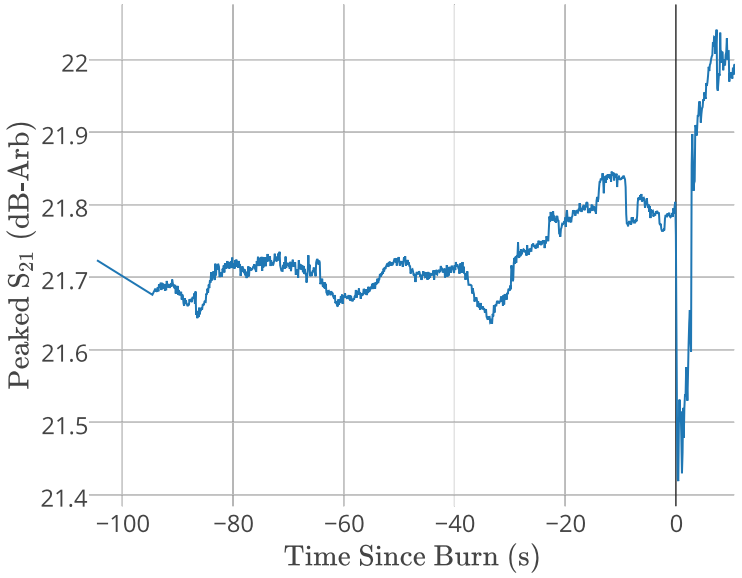

FIGURE 4.74: Whitened Skidmark direct-path strength over the burn

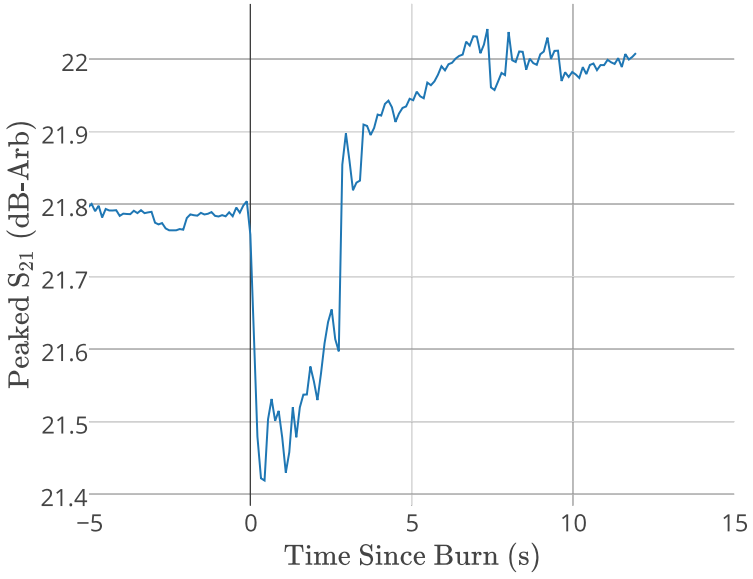

FIGURE 4.75: Whitened Skidmark direct-path strength over the burn, detail

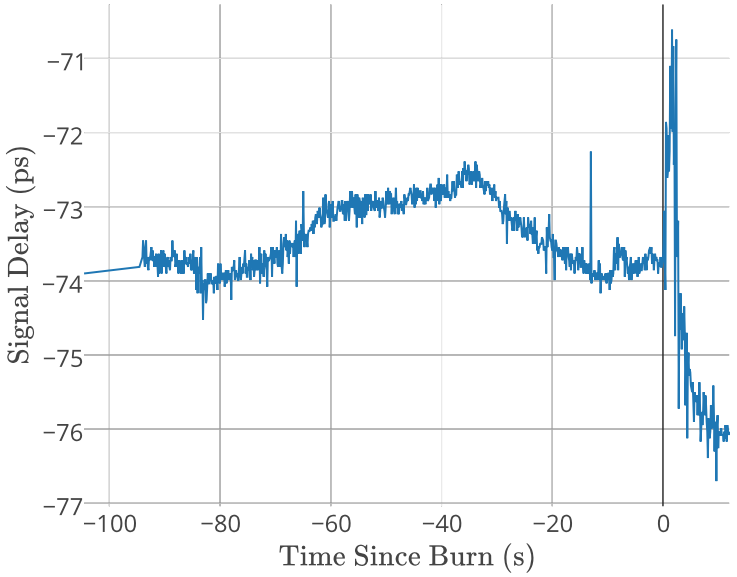

FIGURE 4.76: Whitened Skidmark direct-path delay over the burn

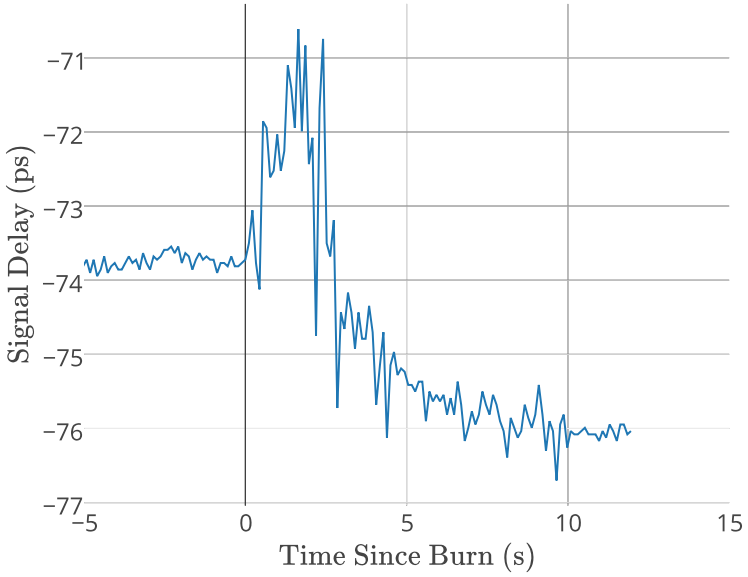

FIGURE 4.77: Whitened Skidmark direct-path delay over the burn, detail

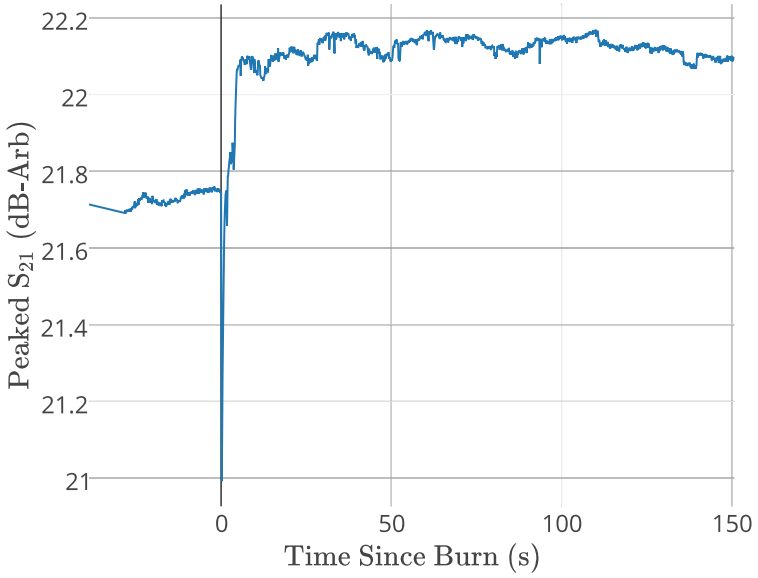

FIGURE 4.78: Whitened Classic direct-path strength over the burn

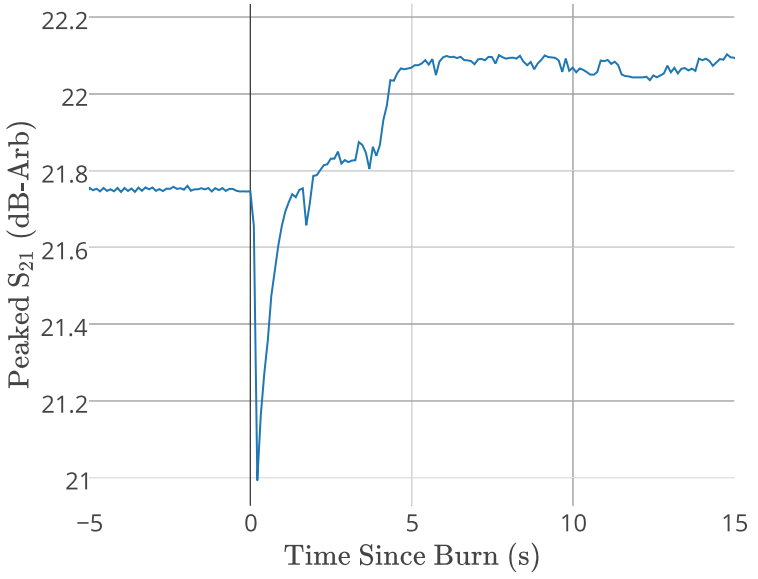

FIGURE 4.79: Whitened Classic direct-path strength over the burn, detail

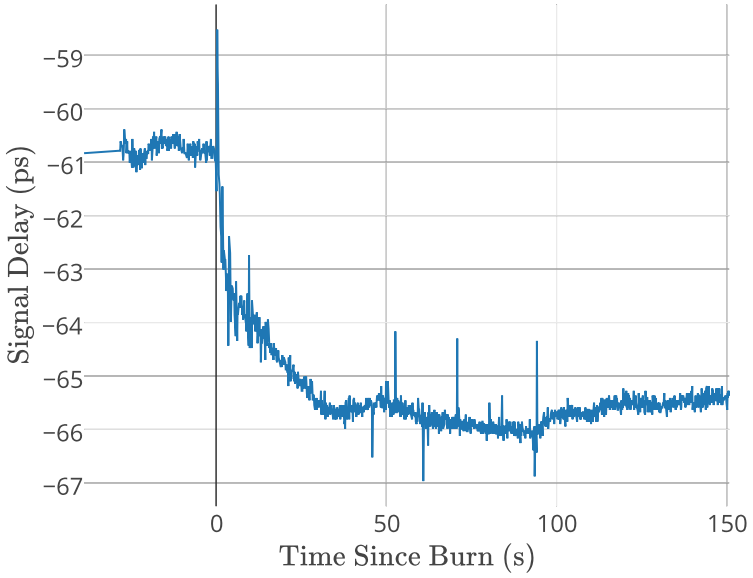

FIGURE 4.80: Whitened Classic direct-path delay over the burn

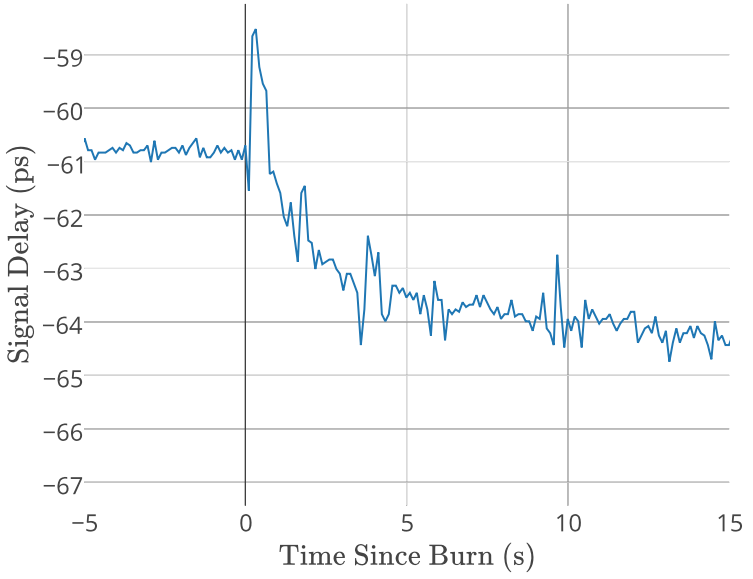

FIGURE 4.81: Whitened Classic direct-path delay over the burn, detail

Based on the whitened plots, the new attenuation and delay values for the Classic and Skidmark burns are as listed in table 4.9.

	Attenuation	Delay
Whitened Skidmark	0.36 dB	3.07 ps
Whitened Classic	0.76 dB	2.22 ps

TABLE 4.9: Experimental results for whitened Classic and Skidmark measurements

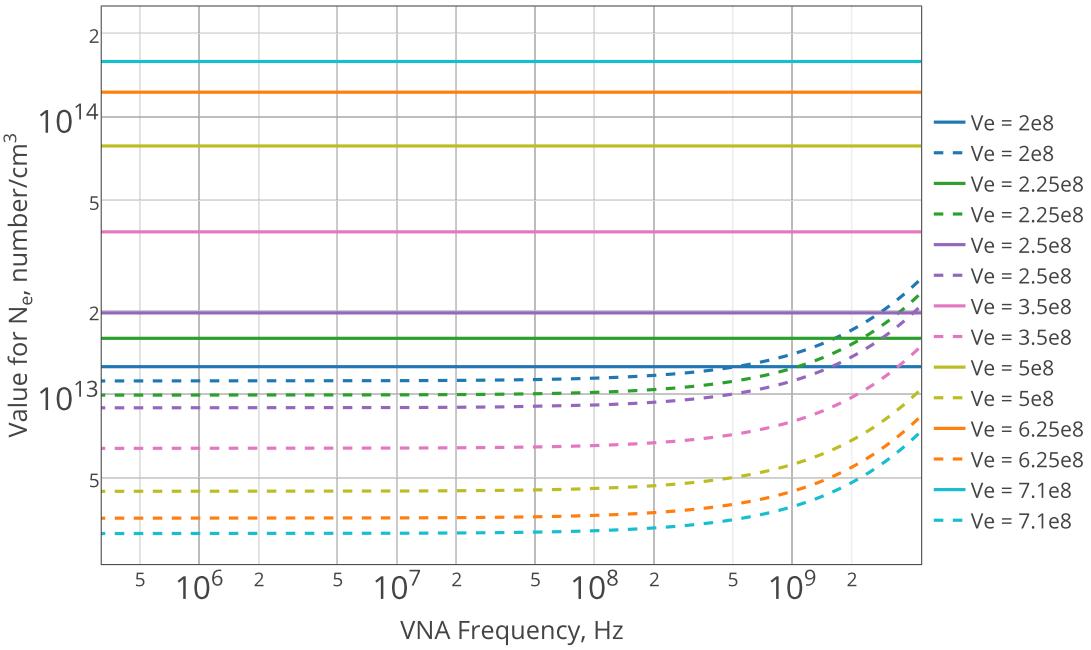

FIGURE 4.82: Solution curves for Skidmark firing (whitened)

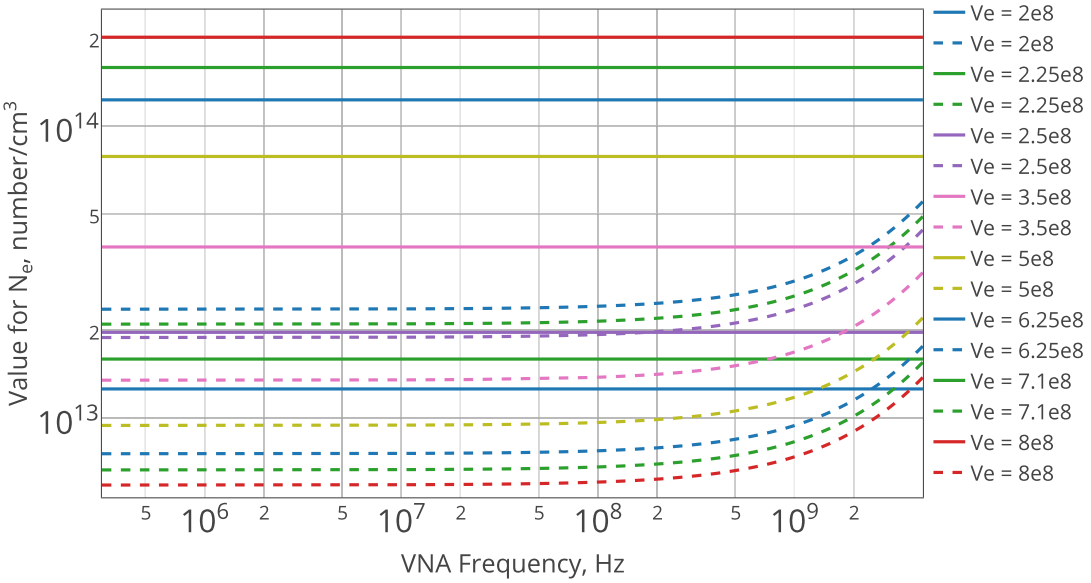

FIGURE 4.83: Solution curves for Classic firing (whitened)

The new solutions for the Whitened Skidmark and Classic values are as listed on table 4.10

	N_e	v_e
Whitened Skidmark	1.11×10^{13} - 1.25×10^{13}	2×10^{8}
Whitened Classic	1.80×10^{13} - 1.96×10^{13}	2.5×10^{8}

TABLE 4.10: N_e solutions for whitened Skidmark and Classic data

The new solutions are consistent with the other whitened data in that they appear to be approximately halved from the non-whitened prediction. The new Skidmark values show a 110% difference, while the Classic shows a 120% difference in values.

Chapter 5

Research Conclusion

Given the commonality of linear equalization as a radar range-resolution sharpening technique, it is likely that the whitened values are more correct than the non-whitened. However, it would be beneficial to repeat the experiments multiple times without the reflector to show the effects of whitening without an increased multipath environment.

The solutions for N_e and v_e found in this study are similar to measured values in previous studies [11, 14, 17]. It is therefore plausible that N_e and v_e can be estimated accurately by finding the phase velocity u_p of the plume through wide bandwidths and ranging. However, additional solutions using different methods based on the delay and attenuation of a radio wave passing through the plume would help further verify the results.

Given the patterns of non-restoring data, even with the thin horizontal beamwidth of the Vivaldi arrays, it is possible that focusing was not the sole cause of the effects in Coutu's thesis, although focusing effects could be seen at the measured plasma parameters in simulations. Temperature seems to affect the overall response of the system, and how it changes after the rocket fire isn't well known. However, some focusing could be observed in the FDTD model after experimental values were used in the model.

The analysis suggests a much lower value for v_e than in the CFD models. This is consistent with Van der Beek's paper's conclusions [9] and is in the same order of magnitude as Kinefuchi's model [11].

Chapter 6

Topics for Further Research

The effect of air and system temperatures should be a focus of future studies of similar scales. A more sophisticated set of instruments could theoretically correlate the increase in gain with an air temperature between the antennas as opposed to adjacent to them.

The addition of other peaks by intentionally introducing multipath has appeared to make the data more noisy, but could be filtered to produce more precise results. This may be an alternative to moving platforms [14] in the future to test multiple parts of the plume, without requiring more antennas and RF equipment. Using ranging presents multiple challenges in analyzing data and adding multiple beams seems to compound the challenges; therefore, whatever properties that can be exploited from radar techniques should be utilized. It could prove helpful to send pseudo-random digital data through the plume in order to utilize correlation and eye-diagram techniques for optimizing filters and reducing Inter-Symbol Interference. Improving the RF section of the apparatus to support the full range of the Wilkinson transformers and antennas would increase the precision of the apparatus.

Finding more solutions for N_e and v_e as related to phase velocity and attenuation seem like the most critical factor in improving the quality of the experimental model. Smoot's model [17] is known to be a very rough estimate for attenuation, and the method for using the index of refraction in this study has, to the author's knowledge, not been previously used.

Appendix A

Bill of Materials

This page intentionally left blank.
Refer to next page for bill of materials.

	Description	Manufacturer	Model Number	Quantity	Part of Coutu's Thesis?	Replacement Cost	Cost to Thesis
RF Equipment	Vivaldi Antenna Arrays	-	-	2		-	-
	SMA to SMA PE-P195 Coax, 600 in.	Pasternack	PE3138	2	✓	$64.47	-
	SMA to SMA RG405 Coax, 24 in	Pasternack	PE3831-24	8	✓	$88.64	-
	Super Ultra Wideband Amplifier, 0.1-18 GHz	Mini-Circuits	ZVA-183W+	1	✓	$ 1,395.00	-
	Connectorized Amplifier	Mini-Circuits	ZX60-8008E+	8	✓	$399.60	-
	Mixers	Mini-Circuits	ZX05-24MH+	2		$109.90	$109.90
	Low-Pass Filter	Mini-Circuits	VLF-7200+	1		$24.95	$24.95
	High-Pass Filters	Mini-Circuits	VHF-8400+	2		$43.90	$43.90
	Power Divider	Mini-Circuits	ZX10-2-126-S+	1		$39.95	$39.95
	Local Oscillator	Polarad	1108E	1		-	-
	Programmable DC Power Supplies	Tektronix	PS2510G	3		$699.00	-
	Vector Network Analyzer	Agilent	E5071B	1	✓	$50,000.00	-
Structure	Slotted-Aluminum Frames	80/20 Inc.	1515		✓	-	-
	Steel Test Stand	-	-	1	✓	-	-
	Elliptical Reflector	-	-	1		-	$12.95
Instrumentation	Laptop with GNU/Linux OS	Asus	EEE1000HD	1		$300	-
	Data-collection microcontroller	Arduino	Uno	2		$30	-
	3-Axis Accelerometer	Sparkfun	MMA8452	1		$9.95	$9.95
	Ambient temperature and pressure sensor	Sparkfun	MPL115A1	1		$12.95	$12.95
	Infrared Proximity Sensor	SHARP	GP2Y0A21YK	1		$13.95	$13.95
	Thermocouple amplifier	Adafruit	269	4		$59.80	$59.80
	Type-K glass braid thermocouple	Adafruit	270	4		$39.80	$39.80
Rocket Motors	Cesaroni Pro-54 3-Grain Casing	Cesaroni	P54-3G	1	✓	$69.39	-
	Cesaroni Pro-54 Delay/Eject Closure Adapter	Aero Pack	MC54	1	✓	$14.00	-
	Cesaroni J295 Classic Reload Kit	Cesaroni	1195J295-16A	1		$91.50	$91.50
	Cesaroni J360 Skidmark Reload Kit	Cesaroni	1016J360-16A	1		$92.95	$92.95
	Cesaroni K360 White Reload Kit	Cesaroni	1281K360-13A	1		$99.46	$99.46
	Cesaroni J140 White Longburn Classic Reload Kit	Cesaroni	1266J760-19A	1		$91.50	$91.50
	Cesaroni J1520 VMax Reload Kit	Cesaroni	1093J1520-17A	1			
					Replacement Total (excl. VNA)	$3790.66	
					Cost Total		$743.51

Appendix B

Source Code

B.1 Data collection scripts

The data collection scripts are responsible for communicating with the VNA to store information, and ensuring that live data is being saved. A tcl expect script spawns a telnet session, and specifying a folder on the VNA's D drive and its network address will allow telnet to trigger the machine and save files to that folder. A Python script can display time or frequency information for those stored files, assuming the VNA's folder is mounted locally on the filesystem.

B.1.1 Expect: vna-trig-save-local

```
1
2  #!/usr/bin/expect
3  #
4  # vna-trig-save-local
5  #
6  # This script communicates with the VNA to save S2P files to its
7  # local memory.
8  #
9  # folders are specified on the VNA's D drive.
10 # its proper usage should be:
11 #
12 # ./vna-trig-save-local IPADDRESS LOCALFOLDER
13 #
14 # Needless to say, you will need to install expect script
15 # support to be able to run this script.
16
17
18
19 set host    [lindex $argv 0]
20 set folder  [lindex $argv 1]
21
22 set prompt "SCPI>"
```

```
23
24 #open a telnet session to talk with the VNA
25 spawn telnet $host
26 expect "'^]'."
27 send "\r\n"
28 sleep 3
29
30 send "\r"
31
32 #wait for the VNA to respond
33 expect "$prompt"
34 send ":TRIG:SCOP ACT\r"
35 sleep 1
36 expect "$prompt"
37 send ":TRIG:SOUR BUS\r"
38 sleep 1
39 expect "$prompt"
40 send ":DISP:ENAB OFF\r"
41 sleep 1
42
43 while {1 > 0} {
44
45 #save each file with the current unix time in microseconds
46 # as its filename.
47   set date [clock clicks -microseconds]
48
49   expect "$prompt"
50
51   send ":TRIG:SING\r"
52
53   expect "$prompt"
54
55 #ask the VNA to tell us when it's ready to save
56   send "*OPC?\r"
57
58   expect "+1"
59   expect "$prompt"
60
61 #send the save command
62   send ":MMEM:STOR:SNP \"D:\\${folder}\\${date}.S2P\"\r"
63
64   expect "$prompt"
65
66 #ask the VNA to update the screen
67   send ":DISP:UPD\r"
68 }
```

B.1.2 Python: view-data-rt-network.py

```
1
2  #!/usr/bin/python
3  #
4  # vna-view-data-rt-network.py
5  #
6  # This script plays back an animated realtime plot of the VNA
7  # information as S2P files are saved to its local memory.
8  # For this to work, you must have the folder the VNA is saving to
9  # mounted locally and specified in the dataFolder string
10
11 import numpy as np
12 import matplotlib.pyplot as plt
13 import pylab
14
15 import skrf as rf
16
17 #change this to the mount point on the local file system
18 # of the VNA save directory
19 dataFolder='../mountVNA'
20
21 # this technically reads all the files in a folder, so the
22 # longer it goes on, the slower it gets.
23 # works fine for a few thousand files though.
24 readstuff = rf.read_all(dataFolder,obj_type = 'Network')
25
26 networks = rf.NetworkSet(readstuff)
27
28
29 networks.animate('s_db',ylims=(-50,25),xlims=(300000,4500000000),\
30 show=True,savefigs=False,label=None)
```

B.2 Data analysis scripts

The following code was used during the study to analyze certain properties of the gathered S2P (touchstone) files from the VNA. Most of the files are in python using the scikit-rf library for extracting information from the touchstone files, with the exception of the time-delay information, which was produced by Dr. William C. Barott in MATLAB.

B.2.1 Python: analyze-wholefolder1plot.py

```
1
2  #!/usr/bin/python
3
4  #analyze_wholefolder1plot.py
5  #
6  # This file is a simple, few line script to see all of the S2P
7  # frequency information in a folder smashed together in 1 plot
8  #
9
10 import numpy as np
11 import matplotlib.pyplot as plt
12 import pylab
13
14 import skrf as rf
15
16
17 #change the path to whatever folder contains the data
18 dataFolder='../tests_2014_5_5/test1'
19
20 #This puts all of the S2P files in one object
21 readstuff = rf.read_all(dataFolder,obj_type = 'Network')
22
23 networks = rf.NetworkSet(readstuff)
24
25 #and this pline creates the plot.
26 networks.plot_s_mag()
27
28 # without the line below, the figure won't show
29 pylab.show()
```

B.2.2 Python: analyze-view1FileTimeDomain.py

```
1
2  #!/usr/bin/python
3
4  #analyze_view1FileTimeDomain.py
5  #
6  # This file is a short script that plots frequency and time
7  # information for a single S2P file.
8
9  import skrf as rf
10 import matplotlib.pyplot as plt
11 import pylab
12
13 #create a new fiture
14 figure1 = plt.figure()
15
16 #open a specified file and create a network object
17 # - Note - Change the path here to whatever file you'd like
18 #          to see time and frequency information of
19
20 network = rf.Network('../tests_2014_9_20/Test_1_Skidmark/1.S2P')
21
22
23 #This plots the S matrix in dB. m=1,n=1 corresponds to S21.
24 network.plot_s_db(m=1, n=0, show_legend=True)
25
26 #open another figure.
27 figure2 = plt.figure()
28
29 #This plots S21's time data.
30 network.plot_s_db_time(m=1, n=0, show_legend=True)
31
32
33 # without the line below, the figure won't show
34 pylab.show()
```

B.2.3 Python: analyze-savecsv.py

```
1
2  #!/usr/bin/python
3
4  #analyze_savecsv.py
5  #
6  # This file goes through a folder containing S2P files and
7  # exports them as CSV's for that pesky Dr. Barott.
8  #
9
10 import skrf as rf
11 import os
12
13 # This variable points to the path of the folder
14 # that we want to look at.
15 directory = '../tests_2014_9_20/test_2_classic/'
16
17 #create a list of the files in the directory
18 fileList = os.listdir(directory)
19
20 #store the number of files
21 numFiles = len(fileList)
22 count = 0
23
24 #Iterate through the files in the directory
25 for filename in sorted(fileList):
26
27         #only consider touchstone files
28         # (exclude desktop.ini and other stuff)
29         if filename.endswith('.S2P'):
30
31                 count = count + 1
32
33                 #this is so we can keep track of how far we are
34                 print 'processing ' + str(count) + ' out of ' + \
35                 str(numFiles) + ', ' + \
36                 str( round(float(count)/float(numFiles)\
37                  * 100,2) ) + '%'
38
39                 #create a scikit-rf network object
40                 aNetwork = rf.Network(directory + filename)
41
42                 #uncomment to write the touchstone again somewhere
43                 #aNetwork.write_touchstone(\
44                 #filename=filename,\
45                 #dir='csv-skd',\
46                 #write_z0=False,\
47                 #skrf_comment=False)
48
49                 #string with the file's name.
50                 filecsv = 'csv-csc/' + filename[:-3] + 'csv'
51
52                 #use skrf to write the file.
53                 aNetwork.write_spreadsheet(\
54                 file_name=filecsv,file_type='csv',\
55                 form='ri')
```

B.2.4 Python: analyze-findTDpeak.py

```
#!/usr/bin/python

#analyze_findTDpeak.py
#
# This file reads in a folder of S2P files, sorts them
# by filename (assumes the filename corresponds to a
# unix timestamp in us), and plots the maximum value
# of the time-domain information of S21 over
#  each file (frame).

import skrf as rf
import matplotlib.pyplot as plt
import matplotlib.gridspec as gridspec # subplots
import pylab
import numpy as np
import plotly
from matplotlib import cm, colors
import os
import plotly.plotly as py
import plotly.tools as tls
from plotly.graph_objs import *

# This is optional, but will export a plot my plotly account,
# which gives me greater flexibility in manipulating plots
py.sign_in("torresja4", "8i1gb0db6t")

# This variable points to the path of the folder we want to
# look at.

directory = '../tests_2014_9_20/Test_1_Skidmark'



#define a frequency range
startFrequency = 300e3
stopFrequency = 4.5e9
numpoints = 400

#calculate BW
bw = abs(stopFrequency - startFrequency)

#and time resolution
t_res = 1/bw



#create a list of the files in the directory
fileList = os.listdir(directory)

#store the number of files
numFiles = len(fileList)

#create some empty lists
peaks_dB = []
fastTime = []
```

```
slowTime = []

firstTime = 0


#Iterate through the files in the directory
for filename in sorted(fileList):

    #only consider touchstone files
    # (exclude desktop.ini and other stuff)
    if filename.endswith('.S2P'):

        #Since we're using the time difference from the
        # times stamped in the filename, the first file
        # in the folder corresponds to the start time.
        if firstTime == 0:
            firstTime = int(filename[:-4])

        # This corresponds to the difference between the
        # first file and the current.
        timeDiff = (int(filename[:-4]) - firstTime)

        print filename


        # Create a scikit-rf object using the current file
        # in the directory
        aNetwork = rf.Network(directory + filename)

        #copy its s-matrix in dB
        s_time_info_db = aNetwork.s_time_db

        #find the maximum value
        i,j,k = np.unravel_index(s_time_info_db.argmax(),\
        s_time_info_db.shape)

        #append the max to our list of maxes
        peaks_dB.append(s_time_info_db[i,j,k])

        #also append its time index to our list of fast times
        fastTime.append(i/2 * (t_res)/numpoints*100 * 1e9)

        #uncomment this line to see indices
        #instead of time values
        #fastTime.append(i)

        # also append the file's timestamp (in its filename) to
        # our list of slow times
        slowTime.append( timeDiff / 1e6 )



#figure 1 shows a 2x1  subplot, 1 with the index vs dB info of
# all files, and the other with a sample file's time-domain data
figure1 = plt.figure()
plt.subplot(2,1,1)
plt.plot(fastTime,peaks_dB)
```

```
113 plt.autoscale()
114 plt.xlabel('Time index (ns)')
115 plt.ylabel('peaks_dB, dB')
116 plt.title('peak value time-delay in gathered data')
117
118 plt.subplot(2,1,2)
119 aNetwork.plot_s_db_time(m=1,n=0)
120 plt.title('Sample file time domain information')
121
122 # Figure 2 shows the peak-data over time as gathered
123 # from the filename.
124 figure2 = plt.figure()
125 plt.plot(slowTime,peaks_dB)
126 plt.autoscale()
127 plt.xlabel('time in seconds')
128 plt.ylabel('peak value, dB')
129 plt.title('strength of peak value across gathered data \
130 (skidmark)')
131
132
133 #This is the code that actually uploads figures to plotly
134 #if you want this to happen, uncomment the lines.
135 #If they're uploaded, pylab doesn't plot them however.
136 #py.iplot_mpl(figure1)
137 #py.iplot_mpl(figure2)
138
139 pylab.show()
```

B.2.5 Python: analyze-findTDpeak-plusminus.py

```
#!/usr/bin/python

#analyze_findTDpeak_plusminus.py
#
# This file reads in a folder of S2P files, sorts them by
# filename (assumes the filename corresponds to a unix
# timestamp in us), and plots the maximum value AND a
# set offset index plus and minus from it of the
# time-domain information of S21over each file (frame).

import skrf as rf
import matplotlib.pyplot as plt
import pylab
import numpy as np
import os

# This variable points to the path of the folder
# we want to look at.
directory = '../tests_2014_9_20/Test_1_Skidmark'

#Defines the # offsets to look ahead of and before the maximum
#Each offset corresponds to 0.22 nS (our time resolution)
offset = 5

#define a frequency range
startFrequency = 300e3
stopFrequency = 4.5e9
numpoints = 400

#calculate BW
bw = abs(stopFrequency - startFrequency)

#and time resolution
t_res = 1/bw


#create a list of the files in the directory
fileList = os.listdir(directory)

#store the number of files
numFiles = len(fileList)

#create some empty lists
peaks_dB1 = []
fastTime1 = []


peaks_dBplus = []
fastTime2 = []


peaks_dBminus = []
fastTime3 = []

slowTime = []
```

```
56 firstTime = 0
57
58
59 #Iterate through the files in the directory
60 for filename in sorted(fileList):
61
62     #only consider touchstone files
63     #(exclude desktop.ini and other stuff)
64     if filename.endswith('.S2P'):
65
66         # Since we're using the time difference from the times
67         # stamped in the filename, the first file in the folder
68         # corresponds to the start time.
69         if firstTime == 0:
70             firstTime = int(filename[:-4])
71
72         #This corresponds to the difference between the
73         # first file and the current.
74         timeDiff = (int(filename[:-4]) - firstTime)
75
76         print filename
77
78         # Create a scikit-rf object using the current file in
79         # the directory
80         aNetwork = rf.Network(directory + filename)
81
82         #copy its s-matrix in dB
83         s_time_info_db = aNetwork.s_time_db
84
85         #find the maximum value
86         i,j,k = np.unravel_index(s_time_info_db.argmax(),\
87         s_time_info_db.shape)
88
89         #append the max to our list of maxes
90         peaks_dB1.append(s_time_info_db[i,j,k])
91
92         #also append its time index to our list of fast times
93         fastTime1.append(i/2 * (t_res)/numpoints*100 * 1e9)
94
95         #append max + offset to our list of max + offsets
96         peaks_dBplus.append(s_time_info_db[i+offset,j,k])
97         # and its corresponding index to index + offsets
98         fastTime2.append((i+offset)/2 * (t_res)/numpoints*100\
99          * 1e9)
100
101        #same as previous, but with a minus offset
102        peaks_dBminus.append(s_time_info_db[i-offset,j,k])
103        fastTime3.append((i-offset)/2 * (t_res)/numpoints*100 \
104        * 1e9)
105
106        # also append the file's timestamp (in its filename) to
107        # our list of slow times
108        slowTime.append( timeDiff / 1e6 )
109
110
111
112 #figure 1 shows a 2x2  subplot -
```

```
#   1 has the index vs dB info of all files,
#   2 has a sample file's time-domain data
#   3 is index vs dB of the offset+ data
#   4 is index vs dB of the offset- data
figure1 = plt.figure()
plt.title('classic burn data uncertainty')
plt.subplot(2,2,1)
plt.plot(fastTime1,peaks_dB1)
plt.autoscale()
plt.xlabel('Time index (ns)')
plt.ylabel('peaks_dB, dB')
plt.title('peak value time-delay in \
gathered data (classic)')

plt.subplot(2,2,2)
aNetwork.plot_s_db_time(m=1,n=0)
plt.title('Sample file time domain information (classic)')

plt.subplot(2,2,3)
plt.plot(fastTime2,peaks_dBplus)
plt.autoscale()
plt.xlabel('Time index (ns)')
plt.ylabel('peaks_dB, dB')
plt.title('+1.1nS offset of peak value time-delay in \
gathered data (classic)')

plt.subplot(2,2,4)
plt.plot(fastTime3,peaks_dBminus)
plt.autoscale()
plt.xlabel('Time index (ns)')
plt.ylabel('peaks_dB, dB')
plt.title('-1.1nS offset of peak value time-delay in \
gathered data (classic)')


#figure 2 also shows a 2x2  subplot -
#   1 has the peak value over slow time (as put in the filename)
#   2 has a sample file's time-domain info
#   3 is slowtime vs dB of the offset+ data
#   4 is slowtime vs dB of the offset- data
figure2 = plt.figure()
plt.title('classic burn data')
plt.subplot(2,2,1)
plt.plot(slowTime,peaks_dB1)
plt.autoscale()
plt.xlabel('time in seconds')
plt.ylabel('peak value, dB')
plt.title('strength of peak value across\
 gathered data (classic)')

plt.subplot(2,2,2)
aNetwork.plot_s_db_time(m=1,n=0)
plt.title('Sample file time domain information (classic)')

plt.subplot(2,2,3)
plt.plot(slowTime,peaks_dBplus)
plt.autoscale()
```

```
170 plt.xlabel('time in seconds')
171 plt.ylabel('peak value, dB')
172 plt.title('+1.1nS offset of peak value across \
173 gathered data (classic)')
174
175 plt.subplot(2,2,4)
176 plt.plot(slowTime,peaks_dBminus)
177 plt.autoscale()
178 plt.xlabel('time in seconds')
179 plt.ylabel('peak value, dB')
180 plt.title('-1.1nS offset of peak value across \
181 gathered data (classic)')
182
183
184 #Need this line for the plots to actually appear.
185 pylab.show()
```

B.2.6 Python: analyze-datain.py

```
1
2  #!/usr/bin/python
3
4  #analyze_datain.py
5  #
6  # This file iterates through our range of frequencies, and uses
7  # the given solutions to plot values of Ne vs Ve and w
8
9
10 import skrf as rf
11 import matplotlib.pyplot as plt
12 import pylab
13 import numpy as np
14 import math
15 import os
16
17
18 import plotly.plotly as py
19 import plotly.tools as tls
20 from plotly.graph_objs import *
21
22 # This is optional, but will export a plot my plotly account,
23 # which gives me greater flexibility in manipulating plots
24 py.sign_in("torresja4", "8i1gb0db6t")
25
26 #define a frequency range
27 startFrequency =  300000
28 stopFrequency = 4500000000
29 numpoints = 400
30
31 fspan = stopFrequency - startFrequency
32
33 # note to self, this is why we usually use points ending in xx1,
34 # i.e. 401 vs 400
35 fstep = fspan/(numpoints - 1)
36
37 #bandwidth
38 bw = abs(stopFrequency - startFrequency)
39
40 #time resolution
41 t_res = 1/bw
42
43
44 #Enter measured parameters here:
45
46 #Experimentally derived - delays for classic
47 delaymin_csc = 58.92e-12
48 delaymax_csc = 75.23e-12
49
50 delay_csc = delaymax_csc - delaymin_csc
51
52 #Experimentally derived - delays for skidmark
53 delaymin_skd = 55.10e-12
54 delaymax_skd = 63.34e-12
55
```

```
delay_skd = delaymax_skd - delaymin_skd

#Experimentally derived - signal levels at drop for classic
attenb4_csc = 5.3661
attenaft_csc = 4.9346

atten_csc = attenb4_csc - attenaft_csc

#Experimentally derived - signal levels at drop for skidmark
attenb4_skd = 5.3925
attenaft_skd = 5.165

atten_skd = attenb4_skd - attenaft_skd

#y represents the plume diameter
y = 0.10

#physical constants
e0 = 8.85418782e-12
qe = 1.60217657e-19
me = 9.10938291e-31
# speed of light in air has a refractive index
# of 1.0003 approximately
c = 299792458/1.0003

#generic frequency object to create networks if we need it later
frequency_v=rf.Frequency(startFrequency,\
                         stopFrequency,  \
                         numpoints,      \
                         'hz')


#initializing solution vectors
    # We analytically came up with four solutions for
    # each variable, and we need one for each burn


Nec = np.zeros((400,16),dtype=np.complex128)
Nes = np.zeros((400,16),dtype=np.complex128)
ves=[5e7,1e8,2.5e8,5e8,7.5e8,1e9,5e9,1e10]

m = 0
n = 0
freqsteps = frequency_v.f


#Iterate through the files in the directory
for freq in freqsteps:

    #These were the obtained solutions and they are not pretty.

    w = (freq + 8.5e9) * 2 * math.pi
    wf = w #oops

    m = 0

     for ve in ves:
```

```
113
114         #ugly equations corresponding to the solutions for
115         # finding Ne go here
116         Nec[n,m] = np.absolute((1j*(-e0 * me * ve**2 * w -  \
117                    20 * c * delay_csc * e0 * me * ve**2 * w \
118                    - 100 * c**2 * delay_csc**2 * e0 * me *  \
119                    ve**2 * w + e0**2 * me * ve**2 * w))     \
120                     /(qe**2 * (e0 * ve + 1j * w + 20 * 1j   \
121                    * c * delay_csc * w + 100 * 1j * c**2 *  \
122                     delay_csc**2 * w)))
123
124         Nec[n,m+8] = np.absolute((21.7391 * atten_csc * \
125                      (ve**2 + w**2))/ve)
126
127         Nes[n,m] = np.absolute((1j*(-e0 * me * ve**2 * w -  \
128                    20 * c * delay_skd * e0 * me * ve**2 * w \
129                    - 100 * c**2 * delay_skd**2 * e0 * me *  \
130                    ve**2 * w + e0**2 * me * ve**2 * w))     \
131                     /(qe**2 * (e0 * ve + 1j * w + 20 * 1j   \
132                    * c * delay_skd * w + 100 * 1j * c**2 *  \
133                     delay_skd**2 * w)))
134
135         Nes[n,m+8] = np.absolute(( 21.7391 * atten_skd * \
136                      (ve**2 + w**2))/ve )
137
138
139         m = m + 1
140
141
142     n = n + 1
143     print str(n) + " out of 400"
144     print str(wf) + " through " + str(stopFrequency)
145
146
147 #plot this funky business.
148
149 m = 0
150 classicNeSolutions = plt.figure()
151
152 #plot each line in a single figure
153 for ve in ves:
154     plt.plot(freqsteps,Nec[:,m],label= "Ve = " + str(ve))
155     plt.plot(freqsteps,Nec[:,m+8],label="Ve = " +str(ve),\
156     ls='dashed')
157     m = m + 1
158
159 plt.autoscale()
160 plt.xlabel('frequency, Hz')
161 plt.ylabel('value for Ne, number/cm^3')
162 plt.title('Ne solutions on iterated w using two models, classic')
163 #plt.legend()
164
165 m = 0
166 skidmarkNeSolutions = plt.figure()
167
168 for ve in ves:
169     plt.plot(freqsteps,Nes[:,m],label="Ve = " + str(ve))
```

```
170     plt.plot(freqsteps,Nes[:,m+8],label="Ve = " + str(ve),\
171     ls='dashed')
172 
173     m = m + 1
174 
175 plt.autoscale()
176 plt.xlabel('frequency')
177 plt.ylabel('value for Ne, number/cm^3')
178 plt.title('Ne solutions on iterated w using two models,\
179  skidmark')
180 
181 #This is the code that actually uploads figures to plotly
182 #if you want this to happen, uncomment the lines.
183 #If they're uploaded, pylab doesn't plot them however.
184 #py.iplot_mpl(classicNeSolutions)
185 py.iplot_mpl(skidmarkNeSolutions)
186 
187 #plots don't show up if you don't have this line,
188 #unless you're in interactive mode.
189 pylab.show()
```

B.2.7 MATLAB: jorge-reader.m

```
% Matlab code reader for the rocket CSV data from Jorge
% Created WCB 2014/10/23

function jorge_reader

% set the directory for the rocket data
directory = 'E:\users\jorge\Desktop\Google Drive\Thesis work\laptop_sep20\Thesis\code\commasv-csc'

% create a list of all of the file names
fns = dir(directory);

% Loop through each file
for n = 1:length(fns)
    % Call csvread with starting on row 1 and col 0 to kill the header data
    dd = csvread(strcat(char(directory),'\',char(fns(3).name)),1, 0);
    % Call the single reader and return the result in r. The single reader
    % will implement all math.
    if n == 1
        % On the first loop, don't force a "firstpeak". Let the reader
        % identify the first peak bin itself.
        r(n) = jorge_single_reader(dd);
    else
        % on subsequent loops, force the firstpeak to be the bin identified
        % on the first time through.
        r(n) = jorge_single_reader(dd, r(1).firstPeak);
    end
    disp(n)
end

disp('done')

figure
plot(20*log10([r.peakValue]))
xlabel('Frame number')
ylabel('power, dB-Arb')
title('Peak value extracted from the plume after correction')

figure
plot([r.peakDelay])
xlabel('Frame number')
ylabel('Delay, seconds')
title('Delay required for peak value')




function r = jorge_single_reader(dd, starter)

% Parse the complex value
```

```
50 flist = dd(:,1);
51 dreal = dd(:,6);
52 dimag = dd(:,7);
53
54 d = dreal + j*dimag;
55
56 % Create a list of frequencies, a bin separation time, and a
       list of time
57 % corresponding to the fft'd values.
58 flist(end) - flist(1);
59 tcoh = 1/(flist(end) - flist(1));
60 tlist = ((1:size(dd,1)) - (size(dd,1)/2))*tcoh;
61
62 % if the starter peak wasn't specified (1 argument), then find
       it. If it
63 % was specified, use it.
64 if nargin == 1
65     tseries = fft(d);
66     [a,b] = max(abs(tseries)); % B is the index
67 else
68     b = starter;
69 end
70
71 % Create a list of delays to try. Go +/- 1 sample.
72 dlist = linspace(-tcoh, tcoh, 10000);
73 for n = 1:length(dlist)
74     cdelay = dlist(n); % Pull the current one
75     % Use the current one to make an exponential response, but I
       screwed up
76     % and pulled it again (no worries, just didn't use "cdelay"
      it's late
77     dspec = exp(-j*2*pi*flist*dlist(n));
78     % store the results in a matrix
79     fsmat(:,n) = d.*dspec;
80 end
81 % create an FFT of the prev matrix to get slow time vs fast time
82 tsmat = fft(fsmat);
83 % convert to magnitude but also extract the row corresponding to
       the "peak"
84 % value, so that we're only looking at that row
85 pkvdel = abs(tsmat(b,:));
86 % find the delay and peak value corresponding to the delay that
       causes the
87 % peak row (eg starter) to exhibit a maxima over all time dleays
       that we
88 % tried
89 [a2,b2] = max(pkvdel);
90
91 % store and report
92 r.peakValue = a2;
93 r.peakDelay = dlist(b2);
94 r.firstPeak = b;
```

References

[1] S. Nayak and J. Meledath, "Lightning-induced current and voltage on a rocket in the presence of its trailing exhaust plume," *IEEE Transactions on Electromagnetic Compatibility*, vol. 52, no. 1, pp. 117–127, Feb 2010.

[2] Goddard Space Flight Center, "NASA Case Study: Atlas Centaur-67: Go or No Go for Launch?" National Aeronautics and Space Administration, GSFC, Tech. Rep. GSFC-1008C-1, 2011.

[3] C. Kraft, Jr., "Apollo Expeditions to the Moon, Chapter 7.3: A lightning strike," National Aeronautics and Space Administration, Scientific and Technical Information Office, Tech. Rep. SP-350, 1975.

[4] J. A. Blevins, R. A. Frederick Jr., and H. W. Coleman, *"An Experimental Investigation of Microwave Diagnostics in a Labscale Rocket Exhaust Plume.* 30th AIAA/ASME/SAE/ASEE Joint Propulsion Conference, Indianapolis, IN, 1994.

[5] N. Coutu, "Implementation of microwave transmissions for rocket exhaust plume diagnostics," Master's thesis, Embry-Riddle Aeronautical University, 2012. [Online]. Available: http://books.google.com/books?id=ks-2mAEACAAJ

[6] W. Balwanz, "The plasmas of rocket flight," in *IRE International Convention Record*, vol. 9, March 1961, pp. 3–9.

[7] G. P. Sutton and O. Biblarz, *Rocket propulsion elements.* John Wiley & Sons, 2010.

[8] R. H. Lee, I. Chang, and G. E. Stewart, "Studies of plasma properties in rocket plumes," DTIC Document, Tech. Rep., 1982.

[9] B. van der Veek, S. Chintalapati, D. R. Kirk, and H. Gutierrez, "Modeling and validation of ku-band signal attenuation through rocket plumes," *Journal of Spacecraft and Rockets*, vol. 50, no. 5, pp. 992–1001, 2013.

[10] E. Baghdady and O. Ely, "Effects of exhaust plasmas upon signal transmission to and from rocket-powered vehicles," *Proceedings of the IEEE*, vol. 54, no. 9, pp. 1134–1146, Sept 1966.

[11] K. Kinefuchi, I. Funaki, H. Ogawa, T. Kato, S. Tachikawa, T. Shimada, and T. Abe, "Investigation of microwave attenuation by solid rocket exhausts," in *47th AIAA Aerospace Sciences Meeting Including The New Horizons Forum and Aerospace Exposition, AIAA*, vol. 1386, 2009, pp. 5–8.

[12] H. A. Poehler, "Project see-thru flame interference measurements, titan iii-c launch test 8275/2250," DTIC Document, Tech. Rep., 1968.

[13] K. Baldwin, J. Eckerman, R. Williamson, and R. Buck, "Plasma properties in the plume of solid propellant motors containing CsNO3 and KNO3," DTIC Document, Tech. Rep., 1963.

[14] T. J. Seliga and L. Smoot, "Rocket exhaust plume radar attenuation and amplitude/phase noise," *Journal of Spacecraft and Rockets*, vol. 4, no. 6, p. 9, 1967.

[15] K. Kinefuchi, K. Okita, I. Funaki, and T. Abe, "Prediction of in-flight radio frequency attenuation by a rocket plume," *Journal of Spacecraft and Rockets*, pp. 302–309, 2014.

[16] R. Fitzpatrick. (2006) Classical electromagnetism. [Online]. Available: http://farside.ph.utexas.edu/teaching/em/lectures/lectures.html

[17] D. L. Underwood and L. Smoot, "Prediction of microwave attenuation characteristics of rocket exhausts," *Journal of Spacecraft and Rockets*, vol. 3, no. 3, pp. 302–309, 1966.

[18] D. M. Pozar, *Microwave Engineering, Third Edition.* John Wiley & Sons, 2005.

[19] G. Goebel. (2013) Introduction to radar technology. [Online]. Available: http://www.vectorsite.net/ttradar.html

[20] J. H. McClellan, R. W. Schafer, and M. A. Yoder, *Signal Processing First.* John Wiley & Sons, 2005.

[21] Y. Zhu, "Study of microstrip antennas on double negative metamaterials," Master's thesis, Hong Kong Polytechnic University, 2010.

[22] L. Sevgi, *Complex electromagnetic problems and numerical simulation approaches.* John Wiley & Sons, 2003.

[23] Y. Yang, Y. Wang, and A. E. Fathy, "Design of compact vivaldi antenna arrays for uwb see through wall applications," *Progress In Electromagnetics Research*, vol. 82, pp. 401–418, 2008.

[24] M. Wang, W. Wu, and Z. S. Shen, "Bandwidth enhancement of antenna arrays utilizing mutual coupling between antenna elements," *International Journal of Antennas and Propagation*, vol. 2010, no. 690713, pp. 774–780, 2009.

[25] S. J. Orfanidis, "Antenna arrays," in *Electromagnetic Waves and Antennas*. Distributed on-line only, 2014, ch. 19, pp. 864–894. [Online]. Available: http://www.ece.rutgers.edu/~orfanidi/ewa/

[26] A. Abbosh, "Gain and bandwidth optimization of compact uwb tapered slot antennas," *International Journal of Microwave And Optical Technology*, vol. 2, no. 3, pp. 222–225, 2007.

[27] Microwaves101. (2008) Designing wilkinsons in excel. [Online]. Available: http://www.microwaves101.com/microwave-encyclopedia/623-designing-wilkinsons-in-excel

[28] *Tripoli Rocketry Association Safe Launch Practices*, Tripoli Rocketry Association.

[29] Cesaroni Technology Incorporated. (2012) Pro54 high power rocket motor reload kits. [Online]. Available: http://www.pro38.com/products/pro54/motor.php

[30] G. Herrmann and L. Kelley, "Enhanced resolution in simple radars," *Aerospace and Electronic Systems, IEEE Transactions on*, vol. 25, no. 1, pp. 64–72, Jan 1989.